Crystallographic Dependence of Spin Orbit Torques in Epitaxial Thin Films

Dissertation

zur Erlangung des
Doktorgrades
der Naturwissenschaften
(Dr. rer. nat.)

der Naturwissenschaftlichen Fakultät II
Chemie, Physik und Mathematik

Martin-Luther-Universität Halle-Wittenberg

vorgelegt von

Herrn Bharat Grover

Gutachter:
Prof. Dr. Stuart S. P. Parkin
Prof. Dr. Ingrid Mertig
Dr. Chandra Shekhar

Tag der öffentlichen Verteidigung:
22.10.2024

Dedicated to my Parents and Sister . . . .

Late Kishan Chand Grover, Neelam Grover and
Dr. Nitika Grover

Acknowledgments

“I would like to express my heartfelt gratitude to my mother and sister for their unwavering love and support throughout my academic journey. Their constant encouragement, guidance, and sacrifices have been the foundation of my success, and I am indebted to them for their unwavering support. Without their unwavering belief in me and their willingness to help in any way possible, I would not have been able to achieve this significant milestone.

I would like to express my sincere thanks to my advisor, Prof. Dr. Stuart S. P. Parkin, for his invaluable guidance and support throughout my research. His expertise, feedback, and constructive criticism have been instrumental in shaping my research/study approach and methodology, and have pushed me to reach my full potential. I am grateful for his unwavering support and encouragement, even during the most challenging times. It has been an honor and a privilege to work with such a dedicated and brilliant supervisor.

I am particularly grateful to Dr. Binoy Krishna Hazra, who provided technical assistance in providing new samples and the constant support for data analysis phase of my research. I would also like to thank you Prof. Amir Capua (Hebrew University of Jerusalem), Dr. Tianping Ma, and Prof. Georg Woltersdorf (University of Halle) for providing technical assistance in building OFMR setup. I would like to express my sincere appreciation to Dr. Banabir Pal, Dr. Abhay Kant Srivastava and Pranava Keerthi Sivakumar for having fruitful scientific discussions.

I am particularly thankful to Michael Strauch who provided an invaluable administrative support during my stay at MPI and Without his help, I would not have been able to focus on my research/studies as much as I did.

I am grateful to the Max Planck Institute of Microstructure Physics and Martin-Luther-University Halle-Wittenberg for providing the resources and facilities necessary for my research.

Lastly, I would like to express my sincere appreciation to all my colleagues at Max Planck Institute of Microstructure Physics, who have contributed to this research in various ways. Their support, guidance, and encouragement have been invaluable throughout my PhD journey.”

Abstract

Spintronics is one of the emerging fields in nanoelectronics, where the spin angular momentum of electrons is utilized to store and manipulate information. The spin current generated by the spin Hall effect (SHE) in heavy metals (HM) can be used to change the spin state in adjacent ferromagnet layers (FM) via spin-orbit torques (SOTs). In this thesis, I focus on characterizing such spin orbit torques in different materials. Specifically, the crystallographic dependence of spin orbit torques has been studied in two different classes of materials: heavy metal (Pt) and cubic non-collinear antiferromagnet (Mn_3Pt).

In Pt, spin orbit torques were studied in three crystallographic directions: Pt(111), Pt(110), and Pt(001) respectively. We utilized optical and electrical techniques, namely optical detected ferromagnetic resonance (OFMR) and spin orbit driven ferromagnetic resonance (ST-FMR). The results obtained from these techniques were compared using DC bias methods, and the advantages of using optical techniques have been discussed.

For SOT characterization in Mn_3Pt, we studied the role of exchange bias along two crystallographic directions: $Mn_3Pt(111)$ and $Mn_3Pt(001)$ respectively. To understand the role of exchange bias, a thin layer of Cu was inserted between Permalloy (Py) and Mn_3Pt layers. We observed damping/antidamping-like (τ_{AD}) and field-like torques (τ_{FL}) due to spin polarization in three directions (σ_x, σ_y, and σ_z respectively). The origin of these spin polarizations could be related to the magnetic and crystal symmetry of the crystal. Finally, we were able to demonstrate the field-dependent switching of FM with perpendicular anisotropy via the spin orbit torque generated by the Mn_3Pt layer.

Contents

List of Figures

List of Tables

1

Introduction

The goal of spintronics research is to reduce the power consumption of CMOS based devices and at the same time to increase the storage and processing capabilities [18]. Spin currents can be categorized into two types: **spin-polarized current** and **pure spin current**. The former is the flow of spins with net charge current associated with it, and the latter one is just the flow of pure spin current with no net charge current associated with it. The efficiency of pure spin current generation and manipulation are the critical figures of merit for industrial device applications. One of the promising applications of SHE can be implemented in the Racetrack Memory (RM), which was proposed by Prof. Stuart Parkin in early 2008. RM consists of a nanowire made of ferromagnetic material, where information is stored in magnetic domain walls. These domain walls are typically magnetized in a perpendicular direction (shown in Fig. 1.1) [1]. The domain walls are the transition region between two domains magnetized in opposite directions, and the spacing between two successive domains are defined the bit length of the memory. The data bits are moved along the RM by means of passing the spin polarized current. The reading is done by intersecting the RM with magnetic tunnel junctions magneto resistive devices [1]. Racetrack memory (RM) has generated significant interest due to its outstanding potential for low-power, high-density and high-speed data storage. However, for long time current driven domain wall rely only on the flow of spin polarized current by means of spin transfer torque (STT), in which domain wall move along the direction of applied current. Recently, spin orbit torque (SOT) driven based RM has been demonstrated, in which a strip of heavy metal such as Pt and W are used to inject the pure spin current into the ferromagnetic layer [19] [20]. SOT based RM are more efficient compares to conventional STT, which provides lower shift current density and perform higher DW velocity. Additionally, since the resistance of heavy metal is usually lower than the FM layer and therefore, low voltage and power consumption is needed to achieve the same DW velocity.

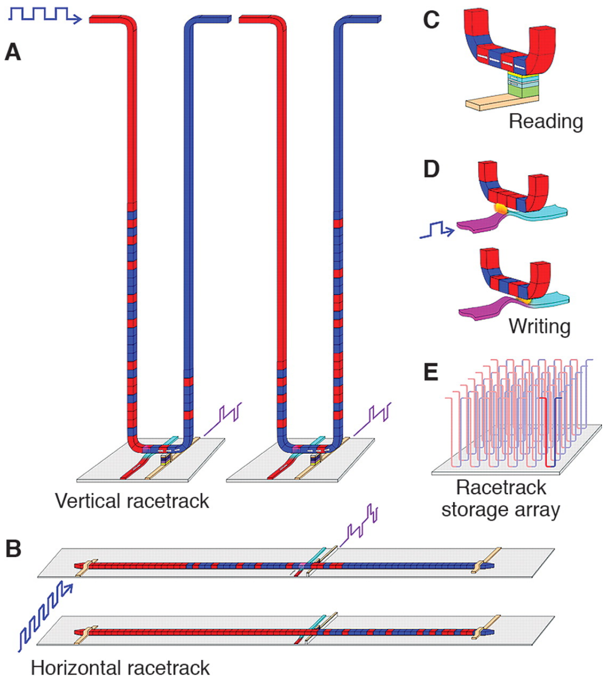

Figure 1.1: Schematic of Racetrack memory. The Fig. is adapted from [1].

The efficiency of generated pure spin current in a given material is defined by the generated spin current (j_s) per unit energy applied, or otherwise known by the parameter spin Hall angle ($\theta_{SH} = j_s/j_c$), where j_c is applied electric current. Despite having significant application of pure spin current, the accurate estimation of j_s or θ_{SH} is quite challenging and crucial, as the generated spin current (j_s) doesn't have direct electrical voltage associated with it [18]. Various techniques are employed to measure the θ_{SH} are both electrical and optical in nature. However, these techniques often yield different values for θ_{SH} [4]. This discrepancy arises due to the model dependence of some techniques, leading to potential over- or underestimation of θ_{SH} [21]. Therefore, it is of utmost importance to develop optical techniques that can be utilized in conjunction with existing electrical techniques to enable a direct comparison of spin Hall measurements. One widely employed technique for studying the spin Hall effect (SHE) in FM/HM bilayers is Spin Torque Ferromagnetic Resonance (ST-FMR) [22].

Another aspect of studying the spin Hall effect (SHE) is the influence of crystal and magnetic symmetry on its efficiency. The origin of SHE is dependent on the electronic and magnetic structure of materials, considering both intrinsic and extrinsic contributions [4]. Recent research has revealed that non-collinear antiferromagnetic materials, where magnetic moments are tilted in space, exhibit spin chirality. This spin chirality is characterized by the expression $S_{i,j,k} = S_i.(S_j \times S_k)$, where $S_{i,j,k}$ represent non-coplanar spins in a lattice. The spin chirality gives rise to a fictitious magnetic field known as a Berry phase, which plays a pivotal role in the SHE and anomalous Hall effect (AHE) observed in non-collinear antiferromagnetic materials like Mn_3X (where X can be Sn, Ge, Pt, Ir, etc.), even in the absence of significant spin-orbit coupling (SOC) [6]. Consequently, non-collinear antiferromagnetic materials possess intriguing magnetic and crystal symmetries, making them compelling candidates for studying the SHE.

With these goals and requirements in mind, this thesis focuses on several key aspects. Firstly, we investigate the crystallographic dependence of the spin Hall effect (SHE) in Pt along three crystallographic directions: (001), (110), and (111). In this research, we utilize an in-house developed optical technique called optically detected ferromagnetic resonance (OFMR) and compare the results obtained with this optical technique to those obtained using a standard spin-torque ferromagnetic resonance (STFMR) technique.

The latter part of the thesis delves into the crystallographic dependence of spin orbit torque in cubic $Mn_3Pt(001)$ and $Mn_3Pt(111)$. By exploring the angular dependence of STFMR measurements, we aim to gain insights into the origin of different torques present in these films. Subsequently, we observe field-dependent magnetization switching using the Mn_3Pt film as a spin Hall material. Through these investigations, we aim to advance our understanding of the crystallographic dependence of the spin Hall effect and spin orbit torque, utilizing optical and electrical techniques

1.1 Outline of the thesis

In Chapter **2** we described the scientific background needed to understand the rest of the thesis. In the beginning, we explained the basics of spintronics, spin current, spin orbit coupling, and then we articulated the spin Hall effect (SHE) and its different mechanism (intrinsic and extrinsic). After this, we described the non-collinear antiferromagnets in the context of spin Hall effect (SHE) and how these materials can be useful for spintronics application. In particular, we focus on the spin orbit torque generated from cubic $Mn_3Pt(111)$ and $Mn_3Pt(001)$, respectively.

In Chapter **3** experimental methods and techniques used in the context of this work has been discussed. At first, the basic principle of the sample preparation and characterization technique such magnetron sputtering, X-ray diffraction (XRD), Atomic Force Microscopy (AFM), Physical Property Measurement System (PPMS) has been discussed. Then, the basic of the device fabrication such as optical lithography and resistivity measurements are discussed. The last two sections of this chapter are devoted to the techniques, namely : Optically Detected Ferromagnetic Resonance (OFMR) and Spin Torque Ferromagnetic Resonance (STFMR).

Chapter **4** serves as the inaugural experimental chapter in the thesis. In this chapter, we first discuss the sample preparation and its structural, magnetic properties such as XRD, AFM, MOKE etc. Then, we describe the OFMR set up in detail and discuss the way of measuring the FMR response in the setup such as field sweep and delay sweep measurement, respectively. After this, the principle of STFMR measurement is presented. In the end, the comparison of above-mentioned techniques are discussed with respect to samples Pt(111), Pt(110) and Pt(001), respectively and discuss the advantage of optical technique compare to STFMR especially in the context of DC bias measurement.

Chapter **5** comprises the subsequent experimental chapter within the thesis. Firstly, sample preparation and its basics structural and magnetic characterization are presented. Then, unconventional spin orbit torques in non collinear antiferromagnets Mn_3Pt with respect to its crystallographic directions (111) and (001) are discussed. In particular, angular dependence STFMR measurements are performed to estimate torques associated with these materials. In the last section, field dependent magnetization switching of perpendicular anisotropic ferromagnetic material with Mn_3Pt as a spin Hall material are discussed.

Finally, Chapter **6** presents the summary and outlook of the thesis.

2

Therotical Background

In this chapter, the theoretical background is presented to provide the necessary context for understanding the subsequent chapters of the thesis. The first section provides an overview of spintronics, introducing the fundamental concepts and principles in the field. The subsequent sections delve into the concept of spin current, exploring its properties and characteristics. The focus then shifts to the Spin Hall Effect (SHE) and its various mechanisms. The different mechanisms underlying SHE are discussed in detail, shedding light on the intricate interplay between spin and charge currents.

The latter part of the chapter concentrates on antiferromagnetic spintronics. It explores the Anomalous Hall Effect (AHE) and Spin Hall Effect (SHE) in non-collinear antiferromagnets, emphasizing their unique properties and potential applications. Additionally, the concept of Berry curvature, a key factor in understanding the phenomena observed in non-collinear antiferromagnets, is introduced and explained.

2.1 Spintronics

Conventional electronics relies solely on the charge degree of electrons, completely ignoring the fact that electrons also possess a unique quantum mechanical property known as “intrinsic angular momentum” or “spin”. The spin of an electron is a direct consequence of relativistic quantum mechanics and has no classical analogue. Since the invention of the first semiconductor transistor at ATT’s Bell Labs in 1947 [23], the number of transistors on an integrated chip has doubled every two years (known as Moore’s Law) [24]. This rapid development, with an increasing number of transistors, has resulted in smaller and smaller modern computers. However, this downsizing also brings the challenge of joule heating in microelectronics. Surprisingly, all these devices utilize the charge degree of freedom to store and process information. Hence, there is a growing need for devices that can store more information, consume less power, and operate faster.

Spintronics is an emerging field in the next-generation nanoelectronic devices aimed at reducing power consumption and increasing memory and processing capabilities [25]. As the name suggests, Spintronics utilizes the spin degree of freedom of electrons to store and manipulate information. The field of Spintronics began with the discovery of Giant Magnetoresistance (GMR) in alternating metallic ferromagnetic thin films separated by nonmagnetic layers in 1988. [26][27][28].

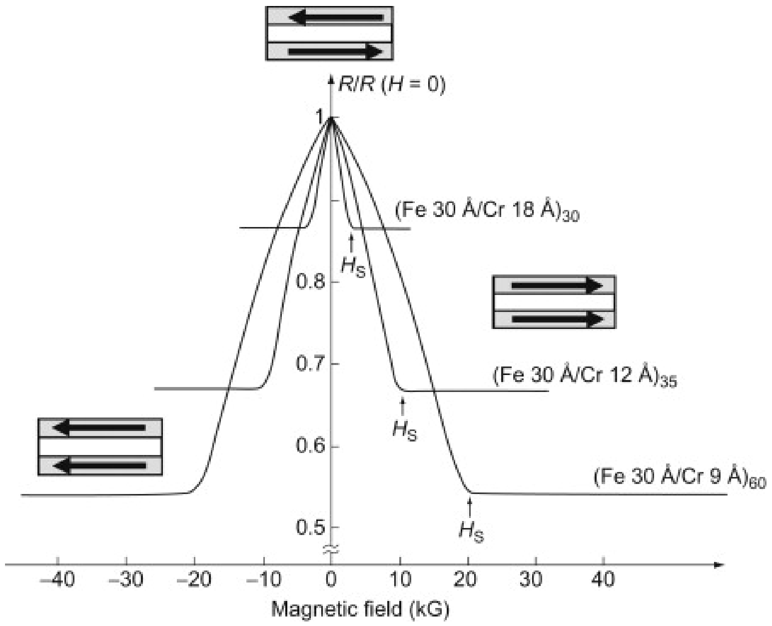

Figure 2.1: Resistivity change due to applied magnetic field in Fe/Cr multilayers [2].

In a typical Giant Magnetoresistance (GMR) structure, the electrical resistance of the system changes depending on the relative orientation of the magnetization in the two ferromagnetic layers. When the magnetization is antiparallel (AP), the resistance is higher, whereas when they are parallel (P), the resistance is lower (as illustrated in Figure 2.1). This GMR phenomenon arises from the spin-dependent scattering of electrons in ferromagnetic materials. Due to the difference in density between up and down spins at the Fermi level in a ferromagnetic material, the scattering rates for these spin orientations are also different [2].

A similar effect is observed when an insulating layer replaces the conducting barrier between the two ferromagnetic layers. In this case, electrons tunnel through the insulating layer, leading to a phenomenon known as tunneling magnetoresistance (TMR) [29]. This TMR effect finds practical application in Magnetic Tunnel Junctions (MTJs). MTJs serve as the fundamental building blocks of Magnetic Random Access Memory (MRAM), as shown in Figure 2.2. MRAM is a non-conventional memory technology that offers potential advantages over conventional CMOS-based computer memory, such as non-volatility, low energy dissipation, fast switching speed, radiation hardness, and durability [3].

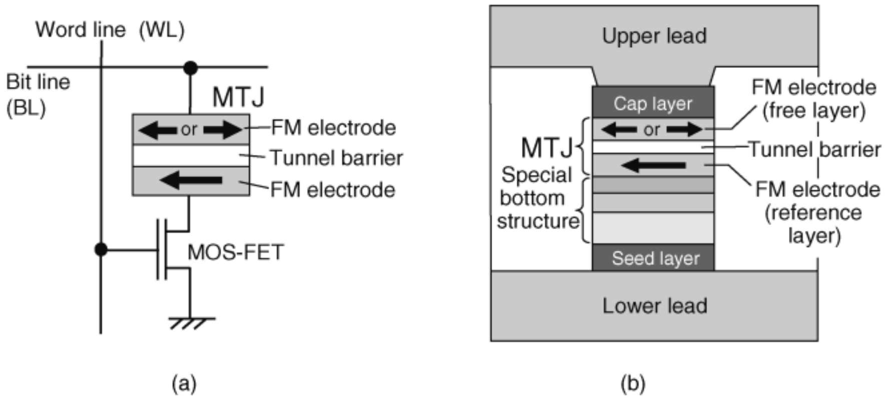

Figure 2.2: (a) Typical circuit diagram of magnetic random-access memory (MRAM) and (b) cross-section area of typical MTJ as a spin valve [3].

There are three important pillars in the studies of Spintronics

- **Spin Injection**, as this is the first step to generate efficiently and to implement them in spintronics device application.
- **Spin Manipulation**, to control the orientation of the electron's spin to process or store the information.
- **Spin Detection**, to read out the spin coherent states after applying the logic operations on them.

2.2 Spin Current

An electron carries an elementary charge of –e, and when there is a coherent flow of electronic charges, it gives rise to an electric current. In conventional electric currents, the spin orientations of electrons are random, meaning that the spins do not have any significant effect on the information being carried. However, in spin currents, the flow is specifically of spin angular momentum without any accompanying charge current. Spin currents are distinct from conventional currents in that they carry and manipulate the spin information of electrons.In order to formulate the spin current, let us consider the Hamiltonian of many body systems [30].

$$H = \sum_{i,\sigma} \frac{1}{2m}(P_i - \frac{e}{c}A_\sigma)^2 + \sum_{i \neq j} V_{ij} \tag{2.1}$$

The first term defines the kinetic energy of the system, and the second term represents the non-neighbouring interactions between electrons. Where $\sigma = \uparrow\downarrow$ is the spin index. From the Hamiltonian, the velocity operators of electrons are

$$v_\sigma = -\frac{c}{e}\frac{\partial H}{\partial A_\sigma} = \sum_i \left(P_i - \frac{e}{c}A_\sigma\right)/m \tag{2.2}$$

Here A_σ is the spin dependent vector potential. The electric current can be expressed as

$$j_e = -e\left(\frac{\partial E}{\partial A_\uparrow} + \frac{\partial E}{\partial A_\downarrow}\right) = -e(v_\uparrow + v_\downarrow)/2 \tag{2.3}$$

Where E $(A_{\uparrow,\downarrow})$ is the energy eigenvalue for the system. If the vector potential is independent of spins i.e., $A_\uparrow = A_\downarrow$ then $v_\uparrow = v_\downarrow$, velocities of electrons are independent of the spin orientations. However, if the vector potential is spin dependent i.e., $A_\uparrow \neq A_\downarrow$ then the velocities will also dependent on the spins for e.g., $v_\uparrow \neq -v_\downarrow$. In this case $j_e = 0$ but there will be non-zero spin current $j_s \neq 0$. Therefore, spin current can be defined as $\frac{\hbar}{2}(v_\uparrow - v_\downarrow)$, where factor $\frac{\hbar}{2}$ comes from the quantum mechanical unit of spin. It should be pointed that there is clear distinction between **spin polarized current** and **pure spin current**, the former includes charge current with majority spin up or spin down electrons and while the latter is just a flow of pure spins with no charge current associated with it.

2.3 Spin Orbit Coupling

Spin-orbit coupling (SOC) is a relativistic phenomenon that occurs when the spin (or magnetic moment) of a moving electron couples to an effective magnetic field in the presence of an electric field. SOC is a direct consequence of the Dirac equation and is included as a correction term in the equation, given by:

$$H_{SO} = \eta_{SO}\sigma.(\mathbf{k} \times \nabla V(r)) \tag{2.4}$$

Here, $\eta_{SO} = \frac{\hbar}{2mc^2} \approx 3.7 \times 10^{-62}$ represents the SOC strength, $\hbar k = \mathbf{p}$, V(r) is the potential acting on the electron, and σ represents the Pauli matrices. In a solid, the potential acting on the electron can be divided into two components: a periodic potential originating from the lattice, denoted as $V_L(r)$, and a non-periodic potential due to impurities. The interaction between the spins (σ) and the periodic potential V_L leads to an effective term of the form:

$$H_{SO,int} = -\frac{1}{2}\sigma.\mathbf{B(k)} \tag{2.5}$$

Here, **B(k)** is the **k**-dependent magnetic field, which depends on the electron's band structure. In this context, **k** is considered as a crystal wave vector. This contribution is solely determined by the electron's band structure and arises even in the absence of impurities, making it an intrinsic contribution of SOC. Additionally, due to the non-periodic part of the potential, SOC takes a similar form:

$$H_{SO,ext} = \eta'_{SO}\sigma.(\mathbf{k} \times \nabla V(r)) \tag{2.6}$$

Here, η'_{SO} represents the strength of extrinsic SOC, which can be orders of magnitude larger than η_{SO}. This extrinsic SOC is associated with the non-periodic part of the potential and is considered as an extrinsic contribution. As a result of the intrinsic and extrinsic contributions of SOC, the velocity and coordinate operators of the electron become spin-dependent. When an electron scatters from an impurity, the scattering cross-section becomes spin-state-dependent, leading to unequal scattering angles for spin-up and spin-down electrons. This phenomenon gives rise to the mechanism of the spin Hall effect (SHE), which can be explained by various mechanisms such as Mott scattering and the side jump mechanism [4].

2.3.1 Rashba and Dresselhaus type of SOC

As mentioned in the previous section, the spin-orbit coupling (SOC) takes the form of $H_{SO} \propto -\sigma.(\nabla V(r) \times \mathbf{p})$. Let's denote the term $w(\mathbf{p}) = \nabla V(r) \times \mathbf{p}$ as the SOC field. Since the SOC is preserved under time reversal, the term $w(\mathbf{p})$ must be odd with respect to the electron's momentum **p**. This odd term survives only in systems where there is a lack of inversion symmetry. Dresselhaus first noticed that certain semiconductors, such as GaAs and InSb, lack inversion symmetry, resulting in an odd w(**p**) [31]. Bychkov and Rashba proposed that in certain quantum wells, the structural inversion symmetry is broken along the growth direction, creating an interfacial electric field $E = E_z\hat{z}$. This broken inversion symmetry gives rise to SOC of the form $H_{R,SO} = \frac{\alpha_R}{\hbar}(\mathbf{z} \times \mathbf{p}).\sigma$, where α_R is known as the Rashba parameter. The Hamiltonian for a two-dimensional electron gas (2DEG) with these two SOC terms takes the form [32]:

$$H_{SO} = \frac{\alpha_R}{\hbar}(\sigma_x p_y - \sigma_y p_x) + \frac{\lambda}{\hbar}(\sigma_x p_x - \sigma_y p_y) \tag{2.7}$$

The first term represents the Bychkov-Rashba SOC arising from the lack of inversion symmetry at the interface, while the second term represents the Dresselhaus SOC resulting from the lack of inversion symmetry in bulk semiconductors. Both Dresselhaus and Rashba SOC couple the spin of the electron to its momentum direction and cause a splitting of the spin sub-bands in energy. The mechanism of the intrinsic spin Hall effect can be explained by these types of SOC, namely Dresselhaus and Rashba SOC [4].

2.4 Spin Hall Effect (SHE)

The electrical manipulation and generation of spin currents are of key importance in the field of spintronics. Among several possibilities, the Spin Hall Effect (SHE) stands out as one of the primary methods for generating spin currents. In this section, we will discuss SHE and delve into its underlying mechanism [4].

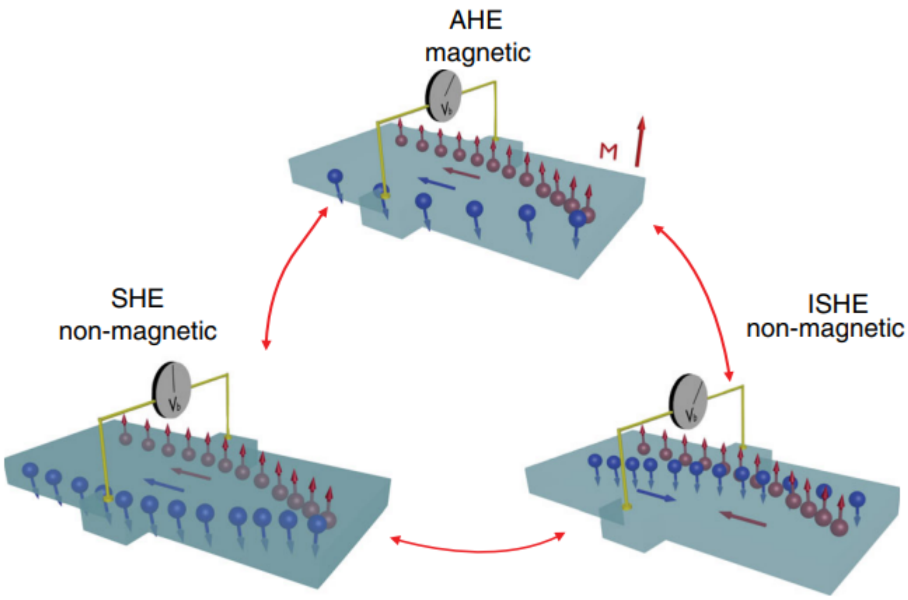

Figure 2.3: An illustration of the connected family of the spin-dependent Hall effects. In the AHE, a charge current generates a polarized transverse charge current. In the SHE, an unpolarized charge current generates a transverse pure spin current. In the ISHE, a pure spin current generates a transverse charge current. The figure is taken from ref.[4].

SHE is a collection of relativistic spin-orbit coupling phenomena, where longitudinal charge current generates transverse spin current and vice versa. The theoretical prediction of SHE was made in 1971 by Dynkonov and Perel, based on the idea of asymmetric Mott scattering [33]. In typical SHE, a longitudinal electrical current passing through a material generates pure transverse spin current polarized perpendicular to the plane defined by the spin and charge current (Red and blue arrows define the direction of spins in Fig. 2.3). In the reciprocal of SHE, known as the Inverse Spin Hall Effect (ISHE), a pure spin current generates a transverse charge current. In order to have SHE/ISHE, the material should possess large SOC. SHE shares some common mechanism with anomalous Hall effect (AHE), where spin orbit coupling generates an asymmetric deflection of the electron charges depending on their spin direction [34] as shown in Fig. 2.3. The AHE can be measured electrically in a ferromagnet via a transverse voltage due to the difference in population of majority and minority charge carriers. Since there is no charge current or electrical signal associated with pure spin current, therefore, it is difficult to detect the SHE electrically.

The important difference between AHE and SHE/ISHE is that, AHE correlates the charge degrees of freedom via SOC which is a conserved quantity. However, SHE/ISHE correlates to the spin degree of freedom, which is a non conserved quantity subject to decay and dephasing. The first observation of SHE was observed by Kato et al. and subsequently by Wunderlich et al. by optical means [35] [36]. In their experiments, scanning Kerr microscopy was used to measure the electrical induced out of plane spin accumulation near the edges of unstrained GaAs and InGaAs films [35] [36].

2.5 Mechanism of SHE

The microscopic mechanism of SHE is similar to AHE. There are three distinct microscopic mechanism namely : **the intrinsic**, **the skew** and unique **the side jump mechanism**. Similar to AHE, the contributions from these mechanisms can be classified based on the transport lifetime (τ). These contributions can be observed by experiments. Within the metallic regime, it is easy to identify the contributions to the spin Hall conductivity, σ_{xy}^{H} which is varied as τ^1 and as τ^0.

Similar to AHE experiment, $\sigma_{xy}^{H} \propto \sigma_{xx}$ (longitudinal conductivity) $\propto \tau^1$ and the τ can be varied by altering disorder or changing the temperature. This contribution proportional to τ^1 is called skew scattering contribution, σ_{xy}^{H-skew}. The other contributions which are not dependent on τ (τ^0 or independent of σ_{xx}) can be further divided into two terms : intrinsic and side jump. The total contributions of σ_{xy}^{H} can be written as:

$$\sigma_{xy}^{H} = \sigma_{xy}^{H-skew} + \sigma_{xy}^{H-int} + \sigma_{xy}^{H-sj} \tag{2.8}$$

2.5.1 Intrinsic Mechanism

Ordinary Hall effect was discovered by Edwin Hall in 1880 and the microscopic understanding of this effect was unknown for the next few decades. As the name implies, the intrinsic contribution of SHE depends on the band structure of the crystal structure [4]. Within semiclassical theories it has been shown that due to interband coherence there is an additional anomalous velocity arises from momentum-berry phase [37][38].

$$v_k = \frac{\partial E_k}{\partial k} + e\mathbf{E} \times \Omega_k \tag{2.9}$$

The first term in the above equation is the normal velocity of the electron due to band energy with respect to electron's momentum **k** and the second term is called the anomalous velocity, which is linear with respect to **E** and Ω is called Berry curvature [39]. To understand the intrinsic contribution of SHE analytically, a system of 2D electron gas with Rashba type of spin-orbit coupling can be considered [5] [40]:

$$H = \frac{P^2}{2m} - \frac{\lambda}{\hbar}\sigma.(\hat{z} \times \vec{p}) \tag{2.10}$$

Where $P = \hbar k$ is the 2D electron momentum, λ is the Rashba effective coupling constant, σ is the Pauli matrices, m is the mass of the electron effective mass and $\hat{z}$ is the unit vector perpendicular to the 2DEG plane. The illustration of the intrinsic nature of SHE is depicted in the Fig. 2.4. In a translation invariant 2DES (Two Dimensional Electron States), due to SOC, a momentum dependent effective magnetic field causes the spins to align perpendicular to the momenta as shown in the Fig. 2.4 (green arrows). When the external electric field **E** is applied, electrons get acceleration and drift through momentum space at the rate of $\vec{P} = -e\mathbf{E}\hat{x}$. The spin Hall effect arises from the time dependent effective magnetic field experienced by the spins because of their motion in momentum space. It has been shown that the nature of this spin current is purely intrinsic and does not rely on the scattering by impurities[5]. The generated spin current density along the $\hat{y}$ direction is given by [5].

$$j_{s,y} = \int_{\text{annulus}} \frac{d^2\vec{p}}{(2\pi\hbar)^2} \frac{\hbar n_{z,\vec{p}}}{2} \frac{p_y}{m} = \frac{-e}{16\pi\lambda m}(p_{F+} - p_{F-}) \tag{2.11}$$

Where p_{F+} and p_{F-} are the Fermi momenta of the majority and minority spin Rashba bands. When both bands are occupied, the spin Hall conductivity takes the form :

$$\sigma_{SH} = \frac{j_s, y}{E_x} = \frac{e}{8\pi} \tag{2.12}$$

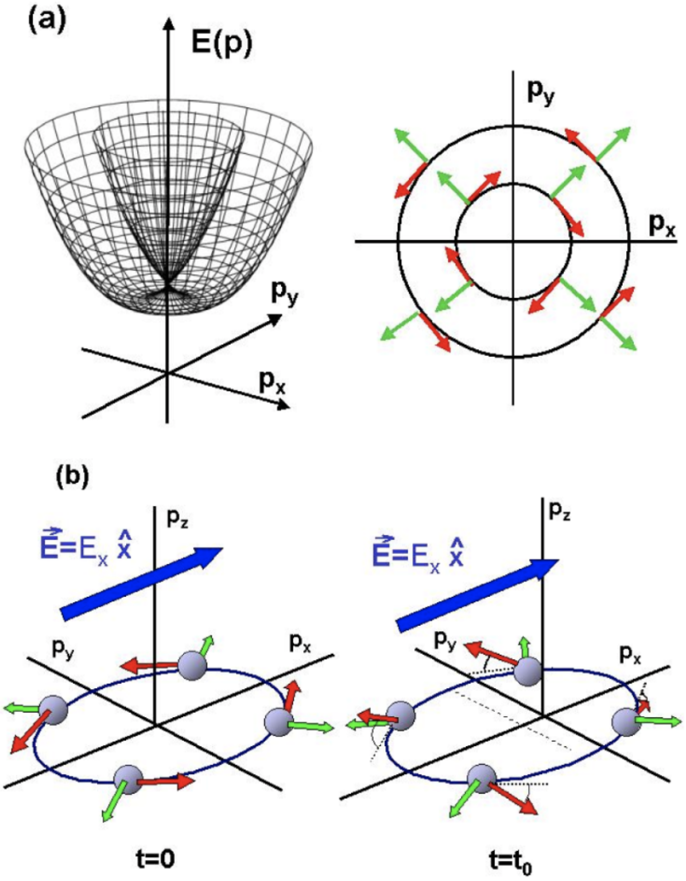

Figure 2.4: a) The 2D electronic eigenstates in a Rashba spin-orbit coupled system are labeled by momentum (green or light gray arrows). For each momentum, the two eigenspinors point in the azimuthal direction (red or dark gray arrows). (b) In the presence of an electric field, the Fermi surface (circle) is displaced an amount $j_e E_x t_0 = hj$ at time t_0 (shorter than typical scattering times). While moving in momentum space, electrons experience an effective torque which tilts the spins up for $p_y > 0$ and down for $p_y < 0$,creating a spin current in the y direction. The figure is taken from ref.[5]

Which is independent of both the Rashba coupling strength and 2DES [5].

2.5.2 Extrinsic Mechanism

The extrinsic mechanism of SHE can be broadly characterized into two parts : **skew-scattering** and **side-jump mechanism**. The skew-scattering mechanism contribution of both SHE directly depends on the Bloch state transport lifetime τ. The skew scattering mechanism of SHE arises from the spin orbit coupling in the disorder potential. This causes the asymmetric chiral contribution to the scattering probability of momenta $\mathbf{k}$ and $\mathbf{k}'$ [4].

$$W^{A}_{\mathbf{k}\mathbf{k}'} \sim (\mathbf{k} \times \mathbf{k}').\mathbf{M} \tag{2.13}$$

Using this transition probability in the Boltzmann equation leads to the longitudinal current proportional to **E** and perpendicular to both **E** and **M**, where the direction of **M** defines the spin polarization in SHE. The corresponding contribution in σ_{xy}^{H-skew} is proportional to longitudinal conductivity σ_{xx} and therefore scattering lifetime τ.

There is another extrinsic mechanism that contributes to SHE is called **Side-jump mechanism**, which is the difference between the total SHE conductivity and the skew and intrinsic contributions. The definition of side-jump contribution within the semi classical theory is as follows : When a Gaussian wave packet scattered from a spherical impurity with spin orbit interaction [The Hamiltonian due to spin orbit coupling, $H_{SO} = \frac{1}{2m^2c^2}(r^{-1}\frac{\partial V}{\partial r}S_zL_z)$]. It's wave vector (**k**) will change by an amount of $\frac{1}{6}\frac{k\hbar^2}{m^2c^2}$ in the transverse direction to **k**. This type of contribution was mentioned by Smit and Berger [41] [42]. The side jump mechanism can be classified further into two parts : intrinsic and extrinsic. These contributions depend on the non spin-orbit and spin-orbit coupled part of the wave packet formed by the Bloch electrons.

2.6 Antiferromagneticic Spintronics

Antiferromagnetic (AF) materials belong to a category of magnetic materials in which the magnetic moments of neighboring atoms are oriented in opposite directions, and therefore they exhibit no net magnetization. The information stored in antiferromagnetic (AF) materials is not influenced by external magnetic fields or perturbations due to the cancellation of the net magnetization. The opposing alignments of neighboring magnetic moments in AF materials result in a zero net magnetization, making them less susceptible to external magnetic fields. Because of this cancellation effect, AF materials exhibit a high degree of stability against external magnetic disturbances. The information stored in AF materials remains preserved even in the presence of external magnetic fields, making them attractive for applications where data integrity and robustness are crucial, such as in magnetic storage devices and magnetic sensors.

Due to strong interaction between neighboring spin sublattices, AF materials also posses large magnon frequencies (typical in THz range) compare to the ferromagnetic materials in which weaker anisotropy results in small magnon frequencies (in GHz range) [43]. Therefore, AF materials are also suitable candidates for writing and reading the information at very short time scale [44]. Antiferromagnetic spintronics can be considered as a subfield of spintronics, in which spin transport, dynamics, and magnetic texture in AF materials are investigated.

2.6.1 Non collinear Antiferromagnets

In collinear antiferromagnets, the AHE vanishes due to the existence of both time-reversal ($\hat{T}$) and crystal symmetry ($\hat{O}$) [9]. Due to the vanishing AHE, collinear AF isn't suitable for reading out signals in spintronics applications. Non-collinear antiferromagnets (NCAF) are a special kind of antiferromagnets in which geometrical frustration leads to the canting of the magnetic moments [45]. Mn_3X (X = Sn, Ge, Ga, Ir, Pt, Rh) are the most common types of compounds that exhibit a non-collinear antiferromagnetic structure [45][6] [46].

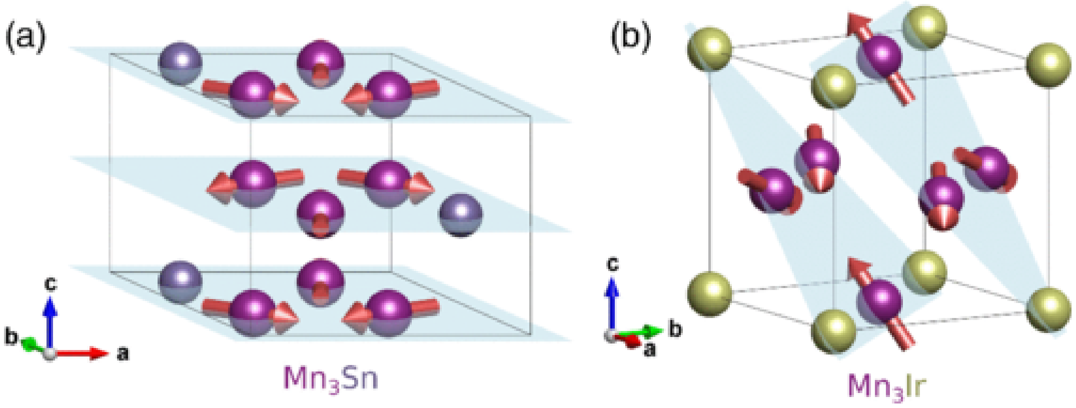

Figure 2.5: Crystal and magnetic structure of (a) Mn_3Sn (as well as Mn_3Ge and Mn_3Ga) (b) Mn_3Ir (as well as Mn_3Pt and Mn_3Rh). The Fig. is adapted from ref [6]

The crystal and magnetic structures of Mn_3Sn and Mn_3Ir are shown in Fig. 2.5. In Mn_3Sn, a non-collinear antiferromagnetic order is observed in the hexagonal crystal structure (with space group $P6_3/mmc$), and the antiferromagnetic ordering persists up to 420K

(Néel temperature T_N). As seen in Fig. 2.5, the Mn atoms exhibit a 120° orientation from each other due to geometrical frustration. Although the total moments are compensated, they align along the same axis. This type of magnetic moment arrangement is referred to as non-collinear antiferromagnetism. On the other hand, Mn_3Ir exhibits antiferromagnetic ordering in a cubic crystal structure (with space group $Pm-3m$, 221), with a kagome plane along the (111) directions. It also has a high Néel temperature of 730K [47]. Due to its large T_N and the presence of the exchange bias effect, Mn_3Ir it has been utilized in spin valve structures for spintronics applications [48].

Furthermore, it is important to highlight the difference in spin textures between hexagonal and cubic crystal symmetries. In Mn_3Sn, the magnetic moments lie in the (0001) basal plane, as illustrated in Fig. 2.6. If we consider the Mn atoms in a clockwise direction, the corresponding magnetic moments will rotate by 120° in the counterclockwise direction compared to the previous moment. This spin texture is referred to as the **inverse triangular spin texture**. Conversely, in the cubic structure of Mn_3Ir, if we consider the Mn atoms in a clockwise direction, the corresponding magnetic moment will rotate by 120° from the previous moment in the same clockwise direction. This spin texture is known as the **triangular spin texture**.

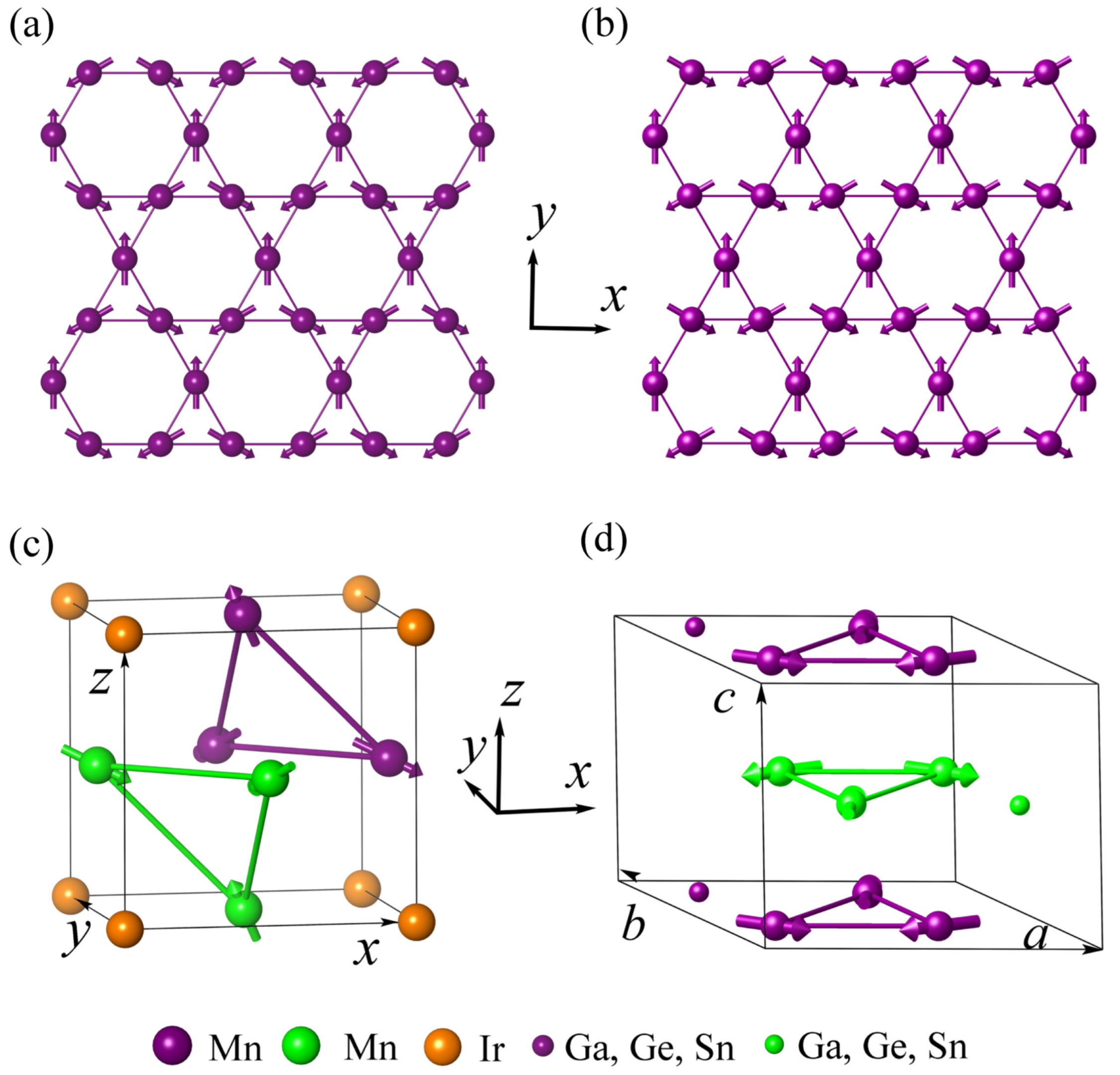

Figure 2.6: (a) (b) The triangular and inverse triangular spin textures in cubic Mn_3Ir and hexagonal Mn_3Sn crystal structure. (c) and (d) shows respective crystal structures. The Fig. is adapted from ref [7].

Although these spin structures are different in cubic and hexagonal compounds, both exhibit **chirality** or handedness. This means that the magnetic properties of the system depend on the direction of rotation through the spin texture. For instance, in the clockwise rotation, the spins follow a tail-to-head configuration, while in the anticlockwise rotation, they follow a head-to-tail configuration, as shown in Fig. 2.6. When the spin textures are reversed, the chirality is also reversed [49]. The specific chirality of the magnetic structure is determined by the **Dzyaloshinskii–Moriya interaction** (DMI), which is an antisymmetric exchange interaction between neighboring spins. The term in the Hamiltonian associated with the DMI can be expressed as:

$$\mathrm{H_{DMI}} = \mathbf{D}_{\mathrm{ij}}.(\mathbf{S}_{\mathrm{i}} \times \mathbf{S}_{\mathrm{j}}) \tag{2.14}$$

$\mathbf{D}_{\mathrm{ij}}$ is a vector that determines the strength of the DMI, with its direction pointing out of the plane containing the $\mathbf{S}_{\mathrm{i}}$ and $\mathbf{S}_{\mathrm{j}}$ moments. The DMI promotes the canting of magnetic moments, causing $\mathbf{S}_{\mathrm{i}}$ and $\mathbf{S}_{\mathrm{j}}$ to be oriented at an angle. Thus, the presence of DMI introduces chirality in the system.

Due to the chirality in the spin structure, when conduction electrons hop onto chiral spin sites, their quantum mechanical amplitude (or wave function) acquires a complex phase factor known as the **Berry phase**. The Berry phase manifests itself as an internal magnetic field in reciprocal space, giving rise to the anomalous Hall effect (AHE) and spin Hall effect (SHE) (which will be explained in the next section) even in the absence of spontaneous magnetization and SOC. It is worth noting that in ferromagnets, the transverse resistivity scales linearly with the saturation magnetization ($\rho_{\mathrm{H}} = \mathrm{R_0 B} + 4\pi \mathrm{R_s M_s}$), whereas in non-collinear antiferromagnets, the Berry phase alone can induce the anomalous Hall effect[1].

2.6.2 AHE in Non-Collinear Antiferromagnet

Hall effect directly probes the electronic states at the Fermi level, and its ordinary part ($\propto \mathbf{B}$) represents the measurement of the Fermi volume, which is the volume in momentum space enclosed by the Fermi sphere. In ferromagnets (FM), an additional contribution comes from the magnetic order, known as the extraordinary or anomalous Hall effect [50].

$$\rho_{\mathrm{xy}} = \mathrm{R_0 B_z} + \rho_{\mathrm{xy}}^{\mathrm{AHE}} \tag{2.15}$$

Here, $\mathrm{R_0}$ is the ordinary Hall coefficient, $\mathrm{B_z}$ is the applied magnetic field in the out-of-plane direction, and $\rho_{\mathrm{xy}}^{\mathrm{AHE}}$ is the anomalous Hall resistivity. Equation 2.15 is valid when the cyclotron frequency (ω_{c}) is much smaller than the scattering rate (τ^{-1}) of carriers ($\mathrm{R_0 B_z} <<$

---

[1] In ferromagnets, the presence of spontaneous magnetization and SOC contribute to the AHE. However, in non-collinear antiferromagnets, the Berry phase induced by chirality can give rise to the AHE even in the absence of spontaneous magnetization.

ρ_{xx}). In ferromagnets, the anomalous Hall effect arises as a direct consequence of the broken time reversal symmetry and spin-orbit coupling (SOC) [51]. The SOC leads to spin-dependent scattering of spin-up and spin-down electrons, resulting in different populations inside a ferromagnet depending on their spin direction. This creates an asymmetric charge accumulation at the opposite edges of the sample, giving rise to a transverse electric field, i.e., the Hall voltage (V_H).

In the earlier section, we mentioned that due to geometrical frustration, spin textures become chiral in non-collinear antiferromagnets. The chirality of the spin texture can be described by two means: the **vector spin chirality** ($k = (S_i \times S_j)$) and the **scalar spin chirality** ($k = S_i.(S_j \times S_k)$) (where indices i, j, and k are the lattice sites) [52]. The vector and scalar chiral orders of spins are direct results of DMI without an inversion center and can be used as order parameters in frustrated ferromagnets and antiferromagnets [52]. The vector chirality is introduced in the context of coplanar arrangements of chiral spin textures, while the scalar chirality is used to describe non-coplanar chiral spin textures [52].

Now let's consider the case when an itinerant electron hops along a closed loop (1 → 2 → 3 → 1) in a chiral spin texture. Its wave function acquires a phase that corresponds to the total angle subtended by the three spins in three dimensions [8]. This phase is known as the Berry phase and can arise from either vector chirality or scalar chirality. In the case of vector chirality (when spin textures are coplanar), this Berry phase is known as the **momentum space Berry phase** (γ(k)). For a closed path in momentum space, it can be defined as:

$$\gamma_n \mathbf{k} = i \oint_C d\mathbf{k}.\, \langle n\mathbf{k}|\nabla_{\mathbf{k}}|n\mathbf{k}\rangle = \oint_C A_n(\mathbf{k}).d\mathbf{k} \tag{2.16}$$

Where $A_n(\mathbf{k}) = i\,\langle n\mathbf{k}|\nabla_{\mathbf{k}}|n\mathbf{k}\rangle$ is a vector-valued function known as the Berry connection or otherwise known as Berry potential. Using Stoke's theorem, it can be seen as

$$\oint_C A_n(\mathbf{k}).d\mathbf{k} = \oint_S \nabla \times A_n(\mathbf{k})d\mathbf{S} \tag{2.17}$$

The pseudo vector $\Omega_n(\mathbf{k}) = (\nabla \times A_n(\mathbf{k}))$ is known as **Berry curvature** in momentum space [53]. This Berry curvature acts as a fictitious magnetic field in momentum space

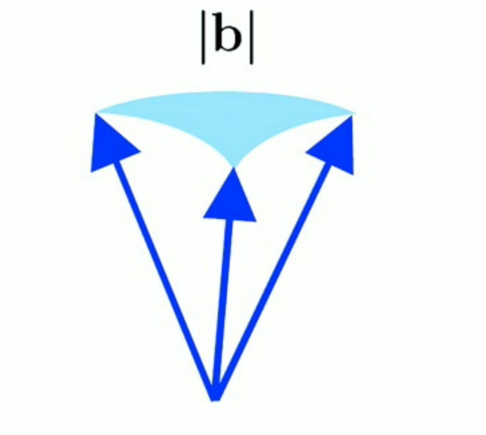

Figure 2.7: Surface enclosed by the canted spins. The Fig. is adapted from [8].

The fictitious magnetic field exerts a Lorentz force on the charge carriers, deflecting their paths in the transverse direction and changing the direction of their momentum. This deflection gives rise to the Hall voltage. The magnetic field induced by the momentum space Berry phase can be as high as 100T [54], resulting in strong deflection of the charge carriers from their initial trajectories. The Berry phase induces the anomalous Hall effect and contributes to the intrinsic part of the anomalous Hall conductivity.

The intrinsic contribution of the anomalous Hall conductivity can be calculated by integrating the orbital polarization (OP) of the momentum Berry curvature of Bloch electrons $\Omega_n(\mathbf{k})$ over the entire Brillouin zone (BZ) [55].

$$\sigma_{xy}^{AHE} = \frac{e^2}{\hbar} \int_{BZ} \frac{d\mathbf{k}}{2\pi^3} \sum f(\mathbf{k}) \Omega_n(\mathbf{k}) \tag{2.18}$$

It is important to note that the momentum Berry phase is a direct consequence of the non-collinearity of the magnetic ordering, which in turn breaks the time reversal symmetry in the system. As a result, even in the absence of net magnetization and spin-orbit coupling, the intrinsic anomalous Hall effect arises in non-collinear antiferromagnets due to the broken time reversal symmetry caused by the long-range magnetic ordering.

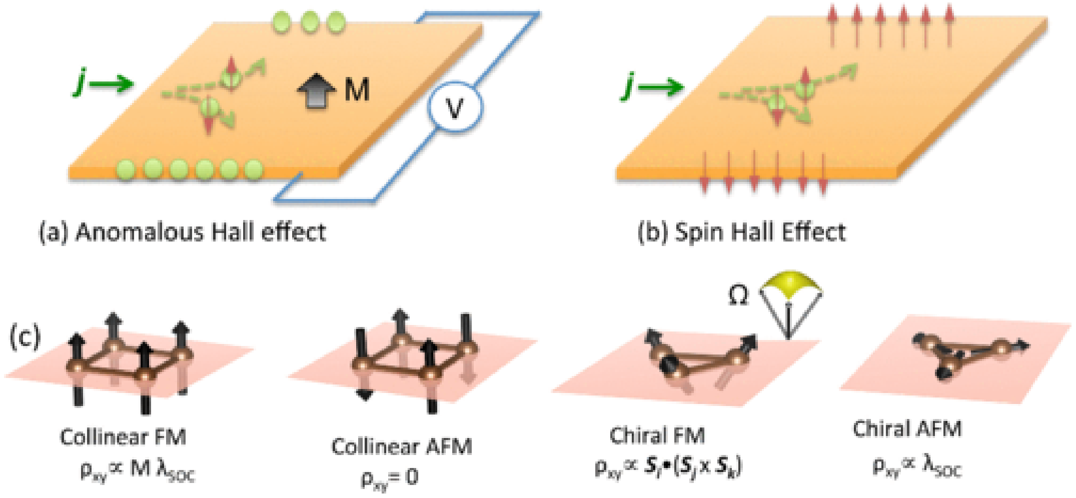

Figure 2.8: Schematic illustrations of (a) AHE and, (b) SHE from the viewpoint of spin-dependent Mott scattering. (c) AHE in collinear FM, collinear AFM, chiral FM, and chiral AFM systems. The Fig. is taken from [9].

2.6.3 SHE in Non-Collinear Antiferromagnet

In this section, spin Hall effect (SHE) in non collinear antiferromagnet will be discussed, in particular Berry phase driven intrinsic SHE. Similar to AHE, the intrinsic contribution of spin Hall conductivity (SHC) can be obtained from the linear response theory [9].

$$\sigma^{\gamma}_{\alpha\beta} = \frac{e}{\hbar}\sum_{n}\int_{BZ}\frac{d^3\mathbf{k}}{(2\pi)^3} f_n(\mathbf{k})\Omega^{\gamma}_{n,\alpha\beta}(\mathbf{k}) \tag{2.19}$$

$$\Omega^{\gamma}_{n,\alpha\beta}(\mathbf{k}) = 2i\hbar^2 \sum_{m\neq n}\frac{\langle u_n(\mathbf{k})|J^{\gamma}_{\alpha}|u_n(\mathbf{k})\rangle\,\langle u_n(\mathbf{k})|v_{\beta}|u_n(\mathbf{k})\rangle}{(E_n(\mathbf{k})-E_m(\mathbf{k}))^2} \tag{2.20}$$

Where $\Omega^{\gamma}_{n,\alpha\beta}(\mathbf{k})$ is the spin Berry curvature, $\sigma^{\gamma}_{\alpha\beta}$ is the spin Hall conductivity tensor, which is a third order tensor and related to the generated spin current $J^{\gamma}_{\alpha\beta}$ via electric field E_{β}. The notation $J^{\gamma}_{\alpha\beta}$ represents the spin current flows along α the direction with the polarization axis along the γ direction and E_{β} is the component of electric field $\vec{E}$ $(\alpha, \beta, \gamma = x, y, z)$. The intrinsic contribution of SHC is determined by the electronic band structure, which are fully compilable with the symmetry in the Hamiltonian.

Based on the crystal and magnetic symmetries of Mn_3X compounds, we would classify the discussion into two parts. Mn_3Sn, Mn_3Ga and Mn_3Ge compounds shows hexagonal crystal symmetry with space group $P6_3/mmc$, in each primitive unit cell Mn_3X planes are stacked along c axis according to "-**AB**-**AB**-" structure and in each structure Kagome type lattice is formed with Ga, Ge, and Sn situated at the center of hexagon formed from the Mn atoms. Due to the geometrical frustration, Mn moments are canted at 120° from each other in the same plane. On the other hand, compounds like Mn_3Rh, Mn_3Ir and Mn_3Pt shows cubic crystal symmetry (face centered lattice) with space group Pm3m, in which atoms Ir (Rh, Pt) sits on the face center while Mn atoms are lying on the corner of the cube. In the cubic structure, within (111) plane Mn atoms forms the Kagome lattice and stack along "-**ABC** -**ABC**-" sequence.

2.6.4 SHE in Mn_3X, X = Ga, Sn and Ge

The magnitude and direction of SHE can be explained by the SHC (Spin Hall Conductivity) tensor. The Intrinsic SHC tensor depends on the electronic band structure, which in turn relies on the symmetries in Hamiltonian. Similar to AHC tensor, some elements of intrinsic SHC tensor will be zero based on the magnetic and lattice symmetries of the compound. For Mn_3X, X = Ga, Sn, and Ge, the magnetic space group is $R\bar{3}m'$ and the corresponding Laue group is m'm'm'[9]. The table 2.1 summarizes the shape of intrinsic SHC tensor and the corresponding numerical values. It can be inferred from the table 2.1 that SHC is anisotropic, i.e., the magnitude of the spin current depends on the flow of the charge current with respect to the crystallographic plane. For example, we take the case of $h-Mn_3Ge$, which is shown in Fig. 2.9.

Here we set the kagome plane in xy plane, if the charge current J flows in x direction then the corresponding spin current J_S will have maximum amplitude along the y direction and minimum amplitude along z direction. Therefore, in order to observe the largest SHE, the charge current needs to be set in the kagome plane, which is also evident in the table 2.1 only σ^z_{xy} and σ^z_{yx} dominated and rest of the elements are zero (SHC« 12 $\frac{\hbar}{e}$).

	σ_x	σ_y	σ_z
symmetry-imposed tensor shape	$\begin{pmatrix} 0 & 0 & 0 \\ 0 & 0 & \sigma^x_{yz} \\ 0 & \sigma^x_{zy} & 0 \end{pmatrix}$	$\begin{pmatrix} 0 & 0 & \sigma^y_{xz} \\ 0 & 0 & 0 \\ \sigma^y_{zx} & 0 & 0 \end{pmatrix}$	$\begin{pmatrix} 0 & \sigma^z_{xy} & 0 \\ \sigma^z_{yx} & 0 & 0 \\ 0 & 0 & 0 \end{pmatrix}$
Mn_3Ga	$\begin{pmatrix} 0 & 0 & 0 \\ 0 & 0 & -14 \\ 0 & 12 & 0 \end{pmatrix}$	$\begin{pmatrix} 0 & 0 & 15 \\ 0 & 0 & 0 \\ -7 & 0 & 0 \end{pmatrix}$	$\begin{pmatrix} 0 & -597 & 0 \\ 626 & 0 & 0 \\ 0 & 0 & 0 \end{pmatrix}$
Mn_3Ge	$\begin{pmatrix} 0 & 0 & 0 \\ 0 & 0 & -21 \\ 0 & 18 & 0 \end{pmatrix}$	$\begin{pmatrix} 0 & 0 & 21 \\ 0 & 0 & 0 \\ -18 & 0 & 0 \end{pmatrix}$	$\begin{pmatrix} 0 & 112 & 0 \\ -115 & 0 & 0 \\ 0 & 0 & 0 \end{pmatrix}$
Mn_3Sn	$\begin{pmatrix} 0 & 0 & 0 \\ 0 & 0 & -36 \\ 0 & 96 & 0 \end{pmatrix}$	$\begin{pmatrix} 0 & 0 & 36 \\ 0 & 0 & 0 \\ -96 & 0 & 0 \end{pmatrix}$	$\begin{pmatrix} 0 & 64 & 0 \\ -68 & 0 & 0 \\ 0 & 0 & 0 \end{pmatrix}$

Table 2.1: The intrinsic SHC tensors and numerical values of SHC for Mn_3Ga, Mn_3Ge and Mn_3Sn, elements of SHC tensors are considered to be zero when they are less than 12 $\frac{\hbar}{e}(\Omega\text{cm})^{-1}$. The value in the table is adapted from ref [9]

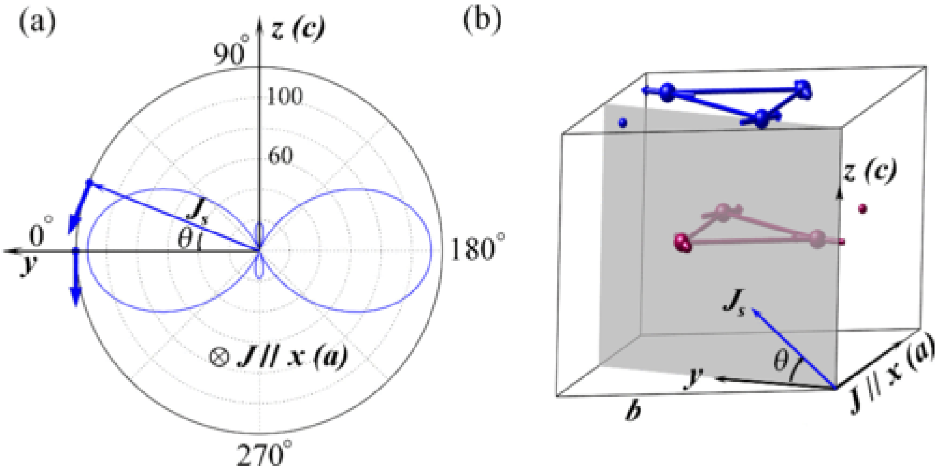

Figure 2.9: (a) Anisotropy in spin current in Mn_3Ge : spin current J_S arising due to the flow of charge current J along x-axis. The value of J_S inside a YZ plane, the largest and smallest SHC occurs for θ = 0° (y-axis) and θ = 90° (z-axis) respectively. (b) Direction of J_S and J with respect to Kagome plane in Mn_3Ge. The Fig. is adapted from [9].

2.6.5 SHE in $\mathrm{Mn_3X}$, X = Rh, Ir and Pt

In the cubic lattice of $\mathrm{Mn_3X}$ (X = Rh, Ir, and Pt), there are three mirror planes that are related to each other by a threefold rotation and intersect the [111] crystallographic plane [9]. In the Kagome plane, the mirror reflection $\hat{\mathbf{M}}$ preserves the lattice symmetry but reverses the magnetic moments, and the time-reversal $\hat{\mathbf{T}}$ also reverses the moments. Therefore, the system preserves the symmetries with respect to $\hat{\mathbf{T}}\hat{\mathbf{M}}$ operations. For symmetry analysis, we set the Kagome plane in the xy plane and the z direction along the [111] direction. The magnetic space group for $\mathrm{Mn_3X}$ (X = Rh, Ir, and Pt) is $\mathrm{Am'm'm2}$, which provides information about the shape of the spin Hall conductivity (SHC) tensor. The non-zero components of the SHC tensor are $\sigma^{\mathrm{x}}_{\mathrm{yz}}$ ($\sigma^{\mathrm{y}}_{\mathrm{xz}} = \sigma^{\mathrm{x}}_{\mathrm{yz}}$) and $\sigma^{\mathrm{y}}_{\mathrm{xy}}$ ($\sigma^{\mathrm{y}}_{\mathrm{xy}} = \sigma^{\mathrm{y}}_{\mathrm{yx}} = -\sigma^{\mathrm{x}}_{\mathrm{xx}} = \sigma^{\mathrm{x}}_{\mathrm{yy}}$), as shown in Table 2.2. Similar to the anomalous Hall conductivity, the SHC in non-collinear antiferromagnets is also anisotropic, meaning that the magnitude of the spin current depends on the experimental configuration (i.e., the flow of charge current with respect to the crystal symmetry).

It is worth noting that the SHC tensor reveals that the charge current J, spin current $\mathrm{J_S}$, and spin polarization do not have to be perpendicular to each other, as indicated by the non-zero value of $\sigma^{\mathrm{x}}_{\mathrm{xx}}$. This type of spin current is known as a **longitudinal spin current**, in which conduction electrons are naturally spin-polarized. This phenomenon is common in ferromagnetic metals. The ability of non-collinear antiferromagnets to generate longitudinal spin currents makes them promising candidates for novel spintronic applications. Figure 2.10 shows the angle-dependent SHC in $\mathrm{Mn_3Ir}$, where the charge current is flowing along the [-110] crystallographic direction (J||x according to convention). The associated SHC exhibits minimum and maximum values of 7 $\frac{\hbar}{e}(\Omega\mathrm{cm})^{-1}$ and 215 $\frac{\hbar}{e}(\Omega\mathrm{cm})^{-1}$ along the [111] (i.e., z-axis) and [001] planes, respectively. This variation of SHC (or θ_{SH}) in $\mathrm{Mn_3Ir}$ has been experimentally verified [56].

	σ_x	σ_y	σ_z
symmetry-imposed tensor shape	$\begin{pmatrix} \sigma^x_{xx} & 0 & 0 \\ 0 & -\sigma^x_{xx} & \sigma^x_{yz} \\ 0 & \sigma^x_{zy} & 0 \end{pmatrix}$	$\begin{pmatrix} 0 & -\sigma^x_{xx} & -\sigma^x_{yz} \\ -\sigma^x_{xx} & 0 & 0 \\ \sigma^x_{zy} & 0 & 0 \end{pmatrix}$	$\begin{pmatrix} 0 & \sigma^z_{xy} & 0 \\ -\sigma^z_{xy} & 0 & 0 \\ 0 & 0 & 0 \end{pmatrix}$
Mn_3Rh	$\begin{pmatrix} -276 & 0 & 0 \\ 0 & 276 & 220 \\ 0 & 70 & 0 \end{pmatrix}$	$\begin{pmatrix} 0 & 276 & -220 \\ 276 & 0 & 0 \\ -70 & 0 & 0 \end{pmatrix}$	$\begin{pmatrix} 0 & 145 & 0 \\ -145 & 0 & 0 \\ 0 & 0 & 0 \end{pmatrix}$
Mn_3Ir	$\begin{pmatrix} -210 & 0 & 0 \\ 0 & 210 & 299 \\ 0 & -7 & 0 \end{pmatrix}$	$\begin{pmatrix} 0 & 210 & -299 \\ 210 & 0 & 0 \\ 7 & 0 & 0 \end{pmatrix}$	$\begin{pmatrix} 0 & 163 & 0 \\ -163 & 0 & 0 \\ 0 & 0 & 0 \end{pmatrix}$
Mn_3Pt	$\begin{pmatrix} -66 & 0 & 0 \\ 0 & 66 & 108 \\ 0 & 7 & 0 \end{pmatrix}$	$\begin{pmatrix} 0 & 66 & -108 \\ 66 & 0 & 0 \\ -7 & 0 & 0 \end{pmatrix}$	$\begin{pmatrix} 0 & 32 & 0 \\ -32 & 0 & 0 \\ 0 & 0 & 0 \end{pmatrix}$

Table 2.2: The intrinsic SHC tensors and numerical values of SHC for Mn_3Rh, Mn_3Ir and Mn_3Pt, elements of SHC tensors are considered to be zero when they are less than 12 $\frac{\hbar}{e}(\Omega cm)^{-}1$. The value in the table is adapted from ref [9]

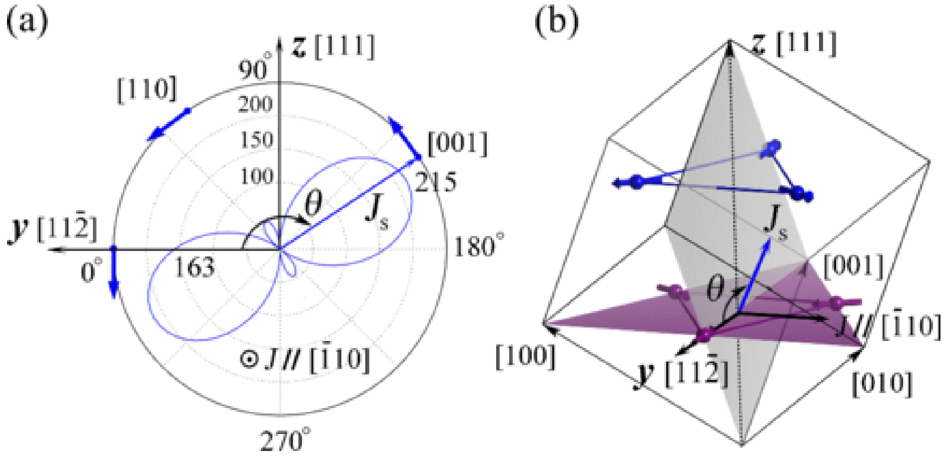

Figure 2.10: (a) Variation of SHC with respect to angle in yz plane for Mn_3Ir, the charge current J flows along x axis i.e., [1-10], the SHC is largest along [001] and smallest [111] plane. (b) Direction of J and J_S within the crystal structure. The figure is adapted from [9].

2.7 Mn_3Pt

Mn_3Pt is a cubic non-collinear antiferromagnet with a lattice constant of a = 3.833 Å and a Néel temperature $T_N \approx 475$ K [57]. It has a face-centered cubic (fcc) crystal structure, with Mn atoms located at face-centered positions. At room temperature, similar to Mn_3Ir, the magnetic moments of Mn atoms form a **triangular spin texture**. Due to geometrical frustration, the moments are canted at 120° from each other, creating a Kagome plane [58].

The magnetic structure of Mn_3Pt exhibits symmetry, which results in non-zero momentum space Berry phase for Bloch electrons. This leads to the presence of anomalous Hall effect (AHE) and magneto-optical Kerr effect (MOKE) even in the absence of net magnetization [59] [60]. The magnetic symmetry in Mn_3Pt also generates out-of-plane spin polarization (σ_z), which is useful for magnetization switching in perpendicular magnetized ferromagnetic films. This property makes Mn_3Pt a promising candidate for spintronics applications [61] [62] [63]. At 360K, Mn_3Pt exhibits first order magnetic phase transition between low temperature non collinear spin texture (**D-phase**) and high temperature collinear AFM (**F-phase**) (shown in Fig. 2.11a and 2.11b) [64].

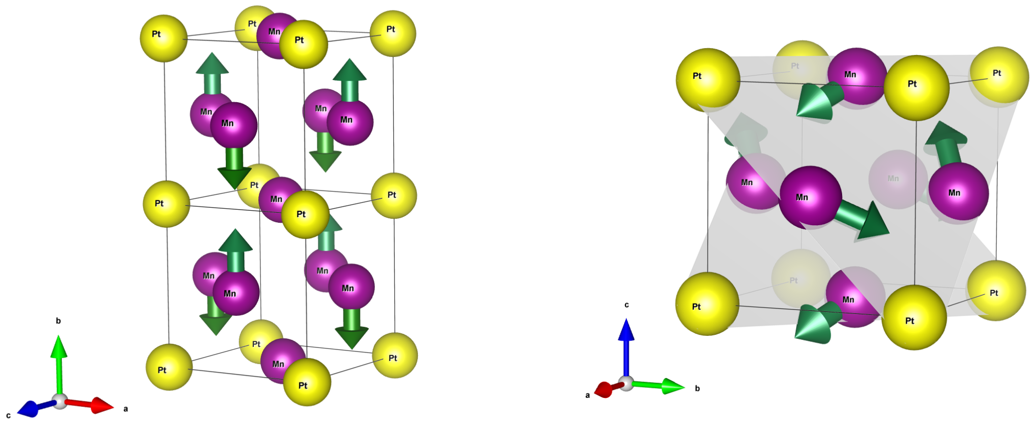

(a) F Phase

(b) D Phase

Figure 2.11: (a) High-temperature F phase of Mn_3Pt shows collinear spin texture and (b) while relatively low temperature (< 360K) D phase exhibits non-collinear spin texture. The crystal structure is made with the help of VESTA software.

The non-collinear D phase of Mn_3Pt exhibits two types of domain configurations: T_1 and T_2, as shown in Fig. 2.12a and 2.12b. In the T_1 configuration, the magnetic moments of Mn atoms are aligned either head to head or tail to tail. On the other hand, in the T_2 configuration, the moments are aligned head to tail or tail to head. The energy difference between these two configurations is very small [57].

In Mn_3Pt with the T_1 domain configuration, a robust anomalous Hall effect (AHE) is observed. However, the T_2 configuration lacks AHE due to the magnetic symmetry of this configuration [63].

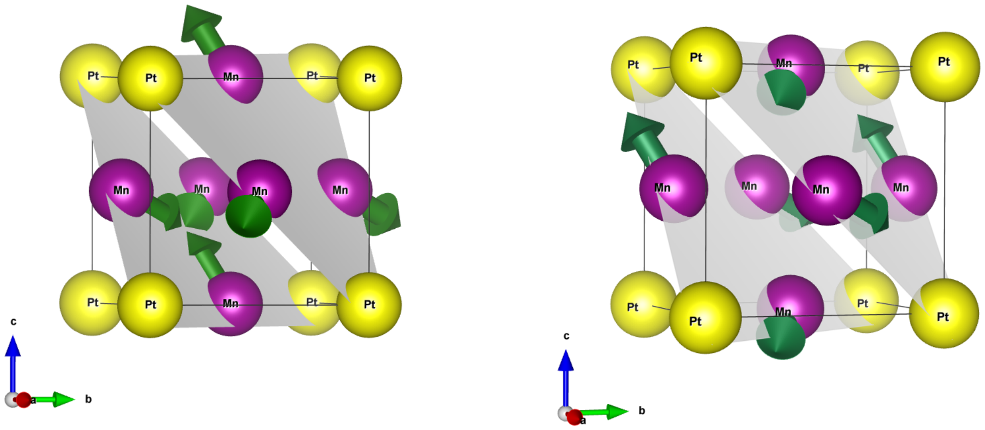

(a) T_1 domain configuration of Mn_3Pt.

(b) T_2 domain configuration of Mn_3Pt.

Figure 2.12: Different domain configuration of Mn_3Pt. The crystal structure was drawn with the help of VESTA software.

3

Experimental Methods

3.1 Introduction

In this chapter, the experimental methods utilized in the thesis are presented. These methods encompass sample preparation techniques such as magnetron sputtering, as well as fundamental sample characterization techniques like X-ray diffraction (XRD), Atomic Force Microscopy (AFM), and the use of specific measurement devices such as the Superconducting Quantum Interference Device (SQUID) and the Physical Property Measurement System (PPMS) from Quantum Design Inc. In the final section of the chapter, the home built setups Optically Detected Ferromagnetic Resonance (OFMR) and Spin-Transfer Ferromagnetic Resonance (STFMR) are discussed.

3.2 Sample preparation technique-Magnetron Sputtering

The samples discussed in this thesis are grown using the magnetron sputtering technique. To understand the magnetron sputtering process, it is important to describe the basic phenomena involved. The term "sputtering" originates from the French word "pulvérisation," which refers to the vaporization of atoms from a surface through bombardment by foreign ions or atoms. The deposition of these sputtered atoms onto another surface, typically a substrate, is known as sputtered deposition.

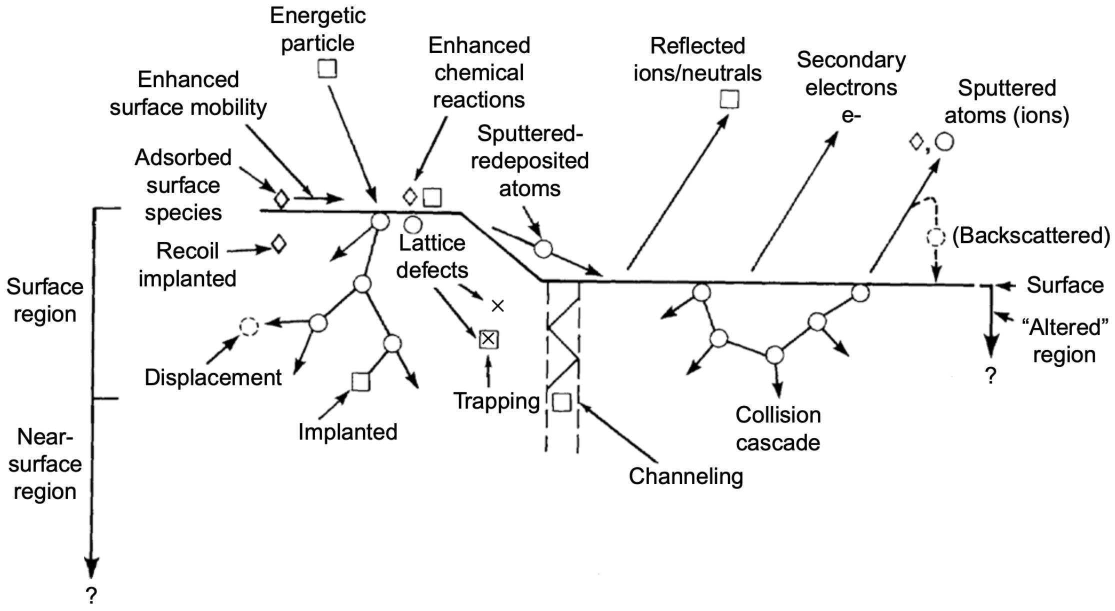

Figure 3.1: Events that occur during the sputtering process. The figure is taken from [10]

Sputter deposition is typically performed under a good base vacuum (less than 10^{-5} Torr) with a low or high-pressure gas environment (5-50 mTorr), where the sputtered atoms travel from the target surface (the source of the atoms) to the desired substrate. The typical processes involved during sputtering are illustrated in Figure 3.1. The ratio of sputtered atoms to the incident ions is known as the sputtering yield, which depends on various factors such as the incidence angle and mass of the bombarding atoms.

There are different configurations of sputtering, with the most common being plasma-based sputtering. In plasma-based sputtering, a plasma is created between the cathode (target) and anode (substrate). Positive ions generated in the plasma are accelerated towards the target, which is held at a negative potential with respect to the plasma, initiating the sputtering process. Within the plasma configuration, different types of sputtering can be categorized based on the nature of the applied potential to the target.

- DC/Diode Sputtering
- AC Sputtering
- Radio Frequency (RF) Sputtering
- Magnetron Sputtering (DC/RF)

In diode sputtering, a negative DC potential is applied to the target, while the substrate is held at a positive potential or ground potential. It is important for the target in DC sputtering to be an electrical conductor because an insulating surface would develop a surface charge that would hinder further sputtering. The sputtering rate is usually slower in DC sputtering.

In AC sputtering, the potential is periodically reversed between the target and substrate. AC sputtering is typically considered to occur at frequencies below 50 kHz. At frequencies above 500 kHz, it is referred to as RF (radio frequency) sputtering. In RF sputtering, the ions do not have enough mobility to behave like in DC sputtering, and the applied potential is spread uniformly between the electrodes. During the first half of the RF cycle, ions are accelerated towards the target, causing sputtering. In the second half of the cycle, electrons in the plasma reach the target and prevent the buildup of charges on the target. Therefore, RF sputtering is suitable for both insulating and conducting targets. Typical frequencies for RF sputter deposition range from 0.5 to 30 MHz, with 13.56 MHz being a commonly used standard frequency [10].

In magnetron sputtering, a magnetic field is applied behind the target. The Lorentz force acting on electrons leads to a high flux of electrons, creating a high-density plasma, from which ions can be extracted to sputter the target uniformly and at relatively higher sputtering rates. Both DC and RF potentials can be applied in magnetron sputtering. The main advantage of magnetron sputtering is that the high-density plasma allows for higher sputtering rates.

3.3 Sample Characterization Techniques

In this section sample characterization techniques such as X-ray diffraction (XRD), Atomic Force Microscopy (AFM), SQUID (Superconducting Quantum Interference Device), PPMS (Physical Property Measurement System) are discussed.

3.3.1 X-Ray Diffraction (XRD)

X-ray Diffraction (XRD) is an analytical technique used to study the crystal structure and composition of materials. The basic principle of X-ray Diffraction is as follows: X-rays are electromagnetic waves with wavelengths on the order of a few Å, which is comparable to the distance between atomic planes in crystalline solids. When X-rays interact with the atoms in a crystalline solid, the scattered beams undergo constructive interference.

In XRD, a beam of X-rays is directed at a crystal, and the scattered X-rays are detected. Figure 3.2 illustrates a beam of X-rays scattered by atomic planes inside a crystal. Rays 1 and 2 represent X-rays scattered by atoms K and L, respectively. The path difference between these two rays can be expressed as follows:

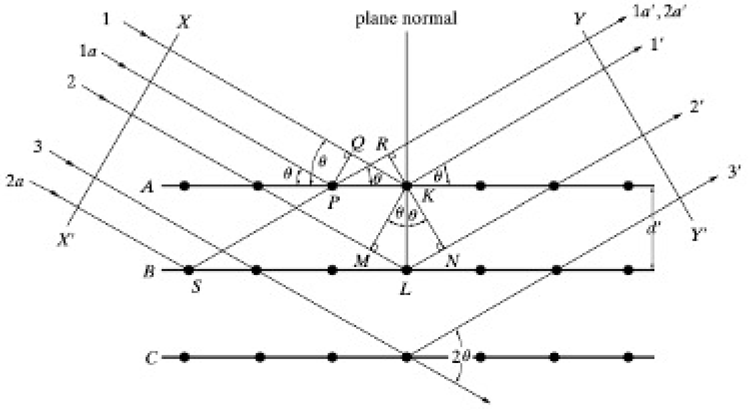

Figure 3.2: Diffraction of X-rays from the atomic planes inside a crystal. The Fig. is taken from [11]

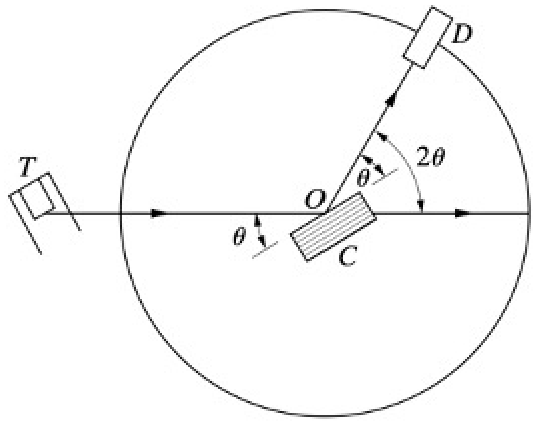

Figure 3.3: Schematic of X-ray spectrometer. The Fig. is taken from [11]

$$\mathrm{ML} + \mathrm{LN} = 2\mathrm{d}'\sin\theta \tag{3.1}$$

Where d′ is the distance between the atomic planes and θ is the angle of incidence (or angle of reflection). In order to have the constructive interference, this path difference must be an integer multiple of the wavelength. Therefore

$$\mathrm{n}\lambda = 2\mathrm{d}'\sin\theta \tag{3.2}$$

The number n is the order of the diffraction, and this relation is known as Bragg's law (named after British scientist W.L.Bragg). Bragg's law can be applied experimentally in two ways. Using x-rays of known wavelength and measuring θ of different atomic planes with different spacing d′ in a crystal, this analysis is called structure analysis. Alternatively, with known spacing d′ of atomic planes and reflection angle (θ), determining the wavelength of X-rays. The instrument used for this procedure is known as x-ray spectrometer (as shown in 3.3). In X-ray spectrometer, X-rays come from the tube T, incident on a crystal C which is set at any desired angle with respect to the incoming beam, by rotation about an axis through O. D is the detector which measure the intensity of reflected X-rays and can also be rotated about O and set at any desired angular position as shown in Fig. 3.3. Generally, for structure analysis, the intensity (I) vs angle (2θ) is measured.

3.3.2 Atomic Force Microscopy (AFM)

Atomic Force Microscopy (AFM) is a surface sensitive technique which is capable of producing three-dimensional images of a surface with an atomic resolution of 10^{-10} m. The basic principle of AFM is as follows, when a sharp tip is brought to the sample, the interatomic potentials are developed between the atoms of a tip and the atoms of a surface. This sharp tip is integrated to the cantilever, when the sample moves horizontally in X-Y direction, the interatomic forces cause the cantilever to move up and down in Z direction, the position of the cantilever can be recorded by the sending a diode laser on it, which deflects the laser onto a position sensitive photodetector. Therefore, by recording the position of the cantilever while moving the sample in X-Y direction, a three-dimensional topography of the sample can be constructed.

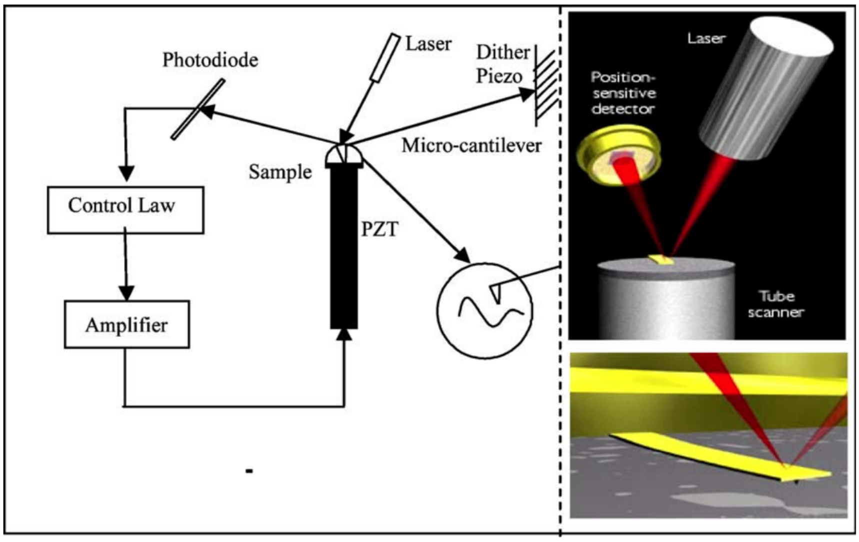

Figure 3.4: Schematic of AFM instrument. The Fig. is taken from [12].

3.3.3 Superconducting Quantum Interference Device (SQUID)

Superconducting Quantum Interference Device (SQUID) is one of the sophisticated instruments to measure the magnetic flux, It can measure the magnetization as low as 10^{-14} T. SQUID utilizes the Josephson effect to measure the tiny changes in magnetic flux [65]. Typically, SQUID consists of one or two Josephson junctions (DC or RF) in a superconducting loop (Fig. 3.5). The working principle of SQUID is as follows, when a bias current (I_B) is applied to the superconducting loop, it splits into two parts (each half side of the loop carries $I_B/2$ current). Inductively coupled magnetic field to the SQUID loop creates screening currents ($I_{loop} = \Phi/L_{loop}$, Where L_{loop} is the inductance of the loop). The amount of the screening current will increase or decrease, depending on the direction of the induced flux, therefore the voltage drop at the Josephson junction will also change. This voltage change at the Josephson junction is periodic with respect to the quantum magnetic flux (Φ_0) (Fig.3.6). Measuring the change in voltage allows the quantification of the magnetic flux (or magnetization due to the sample) coupled to the superconducting loop.

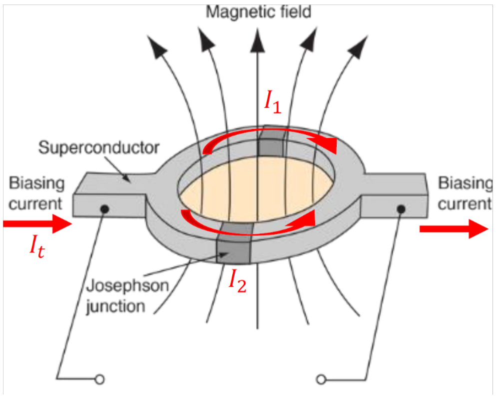

Figure 3.5: Schematic of SQUID instrument [13].

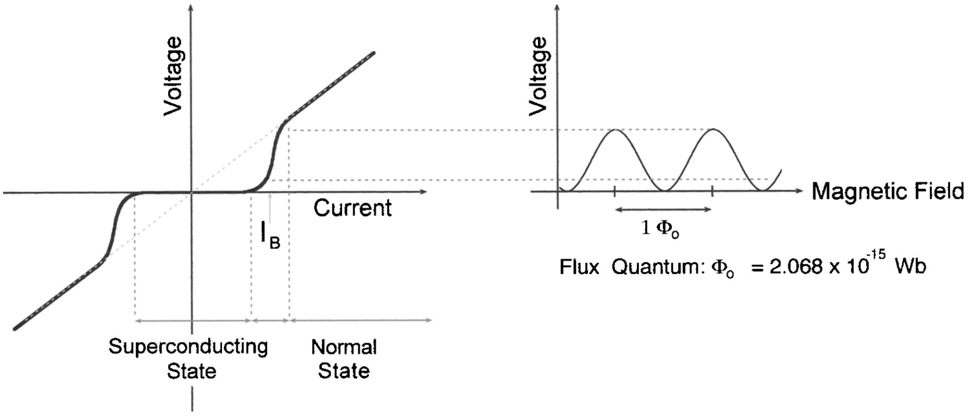

Figure 3.6: (a) Bias point (I_B) for Josephson junction; (b) voltage vs external applied field at constant current [14].

3.3.4 Electrical Transport Measurements

In this section, we discuss the electrical characterization such as Hall effect (R_{xy} - H) and resistance vs temperature (R_{xx} - T) measurements of the grown thin films. A cryostat is an instrument which can vary the temperature (T) and the applied magnetic field (H) around the sample of interest. In particular, we use for all electrical measurements, Physical Property Measurement System (PPMS, DynaCool) from **Quantum Design**. A very brief description of PPMS is as follows : PPMS is a fully automated cryostat system with temperature range 1.9K-400K and different magnetic field range (up to $\pm$14T). The basic unit of PPMS consists of a cryostat and a superconducting magnet, as shown in Fig.3.7a. The cryostat has two different stages. The cryostat typically has two stages: a primary stage and a sample stage. The primary stage is cooled using liquid helium and serves as a heat sink to remove heat from the sample stage. The sample stage is located at the bottom of the cryostat and is cooled by the primary stage, typically to temperatures as low as 0.05 K.

The superconducting magnet is located outside the cryostat and produces a magnetic field that can be varied up to 9/14T. The magnet is typically cooled using liquid helium to achieve its superconducting state and to minimize its resistance, which allows it to produce a strong and stable magnetic field.

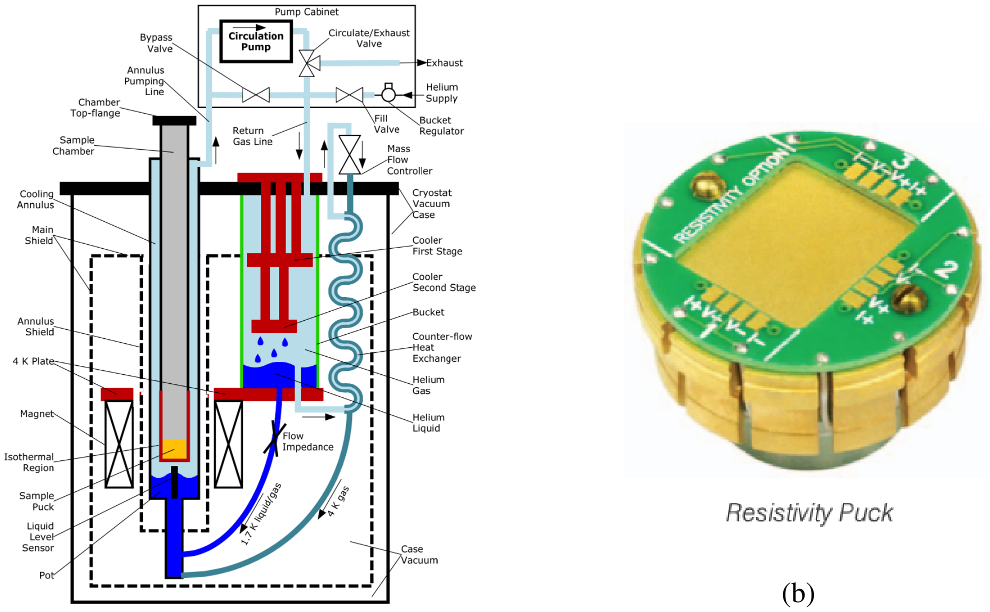

(a)

(b)

Figure 3.7: (a) The DynaCool Cryostat showing the components of the Cryostat Control System, Chamber Temperature Control System, and Magnetic Field Control System. [15]. (b) Puck for placing the sample for R-T and R-H measurement.

3.3.4.1 Resistivity measurement— Linear four probe method

After describing the cryostat operation, we wish to measure the resistivity of the grown thin films. Four probe method is one of the common ways to estimate the thin film resistivity, it is also known as Kelvin probe method named after Lord Kelvin invented a Kelvin bridge to measure a very small resistance. In four point probe method, four equally spaced probes are placed to make the electrical contact with the material of interest, the inner two probes measure the voltage, and the outer two probes provide the current (Fig. 3.8). If the probe spacing is S and the voltage drop between the inner probes is ΔV due to the current (I) flow in the outer probe, then the sheet resistance (R_S) of the infinite sheet of thin films can be written as;

$$R_S = \frac{\pi}{\ln(2)} \frac{\Delta V}{I} \tag{3.3}$$

The factor $\frac{\pi}{\ln(2)}$ is geometrical factor and this factor depends on the sample dimension, shape, and thickness of the sample. The primary advantage of using four probe method is that because the current and voltage are applied and measured at different probes, respectively. Therefore, the effect of contact resistance on the actual value of the resistance can be eliminated. If the film thickness is t, then the resistivity (ρ) can be calculated using the following formula

$$R_S = \frac{\rho}{t} \tag{3.4}$$

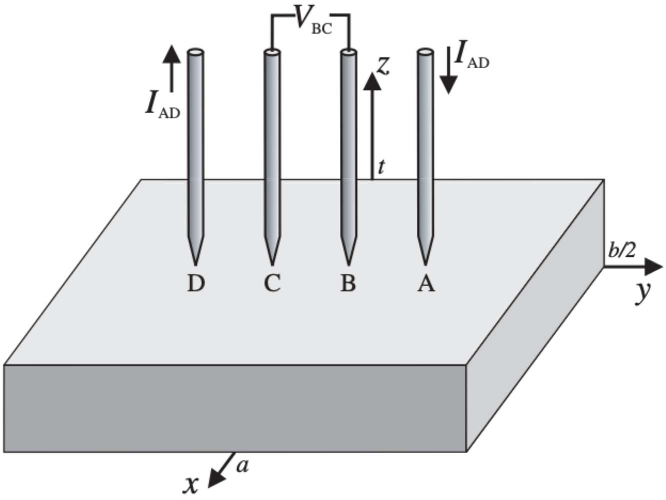

Figure 3.8: Schematic of four point probe method [16]

3.3.4.2 Resistivity measurement—Van der Pauw method

Van der Pauw method is also a four probe technique to measure the resistivity and the Hall coefficient of a sample of an arbitrary shape. In this method, instead of linear contacts, electrodes are placed on the perimeter of the sample, and thus it measures the average resistivity of the sample. Van der Pauw method can be useful when the sample properties are anisotropic. The value of the resistivity can be estimated from the conventions shown in Fig. 3.9. The voltages V1, V3, V5 and V7 are measured with one polarity of the current at the respective contacts and V2,V4,V6 and V8 are measured at the same contacts but with opposite polarity of the current. Once all the voltage are measured, two values of resistivity ρ_A and ρ_B are derived from the following formula:

$$\rho_A = \frac{\pi}{\ln(2)} f_A t_s \frac{V1 - V2 + V3 - V4}{4I},$$
$$\rho_B = \frac{\pi}{\ln(2)} f_B t_s \frac{V5 - V6 + V7 - V8}{4I} \tag{3.5}$$

Where ρ_A and ρ_B are the volume resistivity and f_A and f_B are geometrical parameters which depends on the symmetry of the sample. for perfectly symmetric sample $f_A = f_B = 1$. I is the current flows in each side of the sample. V1-V8 voltage measured according to the Fig. 3.9.

The average resistivity of the sample can be calculated from the average value of ρ_A and ρ_B.

$$\rho = \frac{\rho_A + \rho_B}{2} \tag{3.6}$$

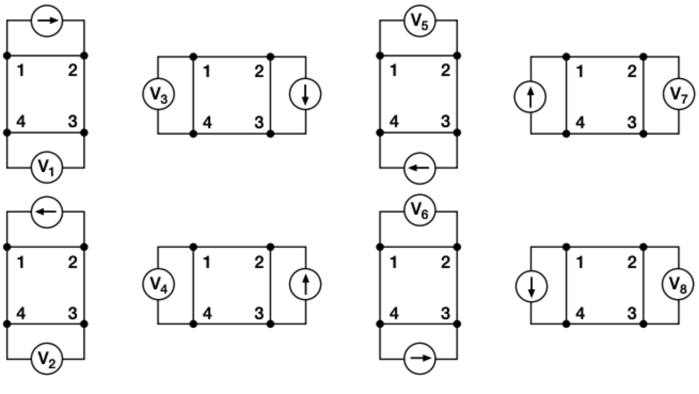

Figure 3.9: Convention in Van der Pauw resistivity measurement.

3.3.5 Device Fabrication-Optical lithography

In order to measure the current and voltage in the thin film, electrodes are fabricated on the film using optical lithography. Optical lithography, also known as photolithography, is a technique that utilizes light to transfer a desired pattern onto a thin film. This process is commonly used in semiconductor IC manufacturing. The type of lithography used can vary based on the wavelength of light employed, such as UV (Ultraviolet) lithography, EUV lithography (Extreme ultraviolet), or X-ray lithography. The choice of light wavelength plays a role in determining the maximum resolution or minimum feature size achievable in the process.

Figure 3.10 illustrates the typical steps involved in optical lithography. The process begins with surface cleaning of the thin film to remove any organic or inorganic contaminants. This is typically done by sonication in solutions such as IPA (Isopropyl alcohol) and Acetone. Next, a photoresist is coated onto the thin film using a spin-coater to ensure an even thickness. A soft bake is then performed to remove any residual solvent from the photoresist. Subsequently, the photoresist is exposed to light through a mask, causing a chemical change in the resist. After exposure, the sample is immersed in a developer solution, which selectively dissolves either the exposed or unexposed parts of the photoresist depending on the nature of the resist. In positive resist, exposure makes the resist more soluble in the developer solution, while in negative resist, the exposed resist becomes chemically hardened, allowing the unexposed resist to be dissolved away. This process results in the desired pattern being transferred onto the film, as shown in Figure 3.10. For OFMR and STFMR measurements, a typical device setup is shown in Figure 3.11.

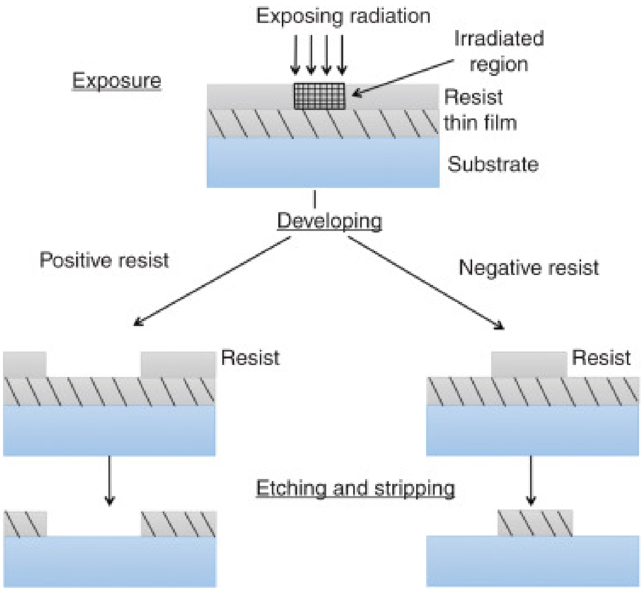

Figure 3.10: (a) Illustration of Photolithography process [17]

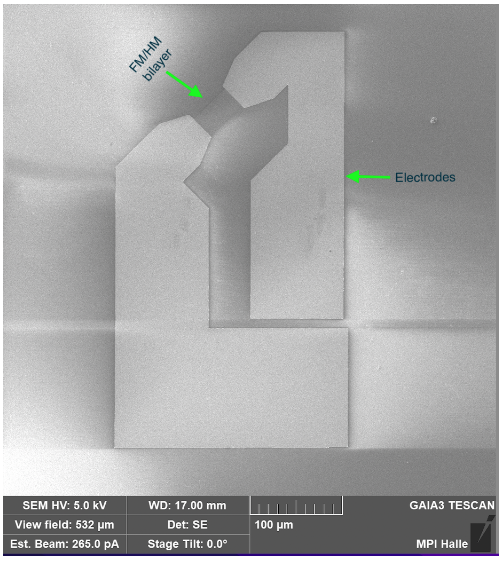

Figure 3.11: SEM image of the STFMR/OFMR device. The optical lithography process was used to fabricate such devices.

3.4 Magneto optical Kerr effect (MOKE)

When a linearly polarized light (s or p polarized) interacts with a magnetic surface, it experiences a rotation of its polarization plane and it becomes elliptically polarized light. This effect was first observed by Michael Faraday in transmitted light in 1845, and the same effect was observed by the Scottish physicist John Kerr in 1876, but in the reflection mode, This effect is known as Magneto Optical Kerr (or Faraday) effect (MOKE).

There are three types of MOKE geometry: Polar, Longitudinal and Transverse, depending on the direction of the magnetization ($\vec{m}$) as shown in the Fig. 3.12. The Kerr angle (Θ_K) of the polarization plane of light is generally expressed as a complex number [66].

$$\Theta_K = \phi + i\epsilon \tag{3.7}$$

The angle ϕ generally represents the Kerr rotation and ϵ denotes the Kerr ellipticity. The physical origin of Kerr effect can be understood using microscopically approach and it's as follows : A linearly polarized light can be decomposed to right and left handed circular polarized (LCP and RCP)states. These LCP and RCP components interact with sample surface differently and results in complex Kerr rotation.

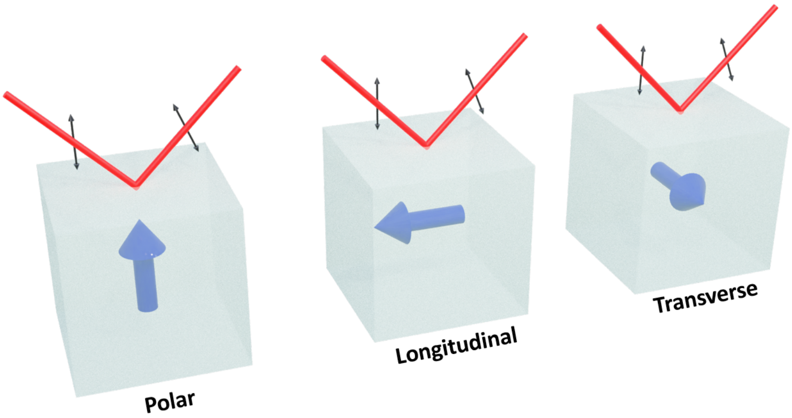

Figure 3.12: Schematic of magneto optical Kerr effect, There are three types of MOKE geometry (Polar, Longitudinal and Transverse) depending on the direction of incident light polarization and magnetization $\vec{m}$ in the sample.

In general, if the optical properties of the sample is same in every direction (optically isotropic), then the permittivity tensor can be written as follows

$$\begin{pmatrix} \epsilon_{xx} & 0 & 0 \\ 0 & \epsilon_{yy} & 0 \\ 0 & 0 & \epsilon_{zz} \end{pmatrix} \tag{3.8}$$

$\epsilon_{xx} = \epsilon_{yy} = \epsilon_{zz} = \epsilon_r\epsilon_0$, where ϵ_r is the relative permittivity of the material, and ϵ_0 corresponds to the vacuum permittivity. The refractive index of a material is defined as $n^2 = \epsilon_r$. However, due to the net magnetization ($\vec{m}$) in the sample (for example, in the z-direction, m_z), it becomes optically anisotropic, and therefore the permittivity tensor takes the form of a skew-symmetric matrix.

$$\begin{pmatrix} \epsilon_r\epsilon_0 & \epsilon_r\epsilon_0 m_z & 0 \\ -\epsilon_r\epsilon_0 m_z & \epsilon_r\epsilon_0 & 0 \\ 0 & 0 & \epsilon_r\epsilon_0 \end{pmatrix} \tag{3.9}$$

The non-zero off-diagonal components ($\epsilon_r\epsilon_0 m_z$) of the permittivity tensor are magnetization (m_z) dependent and therefore affect the velocity and refractive index of light differently. This means that LCP and RCP light experiences different velocities and refractive indexes inside the material, which results in the phase difference between them and thus rotation of polarization plane. The origin of Kerr ellipticity depends on the magnetic circular dichroism i.e., the absorption of LCP and RCP light different absorption. The MOKE is a powerful tool to study the magnetization in ferromagnetic or even in some antiferromagnetic materials [67].

The magnitude of Kerr rotation can be quantified in a magneto-optical Kerr effect (MOKE) setup [68]. When a linearly polarized beam is incident upon a ferromagnetic material, the reflected beam contains both p-component (E_p) and s-component (E_s), with the ratio E_s/E_p defining the Kerr rotation. However, a drawback of this measurement is that the intensity (I) detected by the photodetector is proportional to the square of the s-component ($|E_s|^2$), which can lead to inaccuracies.

To overcome this issue, the analyzer can be positioned at a small angle (δ) relative to the p-axis. By doing so, the intensity measured by the photodetector is no longer solely dependent on $|E_s|^2$, but is influenced by the combined effect of E_s and E_p, resulting in a more accurate measurement of the Kerr rotation.

$$I = |E_p \sin\delta + E_s \cos\delta|^2 \approx |E_p \delta + E_s \cos\delta|^2 \tag{3.10}$$

Now Kerr rotation according to the equation 3.7 $E_s/E_p = \phi + i\epsilon$. Therefore

$$I = |E_p|^2 |\delta + \phi + i\epsilon|^2 \approx |E_p|^2(\delta^2 + 2\delta\phi) = I_0(1 + \frac{2\phi}{\delta}) \tag{3.11}$$

The intensity at zero Kerr rotation can be represented as $I_0 = |E_p|^2\delta^2$. Consequently, when the analyzer is positioned at a small angle (δ) relative to its orthogonal axis, the Kerr rotation measured by the photodetector is directly proportional to the magnetization (m).

The ability to measure the magnetization in the sample can also provide the insight into SHE based phenomena.

3.5 Optically Detected Ferromagnetic Resonance (OFMR)

After studying the basic electrical properties of the films, we wish to characterize the spin Hall efficiency or angle (θ_{SH}) in grown films. For this purpose, we build a special optical technique known as Optically Detected Ferromagnetic Resonance(OFMR) to study the dynamics of the magnetic moments and the effect of the spin current on it. We divide the description of the setup in the following sections.

3.5.1 LASER Source

In OFMR, we use Ti: Al_2O_3 (Vitara oscillator, **Coherent Inc.**) laser system. Where Ti: Al_2O_3 refers to the lasing medium, where sapphire crystal (Al_2O_3) is doped with Ti^{+3} ions. There are some specials properties of the gain medium which makes Ti:Al_2O_3 its more popular among all other solid state lasers.

- Monocrystalline Al_2O_3 has a large thermal conductivity, therefore it is suitable for high laser power and intensities at high temperature.
- The Ti^{+3} ions provides very large gain bandwidth greater than rare-earth doped gain medium, therefore allowing the shorter laser pulses.
- The maximum gain and efficiency obtained around 800 nm, although using different mirror sets wavelength range can be tuned between 650-1100 nm.
- Ti: Al_2O_3 gain medium is pumped by an external laser source, usually a diode laser (pump wavelength lies in green spectral region.)

In our case, Ti: Al_2O_3 laser has a central wavelength of 800 nm and has a repetition rate of 80MHz (12.5 ns time difference between two sucessive laser pulses) and pulse width of about 35fs. The sample of interest (shown in Fig. 3.11) is excited by a microwave/RF signal which is synchronized with the laser pulses. We describe the synchronization process in the next section.

3.5.2 LASER Alignment

As shown in the Fig. 3.13 laser emanates from the source on table 1 and aligned to table 2. The laser is aligned in straight line with the help of two mirrors. Each mirror is mounted is on kinematic mounts, which provides the two degrees of freedom (Pitch(θ), Yaw(ϕ)). By changing these two degree of freedom (θ_1, ϕ_1) and (θ_2, ϕ_2) for each mirror, with few iterations the desired position (x_0, y_0) of the beam can be achieved.

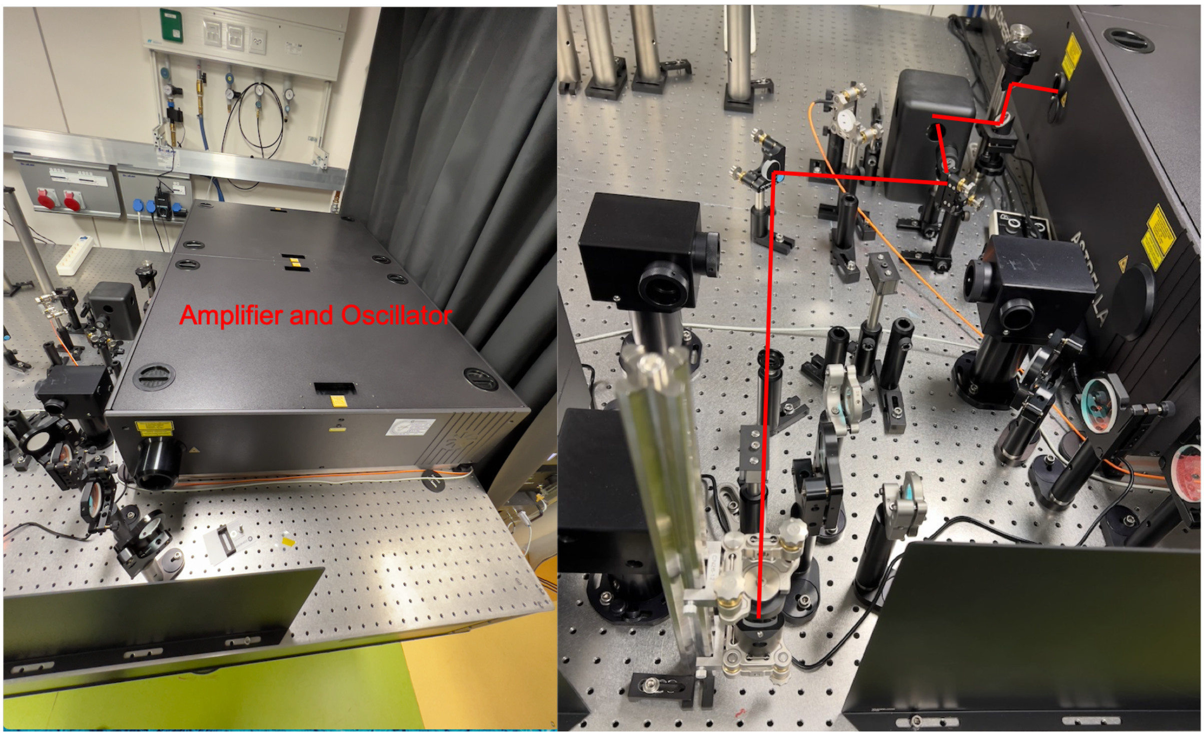

Figure 3.13: Laser emanate from the source (labelled as Amplifier and Oscillator sitting on table 1)

3.5.2.1 Delay Stage Alignment

We use a linear delay stage (**DL325** from Newport) to provide the relative delay between microwave and laser pulses. We use hollow retroreflector (shown in Fig. 3.14), which make sure incoming and outgoing beams parallel to each other. We send the laser beam to very far distance (longer than the travelled path of the beam in the setup) and move the stage back and forth (from starting point to the end point of the delay stage) and observe the beam position. We compensate the beam shift position with the help of two mirrors, after few iterations of this procedure, laser beam is aligned accurately (shown in Fig. 3.15).

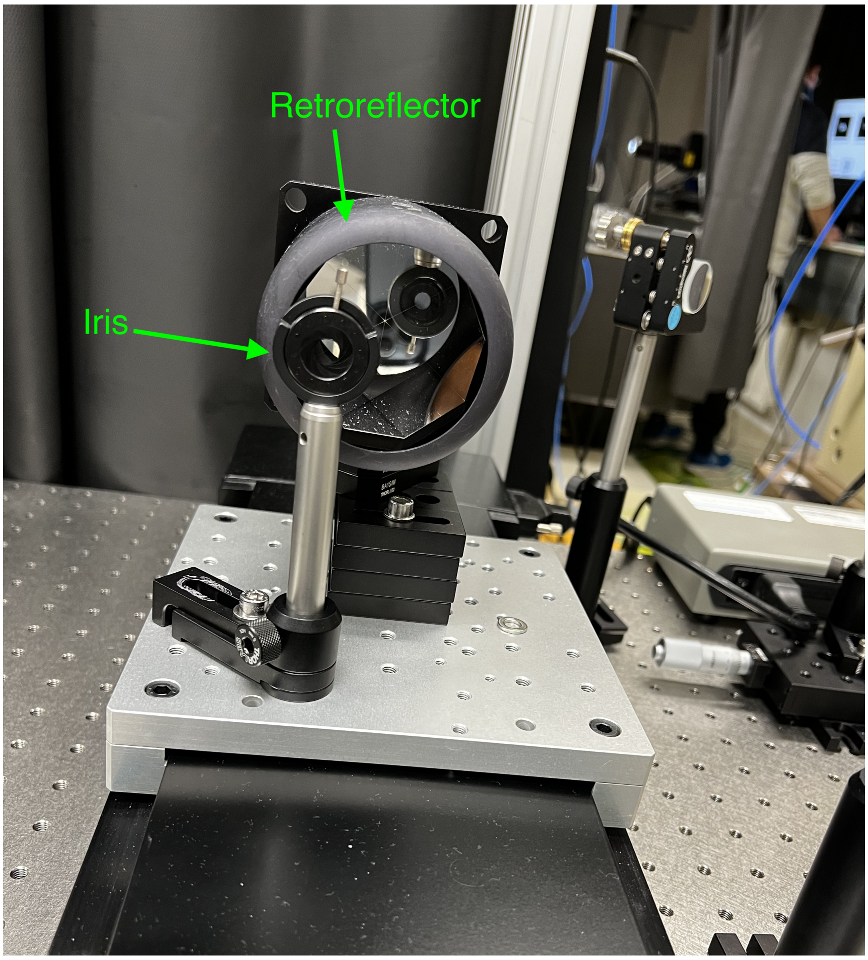

Figure 3.14: Broadband hollow retroreflector

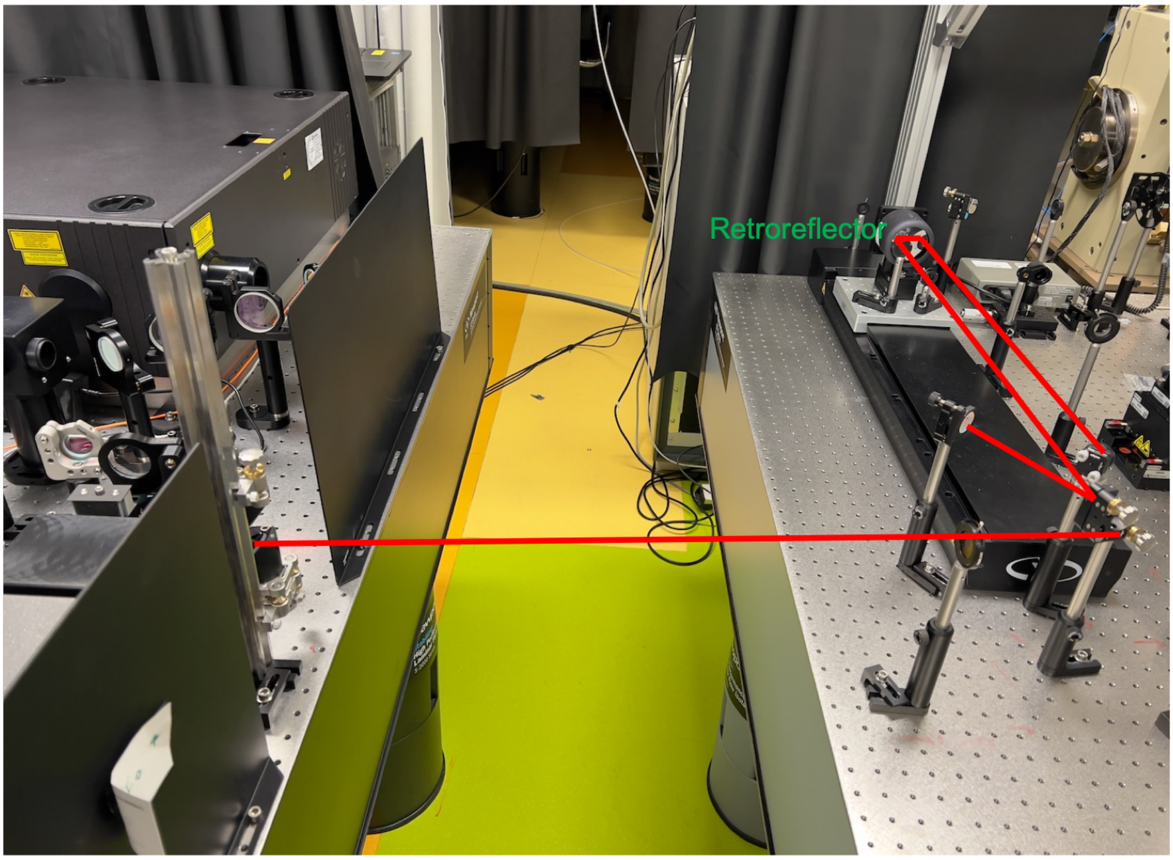

Figure 3.15: Alignment of the delay stage

After alignment of the delay stage, the laser beam is collimated by two lens (**lens 1** and **lens 2** as shown in Fig. 3.16). Then, it becomes **s**-polarized (parallel to the table) with the help of polarizer, and it goes through the beamspliter (labelled as B.S in Fig. 3.16) and impinges on the sample normally and measure the magnetization in the sample via MOKE. The reflected light goes through the analyser and hits the photodetector. The polarization axis of the analyser is deliberately positioned at an angle of $90^\circ \pm \delta$ relative to the polarizer. Here, δ represents a minute angular deviation from the orthogonal axis of the analyser, as previously elucidated. The voltage due to Kerr rotation is measured by the photodetector, the alignment, and focus of the beam on to the detector is done by the XYZ translational stage. The voltage is multiplied by the gain (usually between × 1000-3000) of the detector and feed into the lock-in amplifier (SR-830, **Stanford Instrument**). The sample is subjected to an amplitude modulated microwave signal, which is delivered through a waveguide. The modulation is achieved by utilizing a lock-in amplifier, generating a TTL (Transistor-

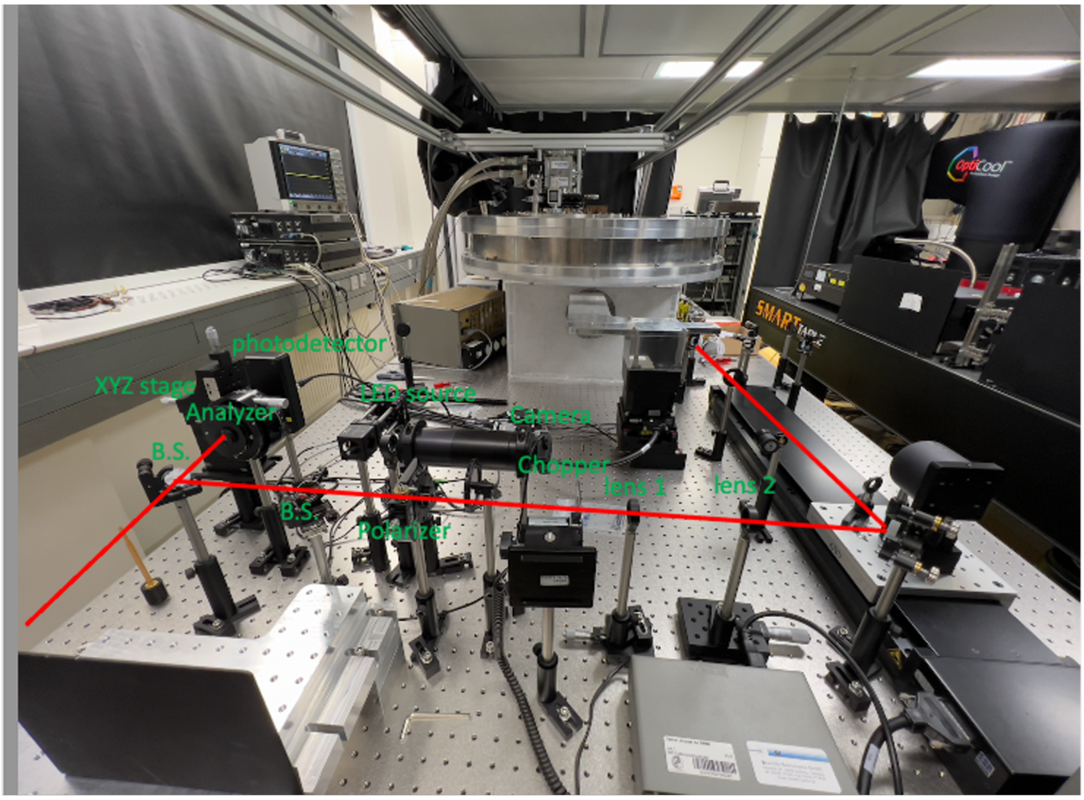

Figure 3.16: (The Laser beam is collimated by the two lenses (**lens 1** and **lens 2**)). The beam becomes **s**-polarized after passing through the polarizer.

Transistor Logic) output that serves as the modulation source. The modulation frequency ranges from 1 kHz to 5 kHz. By demodulating the voltage at the same frequency, the lock-in amplifier enhances the signal-to-noise ratio and allows for the accurate measurement and characterization of the desired response from the photodetector. We use an 20X objective lens with a numerical aperture (NA) of 0.40 (Olympus LMPlanFl). Which provides the lateral resoultion of the setup $\approx 0.5-1\,\mu\text{m}$ ($R = \frac{\lambda}{2NA}$)[69].

3.5.3 Synchronization of the RF signal and LASER

As mentioned above, an RF current passes through the device and excite the magnetization. These excitations of the magnetic moment are probed by laser pulses. In order to probe the excitations right on the time, the laser needs to time synchronized (or phase locked) with an RF signal. The synchronization procedure is as follows : A RF signal is divided by an appropriate ratio (n $\times$ 80MHz, where n is the divide ratio) using a frequency divider. Then the divided signal goes into the synchrolock, which changes the cavity length of the laser in

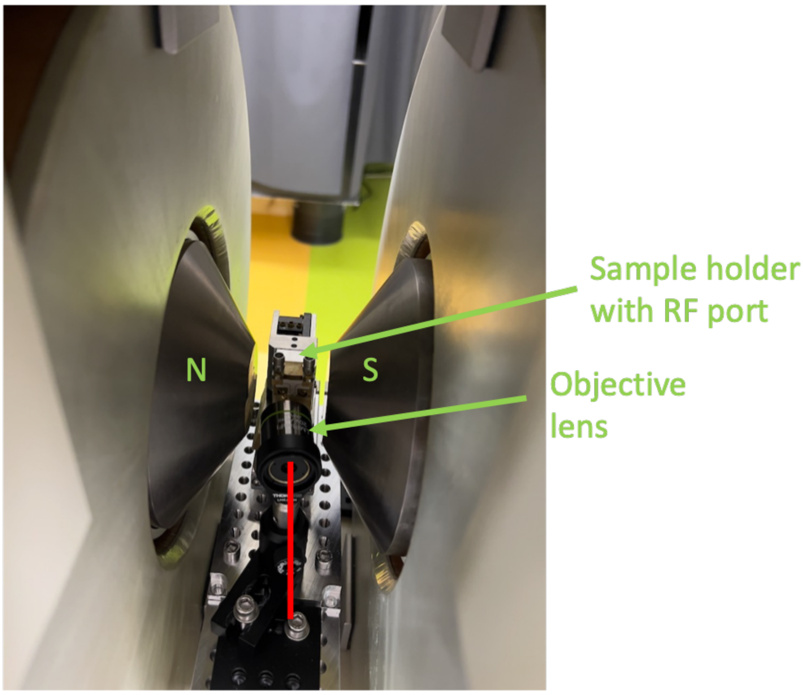

Figure 3.17: A laser beam is striking the sample perpendicularly and measure the magnetization via MOKE. The reflected signal contains the information about the magnetization in the sample and measured by the photodetector. The device is excited by passing the RF current through the RF port into the device via wirebonding.

a way that it locks the phase of the RF signal to one of those longitudinal modes of the laser in frequency domain (shown in Fig. 3.18). Here, the RF signal serves as a master clock while the laser behaves as a slave clock. This synchronization is monitored by a fast photodetector, which provides the feedback signal to synchrolock. The synchrolock, phase locked the laser to RF signal up to the 9^{th} harmonics and this synchronization can be maintained up to few months without any interruption.

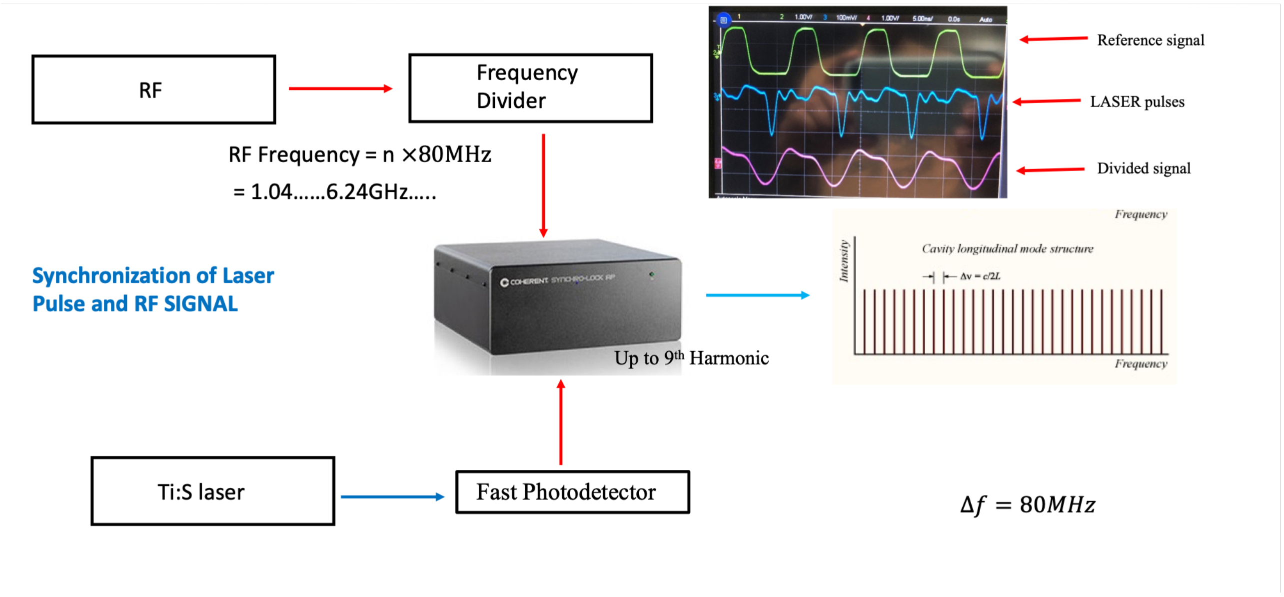

Figure 3.18: Synchrolock Procedure in OFMR.

3.5.4 Voltage Detection in OFMR

In OFMR an in-plane magnetic field $\mathbf{H}_{\text{ext}}$ is applied to the sample. The RF current passes through the sample at 45°with respect to $\mathbf{H}_{\text{ext}}$. This excites the magnetization, which give rise to the out of plane component of magnetization (m_z). The dynamics of the magnetic moment in the presence of spin current can be explained by the Landau Lifshitz-Gilbert equation (LLG) equation (under macro spin approximation).

$$\frac{d\vec{m}}{dt} = (-\gamma \vec{m} \times \vec{H}_{\text{eff}}) + \frac{\alpha}{M_s}\left(\vec{m} \times \frac{d\vec{m}}{dt}\right) + \tau_{DL}(\vec{m} \times (\vec{m} \times \vec{\sigma})) + \tau_{FL+Oe}(\vec{m} \times \vec{\sigma}) \qquad (3.12)$$

The terms $(\vec{m} \times (\vec{m} \times \vec{\sigma})$ and $(\vec{m} \times \vec{\sigma})$ represents damping-antidamping like (τ_{DL}) and field/orested field like torques (τ_{FL+Oe}) acted along in-plane and out of plane component of the magnetization ($\vec{m}$) respectively. Where $\vec{H}_{\text{eff}}$ is the total field acted on the magnetization, i.e., anisotropic field ($\vec{H}_{\text{an}}$), external field ($\vec{H}_{\text{ext}}$), demagnetization field ($\vec{H}_d$) and RF field ($\vec{H}_{\text{RF}}$) etc. Therefore, $\vec{H}_{\text{eff}} = \vec{H}_{\text{an}} + \vec{H}_{\text{ext}} + \vec{H}_d + \vec{H}_{\text{RF}}$, σ is the spin polarization and α is the Gilbert damping of the ferromagnetic material. if we consider the linear excitation ($H_{\text{RF}} = h_o \sin(\omega_1 t)$), then the magnetization response at certain field would be

$$m_z = A\sin(\omega_2 t + \Theta) \tag{3.13}$$

Where A is the amplitude and Θ is the relative phase of the magnetization with respect to the RF field and ω_1, ω_2 are the angular frequencies of the RF excitation and magnetic oscillation at a certain field. At resonance,$\omega_1 = \omega_2 = \omega$. For simplicity, we consider the resonance condition. In our measurement, we choose two types of measurement protocols to measure the magnetization response, either we sweep the delay between RF and laser at certain field, or we sweep the external magnetic field at certain delay. The above equation 3.13 describe the amplitude of the magnetization at certain field, however if we sweep the field the response would be

$$\delta m_z = h_0 \left(\chi'_{xy}\cos\phi + \chi''_{xy}\sin\phi \right) \tag{3.14}$$

Where χ'_{xy} and χ''_{xy} are the real and imaginary part of the susceptibility tensor [70]. ϕ is the relative phase between RF excitation and laser. χ'_{xy} and χ''_{xy} are given by the equation

$$\begin{aligned} \chi'_{xy} &= \frac{M_s \frac{\omega}{\gamma}}{2(2H_{ext} + M_s)} \frac{\delta H}{(H_{ext} - H_{res})^2 + \delta H^2} \\ \chi''_{xy} &= \frac{M_s \frac{\omega}{\gamma}}{2(2H_{ext} + M_s)} \frac{(H_{ext} - H_{res})^2}{(H_{ext} - H_{res})^2 + \delta H^2} \end{aligned} \tag{3.15}$$

Where ω is the angular frequency of RF excitation, γ is the gyromagnetic ratio, M_s is the saturation magnetization, δH is the full width half maximum (FWHM) of the spectra and H_{res} is the resonance field. In the experimental set-up, the out of plane component of the magnetization (δm_z) is measured via MOKE. Upon reflection from the sample, the polarization of the light is rotated by an angle $\delta\theta$, which is proportional to the δm_z .The relation between $\delta\theta$ and δm_z is given by

$$\delta\theta = \frac{\Phi_k \delta m_z}{M_s} \tag{3.16}$$

where Φ_k is the Kerr rotation angle. Then the voltage at the photodetector yields.

$$V_{det} = GP_0(t)\delta\theta \tag{3.17}$$

Where G is the gain factor, $P_0(t)$ is the incident power on the photodetector therefore voltage expression in OFMR yields

$$V_{det} = Ah_0P_0(t)\frac{\Phi_k\delta m_z}{M_s} \tag{3.18}$$

$$V_{det} = Ah_0P_0(t)\frac{\Phi_k}{M_s}\left[\chi'_{xy}\cos\phi + \chi''_{xy}\sin\phi\right] \tag{3.19}$$

Therefore, the optical response of the FMR at certain delay can be written is a combination of symmetric (V_{sym}) and antisymmetric (V_{as}) part of the Lorentzian function. i.e.

$$V_{det} = \Gamma\left[V_{sym}\cos\phi + V_{as}\sin\phi\right] \tag{3.20}$$

Where

$$\Gamma = Ah_0P_0(t)\frac{\Phi_k}{2\delta H}\frac{\frac{\omega}{\gamma}}{2(2H+M_s)}\omega,$$

$$\begin{aligned} V_{sym}(H) &= \frac{\delta H^2}{(H-H_0)^2+\delta H^2}, \\ V_{as}(H) &= \frac{\delta H(H-H_0)}{(H-H_0)^2+\delta H^2} \end{aligned} \tag{3.21}$$

3.6 Spin Torque Ferromagnetic Resonance (ST-FMR)

After characterizing the spin Hall efficiency by OFMR, we wish to measure the same but by an electrical technique known as spin torque ferromagnetic resonance (STFMR). ST-FMR is a pretty common technique to determine the spin Hall efficiency θ_{SH}. In a typical ST-FMR setup, an external magnetic field (H_{ext}) is applied in plane to the sample. An RF current (I_{RF}) passes through the FM/HM bilayer at 45° with respect to H_{ext}. Due to the oscillatory nature of the current, the magnetic moment in FM layer starts to precess around H_{ext}. This leads to the oscillation in anisotropic magneto resistance (AMR) in FM layer, therefore the resistance of FM becomes time dependent. The time dependent resistance (R(t)) and RF current (I_{RF}) produces a rectified voltage across FM/HM bilayer. This voltage is also called mixing voltage (V_{mix}) as it comes from the mixing of I_{RF} and an AMR (ΔR). As the external field (H_{ext}) is swept, the oscillation of magnetic moment becomes larger at resonance and decreases away from the resonance. This mix or rectified voltage (V_{mix}) can be measured by nano-voltmeter or lock-in amplifier.

An additional DC current is applied to measure the SHE. The DC current creates DC spin current, which in turn absorbed by the FM leads to a change in damping (α). The effective damping (α) of FM under spin current can increase or decrease depending on the polarity of the current and the direction of the external magnetic field. The Illustration of the technique is shown below in Fig. 3.19b.

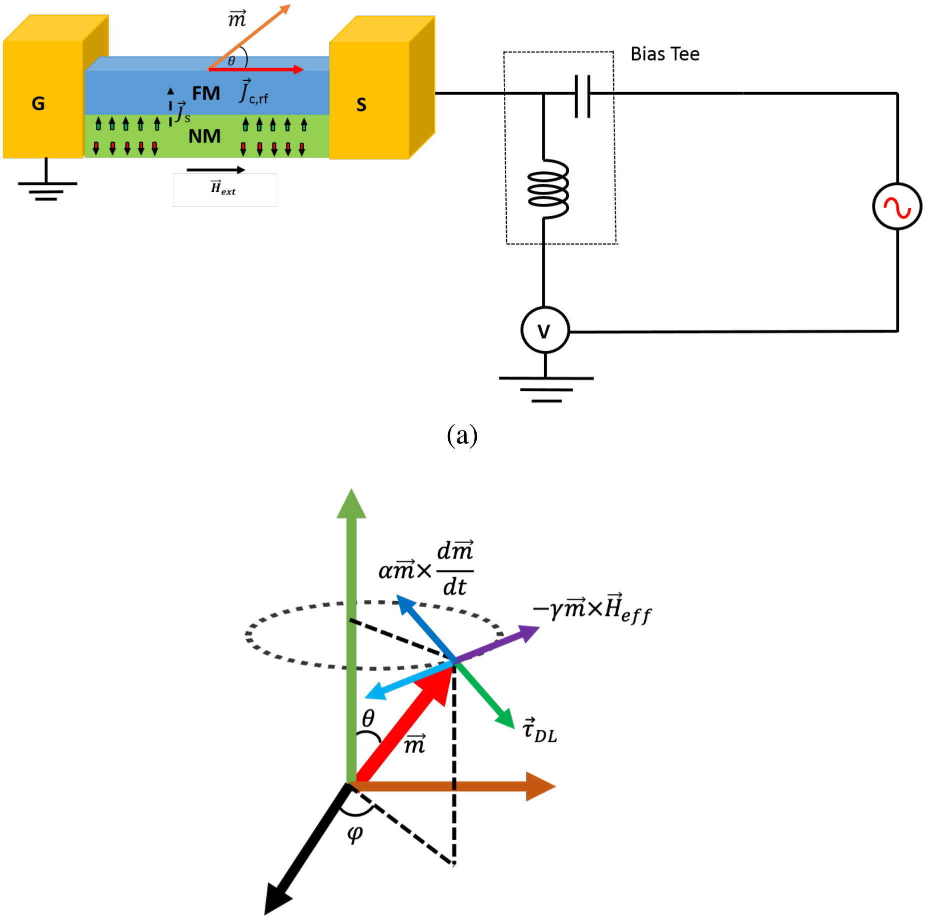

(a)

(b)

Figure 3.19: (a) Illustration of the STFMR setup. (b) Different torques act on the magnetic moment ($\vec{m}$).

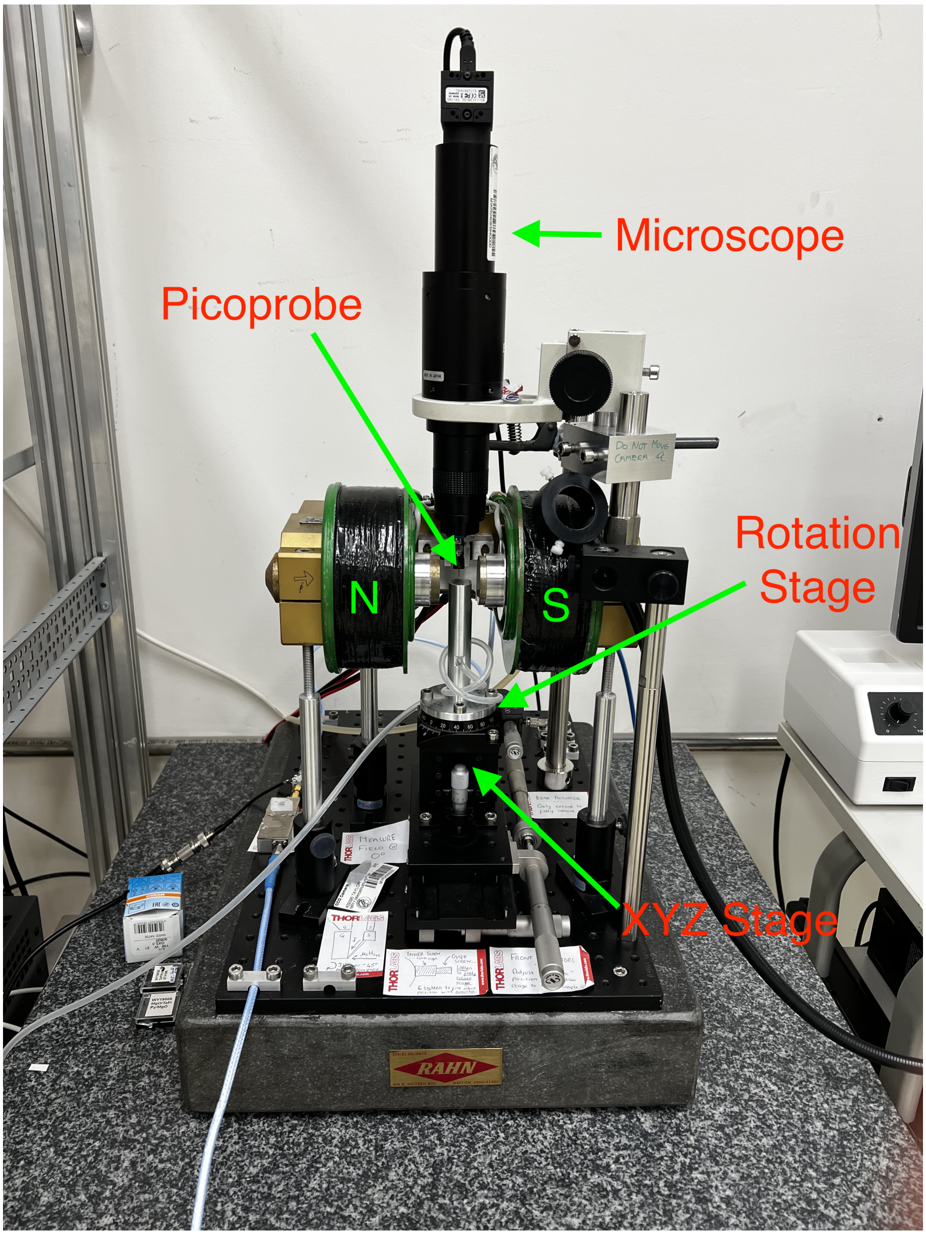

Figure 3.20: STFMR set up labeled with different parts

Fig. 3.20 shows a home built ST-FMR setup. The sample sits on a rotatory stage, which is further mounted on a XYZ translational stage. The typical ST-FMR device is shown in the Fig. 3.11. The RF current passes through the device at 45°with respect to external field (H_{ext}). The pico-probe is used to send the RF current and to measure the voltage (V_{mix}) as well. A bias tee is used to send the additional DC current. A vertical microscope is used to align the pico probe on to the sample electrodes.

3.6.1 Voltage rectification in ST-FMR

As we stated in the last section, the voltage in ST-FMR setup comes from the spin rectification of AMR in FM layer. Here we're going to derive the general expression of the ST-FMR voltage. The voltage due to the rectification of the AMR can be expressed in the following manner : The current passing through the FM/HM bilayer can be written as $I = I_0 \cos(\omega t)$ where I_0 is the amplitude and ω is the angular frequency of the RF current I_{rf}. Due to the oscillation of AMR, the device resistance becomes oscillatory

$$R(t) = R_0 + \Delta R \cos^2 \theta(t) \tag{3.22}$$

where R_0 is the resistance when current I_{rf} is perpendicular to the magnetization ($\vec{m}$) in FM layer, ΔR is the AMR, θ is the angle between I_{rf} and the magnetization $\vec{m}$, which in turns depends on the time (t).

$$\theta(t) = \theta_H + \theta_c \cos(\omega t + \delta) \tag{3.23}$$

Where θ_H is the constant angle between applied field (H_{ext}) and the current I_{rf}, θ_c is the cone angle of precession of $\vec{m}$ in FM layer, The value of θ_c is generally smaller than θ_H, δ_c is the resonance phase between driving torques (damping-antidamping like τ_{DL} and field like torque τ_{FL}) and the magnetization response. By using the Taylor's expansion, we can get

$$\cos(\theta(t)) = \cos(\theta_H + \theta_c \cos(\omega t + \delta)) \tag{3.24}$$

Therefore, time dependent expression of AMR becomes

$$R(t) = R_0 + \Delta R \cos^2(\theta_H + \theta_c \cos(\omega t + \delta)) \tag{3.25}$$

$$R(t) = R_0 + \Delta R \cos^2 \theta_H - 2\cos\theta_H \sin\theta_H . \theta_c . \cos(\omega t + \delta) \tag{3.26}$$

Hence, the voltage expression across FM/HM bilayer would become

$$V(t) = I(t)R(t) \tag{3.27}$$

$$V(t) = (IR_0 + I\Delta R\cos^2\theta_H\cos(\omega t)) - I\Delta R\sin(2\theta_H).\theta_c\cos(2\omega t + \delta)/2 \tag{3.28}$$

Therefore, the total voltage consists of three terms at frequencies ω 2ω and a DC term (time independent term). And this DC term is nothing but the rectified ST-FMR signal. Hence,

$$V_{mix} = -I\Delta R\sin(2\theta_H).\theta_c(\cos\delta)/2 \tag{3.29}$$

The ST-FMR signal is determined by the combination of the amplitude of I_{rf}, the AMR in the device ΔR, the angle of H_{ext} with respect to I_{rf}, the cone angle of precession θ_c and the resonance phase δ. The value of δ goes to 0 - π around the resonance field (H_{res}) with a linewidth of ΔH. The typical ST-FMR spectra can be fitted by linear combination of symmetric and asymmetric part of Lorentzian function.

$$V_{mix} = \frac{V_S\Delta H^2}{((H_{ext} - H_{res})^2 + \Delta H^2)} + \frac{V_A(H_{ext} - H_{res})}{((H_{ext} - H_{res})^2 + \Delta H^2)} \tag{3.30}$$

where V_S and V_A are amplitudes of symmetric and asymmetric component of the Lorentzian function. The value of the symmetric component goes to maximum at H_{res}, whereas for the asymmetric component, the value goes to zero at H_{res}. Both components have the same linewidth value ΔH.

3.6.2 Methods for determining the Spin Hall angle (θ_{SH}) in STFMR

There are a number of ways to determine the spin to charge efficiency in STFMR technique. The following methods

3.6.2.1 V_S/V_A method

As described above, the STFMR voltage (V_{mix}) consist of symmetric (V_S) and asymmetric (V_A) component of Lorentzian function. The V_S component is proportional to the absorbed spin currents (J_S) in FM, and it represents the damping-antidamping like torque (τ_{DL}). The V_A component is correlated to the induced Oersted field torque (τ_{Oe}) generated in HM layer due to the flow of the current [71] [22][72].

$$V_S \propto \frac{\hbar J_S}{2e\mu_0 M_s t} \tag{3.31}$$

$$V_A \propto \frac{H_{RF}}{[1+4\pi M_{eff}/H_{ext}]^{1/2}} \tag{3.32}$$

The field induced Oersted torque can be calculated from Ampere's law ($H_{RF} = J_C d/2$). Therefore, the spin to charge conversion efficiency or spin Hall angle (θ_{SH}) can be estimated by

$$\theta_{SH} = \frac{J_S}{J_C} = \frac{V_S}{V_A}\frac{e\mu_0 M_S td}{\hbar}\left[1+\frac{4\pi M_{eff}}{H_{ext}}\right]^{1/2} \tag{3.33}$$

This method is known as lineshape analysis, and it works under the assumption that there is no field like torque (τ_{FL}) generated at the interface of FM/HM layer. The contribution to the asymmetric voltage (V_A) only comes from the Oersted field H_{RF}. If the interface of FM/HM produces significant Rashba like SOT, Then this method could provide the wrong the estimation of θ_{SH} [73].

3.6.2.2 V_S only method

Since, V_S component of STFMR signal comes from damping like torque(τ_{DL}, acts in plane direction), and the V_A component comes from both field like torque, (τ_{FL}) and Oersted torque (τ_{Oe}, acts out of plane direction), These two components can be separated by the following equations [73][74][75];

$$V_S = -\frac{I_{RF}\gamma\cos\theta_{SH}}{4}\frac{dR}{d\theta_H}\tau_{DL}\frac{1}{\Delta}F_S(H_{ext}) \tag{3.34}$$

$$V_A = -\frac{I_{RF}\gamma\cos\theta_{SH}}{4}\frac{dR}{d\theta_H}(\tau_{FL}+\tau_{Oe})\frac{[1+\mu_0 M_{eff}/H_{ext}]^{1/2}}{\Delta}F_A(H_{ext}) \tag{3.35}$$

Where $\tau_{DL} = \frac{\theta_{SH}J_C\hbar}{2eM_S t}$, is the damping like torque, γ is the gyromagnetic ratio, $\frac{dR}{d\theta_H}$ is the angular dependence of the magneto resistance at angle θ_H, Δ is the linewidth of STFMR signal, $F_S(H_{ext})$ and $F_A(H_{ext})$ are a symmetric and antisymmetric part of the Lorentzian function, I_{RF} is the magnitude of the RF current, M_{eff} is the effective magnetization. Torques τ_{FL} and τ_{Oe} have same symmetry ($\vec{m} \times \vec{\sigma}$) and they act out of plane direction to the magnetization ($\vec{m}$) and can be separate out by different methods [76] [77]. Once the τ_{FL} and τ_{DL} are accurately evaluated, then the corresponding spin Hall efficiencies $\theta_\perp$ and $\theta_{||}$ can be obtained. The V_S only and V_A only method is a general method and works in any material. However, it requires an accurate estimation of parameters such as I_{RF} RF current following through HM layer, which further require calibration of RF signal through HM layer.

3.6.2.3 Modulation of damping(MOD) method

The damping (α) of FM can be influenced in the presence of spin current [78]. In the MOD method, an additional DC current (I_{DC}) passes through FM/HM layer, which increase or decreases the α or the linewidth (ΔH), depending on the polarity of the current and the direction of the external magnetic field (H_{ext}). Under DC bias, the effective linewidth of FM/HM bilayer can be written as

$$\Delta H = \Delta H_0 + \Delta H_{sh} = \frac{2\pi f}{\gamma}\left[\alpha_0 + \frac{\sin\theta_H}{(H_{ext}+2\pi M_{eff})\mu_0 M_S t}\frac{\hbar}{2e}J_{C,HM}\theta_{SH}\right] \tag{3.36}$$

The parameters have the following meanings:

ΔH: The total change in the linewidth broadening caused by spin-orbit torques. ΔH_0: The intrinsic linewidth broadening without current. ΔH_{sh}: The additional linewidth broadening due to spin-orbit torques. f: The frequency of the magnetic resonance. γ: The gyromagnetic ratio. α_0: The damping value without current, representing the intrinsic damping of FM. θ_H: The angle between the direction of the DC current (I_{DC}) and the external magnetic field (H_{ext}). In STFMR/OFMR, this angle is typically set to 45. $J_{C,HM}$: The current passing through the heavy metal (HM) layer, contributing to the spin-orbit torques. M_{eff}: The effective magnetization, which includes both the external magnetic field and the magnetization of the system. μ_0: The vacuum permeability. M_S: The saturation magnetization of FM. t: The thickness of FM. $\hbar$: The reduced Planck's constant. e: The elementary charge. θ_{SH}: The spin Hall angle, representing the efficiency of the spin-to-charge conversion in the heavy metal layer.

The equation 3.36 shows that the change in the magnetic field (ΔH) is determined by the sum of the intrinsic linewidth broadening (ΔH_0) and the additional linewidth broadening due to spin-orbit torques (ΔH_{sh}). The term inside the square brackets represents the contribution of the spin-orbit torques, where the effective damping (α_{eff}) can be modulated by adjusting the angle θ_H. This equation provides a simple and direct method for estimating the effective damping by accurately measuring the slope of linewidth with DC current ($\frac{\Delta H}{\Delta_{I_{DC}}}$). This approach is applicable to various frequency-modulated resonance techniques and is independent of the specific detection scheme. It can be applied in both STFMR and OFMR to compare the techniques in spin Hall effect measurements.

4

Crystallographic Dependence Of Spin Hall Angle in Epitaxial Pt Films

4.1 Introduction

The Spin Hall effect (SHE) encompasses a range of relativistic phenomena that arise when a charge current j_c generates a transverse spin current $j_s\frac{\hbar}{2e}$ through spin-orbit coupling (SOC) [4]. SHE has gained considerable attention due to its applications in manipulating magnetization order parameters in perpendicularly magnetized ferromagnets (FMs) and antiferromagnets for magnetic logic and storage devices [79, 80, 81]. It is also of fundamental interest as it emerges from well-defined band structures and scattering processes closely related to the anomalous Hall effect (AHE). The extrinsic contribution to the spin

Hall conductivity (σ_{xy}^{SH}) depends on the scattering rate (τ) of the electron's spin, while the intrinsic contribution arises from the crystal's band structure, symmetries, and orientation, and is independent of τ [82, 34, 83]. SHE manifests in two forms: intrinsic, which relies on crystal symmetry, and extrinsic, which stems from impurity scattering. The efficiency of SHE is defined by the spin Hall angle (θ_{SH}) and plays a critical role in spintronics-based technologies. However, accurately measuring θ_{SH} and identifying its origin pose significant challenges.

Pt, known for its strong spin-orbit coupling (SOC), is a crucial material for investigating the SHE [84]. It is generally accepted that the SHE in Pt arises from both intrinsic and extrinsic contributions [85]. While studies of the SHE in polycrystalline films have utilized resistivity and temperature dependence to distinguish between these origins [86], investigations of epitaxial films, where the intrinsic SHE should be more pronounced, are less common [83, 87].

Besides the challenges related to material fabrication and engineering, accurately determining the spin Hall angle (θ_{SH}) is crucial for advancing SHE-based technologies. Among various techniques, the spin-torque-driven ferromagnetic resonance (STFMR) method has been extensively employed for this purpose [22]. In a typical STFMR measurement, an RF electrical current passes through a heavy metal/ferromagnet (HM/FM) bilayer, with the HM layer polarizing spins that diffuse into the FM layer. The RF spin torque excites the ferromagnetic resonance (FMR) of the FM layer, which is detected by measuring a DC voltage V_{mix} across the device. The interplay between the oscillatory anisotropic magnetoresistance (AMR) effect and the RF current gives rise to V_{mix}. θ_{SH} can be determined by applying an additional DC current to modulate the FM's damping [73]. However, interpreting the STFMR signal requires careful analysis [88, 89], as it involves considering factors such as RF spin torque, RF Oersted torque, spin pumping, anomalous Hall voltage, and thermoelectric effects like the longitudinal spin Seebeck and Nernst effects [90, 88, 91]. Thus, accurately identifying and quantifying these contributions is crucial for estimating θ_{SH}. Complementary techniques, such as optical methods, which are less prone to electrical artifacts, can provide valuable insights.

This chapter investigates the SHE in epitaxial Pt thin films, with a focus on understanding the dependence of θ_{SH} on crystallographic orientation in epitaxial Al_2O_3(0001)/Pt(111), MgO(110)/Pt(110), and MgO(001)/Pt(001) thin films. In addition to STFMR measurements, the optically detected ferromagnetic resonance (OFMR) technique is employed, enabling the probing of magnetization (m_z) via the magneto-optical Kerr effect (MOKE), instead of measuring V_{mix}.

4.2 Sample Preparation and Characterization

The films under study were grown using a homemade DC magnetron sputtering system in a vacuum chamber with a base pressure of approximately 1×10^{-9} Torr. Pt (111) and Pt (110) layers were sputtered directly onto Al_2O_3 (0001) and MgO (110) substrates, respectively, at a deposition temperature of 550°C. Pt (001) was grown at a temperature of 650°C on a 0.3 nm thick Fe-buffered MgO (001) substrate. The sputtering power and argon (Ar) pressure were maintained at 30 W and 3 mTorr, respectively. The thickness of the Pt layer in all films was approximately 5 nm.

A 5 nm thick ferromagnetic (FM) layer made of Py ($Ni_{81}Fe_{19}$) was subsequently deposited at room temperature on top of the different Pt films using a sputtering power of 30 W and an Ar pressure of 3 mTorr. The films are denoted as Pt (111), Pt (110), and Pt (001), representing the Al_2O_3 (0001)/Pt/Py, MgO (110)/Pt/Py, and MgO (001)/Fe/Pt/Py configurations, respectively, unless specified otherwise.

X-ray diffraction (XRD) plots of Pt (111), Pt (110), and Pt (001) films are shown in Figure 4.1. The distinct peaks observed in each subplot indicate the crystalline nature of these films. Atomic force microscopy (AFM) scans, presented in Figure 4.2, provide information about the surface morphology of the films. The surface roughness of Pt (111) and Pt (001) films was found to be comparable and relatively low, with values of 0.6 nm and 0.4 nm, respectively. In contrast, Pt (110) exhibited a significantly higher surface roughness of 1.8 nm. To accurately determine the spin Hall angle (θ_{SH}), the resistivity of the individual Pt layers was extracted by growing additional Pt/TaN films with the corresponding crystal

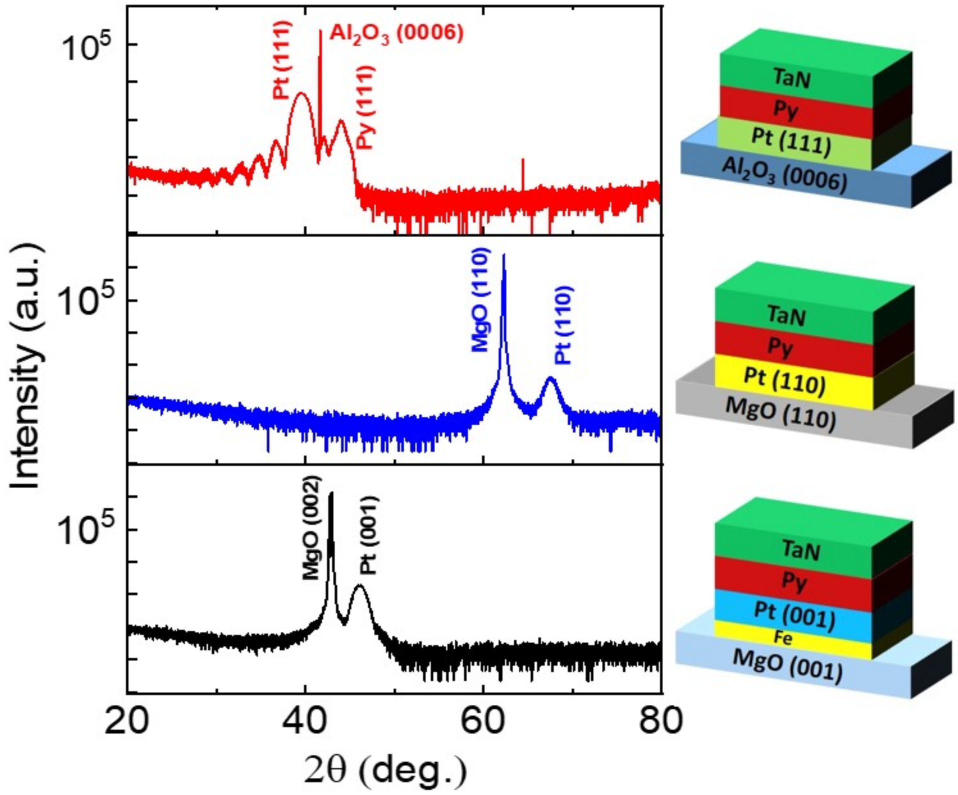

Figure 4.1: (a) XRD Data of Pt (111), Pt (110) and Pt (100) films respectively (from up to down). The distinct peaks of Pt (111), Pt (110) and Pt (001) shows the crystallinity of the films. (b) Schematics of respective films structure.

orientations. The measured resistivity values for the bare Pt (111), Pt (110), and Pt (001) layers were 18 ± 1 μΩ-cm, 30 ± 4 μΩ-cm, and 33 ± 1 μΩ-cm, respectively. It is worth noting that these resistivity values did not reflect the large surface roughness observed in Pt (110).

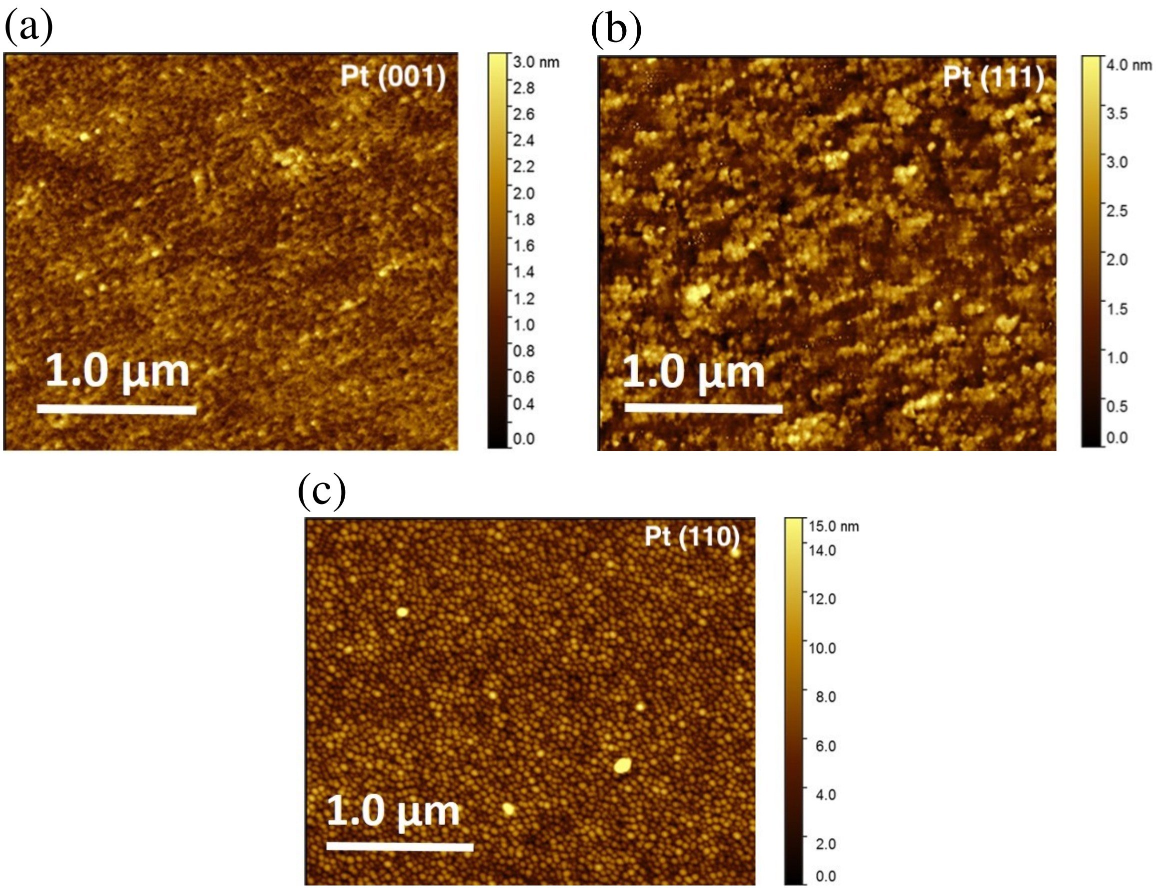

Figure 4.2: Atomic Force Microscope (AFM) images of Pt(001), Pt(111), and Pt(110) (from left to right) respectively.

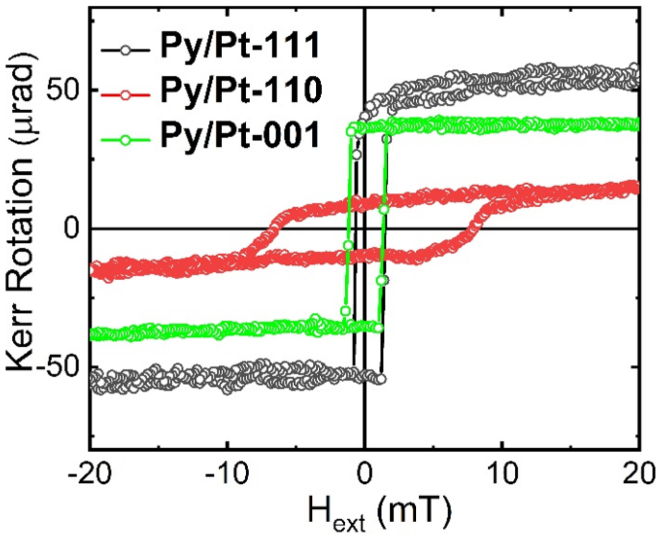

Figure 4.3: Static MOKE data of three films, respectively. The films Pt(001) and Pt(111) show a similar value of MOKE signal and correctivity H_C. Except in the case of Pt(110) where inhomogeneity causes the small and large values of MOKE signal and correctivity respectively.

However, the impact of surface roughness was evident in the in-plane magneto-optical Kerr effect (MOKE) hysteresis curves. Figure 4.3 clearly illustrates that the magnitude of the MOKE signal for Pt (110) is more than 50% weaker compared to the other crystal orientations. Furthermore, the switching transition, represented by the coercivity (H_C), of Pt/Py (111) and Pt/Py (001) films is sharper and smaller, indicating a more uniform magnetization texture in these films.

4.3 OFMR Measurement

Figure 4.4 presents the schematic of the optically detected ferromagnetic resonance (OFMR) setup. In the OFMR technique, a Ti:Sapphire femtosecond laser with a central wavelength of $\lambda = 800$ nm and a repetition rate of $\Delta f = 80$ MHz is used to probe the magnetization using polar magneto-optical Kerr effect (MOKE). The external microwave signal, phase-locked with the laser pulses using the Synchrolock-AP system (Coherent, Inc.), is utilized to excite the magnetization. The microwave current, modulated at 1 kHz, is sent through a gold wire to the sample, inducing magnetization excitation. An external in-plane magnetic field (H_{ext})

is applied at an angle of 45° with respect to the current direction. The precession of the magnetic moment ($\vec{\mathrm{m}}$) is probed by measuring the out-of-plane component of the magnetic moment ($\mathrm{m_z}$) using polar MOKE. An optical delay stage is employed to control the relative phase (delay) between the laser pulses and the microwave signals. The response of OFMR can be recorded in two ways: 1) by sweeping the phase between the microwave signal and the laser pulses at a constant external magnetic field, or 2) by sweeping the magnetic field at a fixed phase.

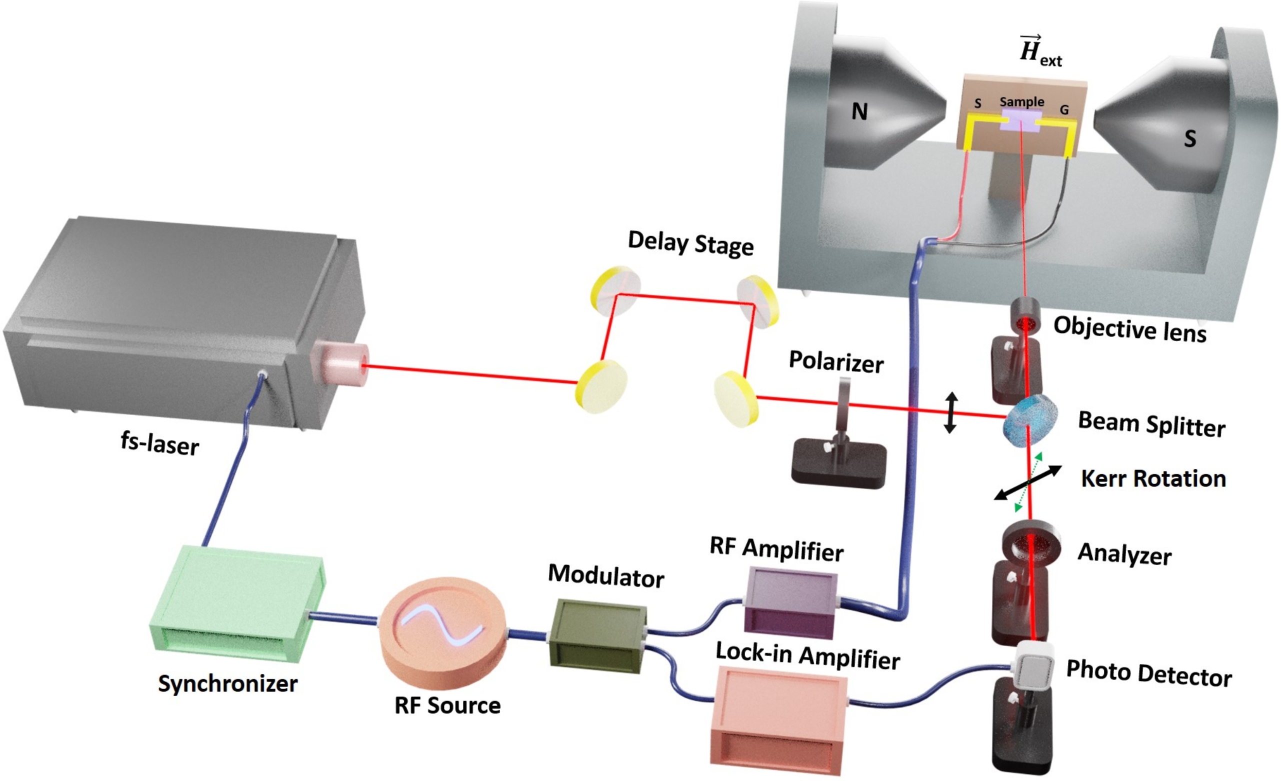

Figure 4.4: Schematic figure of optically detected ferromagnetic resonance (OFMR) set up: A fs laser pulses emanating from the Vitara oscillator (Coherent Inc.) are aligned in free space via mirrors and optical delay line. A phase-locked external microwave signal is injected into the device. Precession of the magnetization is probed via polar MOKE geometry.

4.3.1 Delay Sweep Measurement

As the name suggests, in delay sweep measurement, the delay between microwave and laser pulses is swept at a constant magnetic field. At each value of the magnetic field, the response of the magnetic moment is sinusoidal, as can be seen in the figure 4.5a below. From this response, the amplitude of magnetic moment (m_Z) and the relative phase of magnetic moment with respect to the driving microwave field can be obtained by using the equation.

$$m_Z = A\sin\left(\frac{2\pi t}{T} + \Theta\right) \tag{4.1}$$

The relationship between the amplitude of the magnetic moment (A) and the phase (Θ) of m_Z is described by an equation. The time period (T) of the magnetic moment oscillation is determined by the frequency of the microwave signal. By applying this equation at different values of the external magnetic field (H_{ext}), the corresponding amplitudes (A) can be obtained. The dependence of A on H_{ext} yields the resonance curve for the magnetic material under investigation.

In Figure 4.5b, the resonance curve for Py(5)/Pt(5) (where the numbers in parentheses represent the thickness in nm) is presented. The plot illustrates that initially, as H_{ext} increases, the magnitude of A also increases. At a specific field, known as the resonance field (H_{res}), A reaches its maximum value. However, further increase in H_{ext} causes a decrease in the magnitude of A, resulting in a symmetric Lorentzian-shaped curve, as shown in Figure 4.5b.

Figure 4.6a demonstrates the resonance spectra for different frequencies ranging from 6.24 to 13.52 GHz. The linewidth (ΔH) of these spectra, defined as the full width at half maximum (FWHM), is proportional to the effective Gilbert damping (α_{eff}) of the material. The relationship between ΔH and the frequency (f) allows for an estimation of the effective Gilbert damping coefficient (α) (as shown in figure 4.6b).

$$\Delta H = \Delta H_0 + \frac{2\pi\alpha f}{\gamma} \tag{4.2}$$

(a)

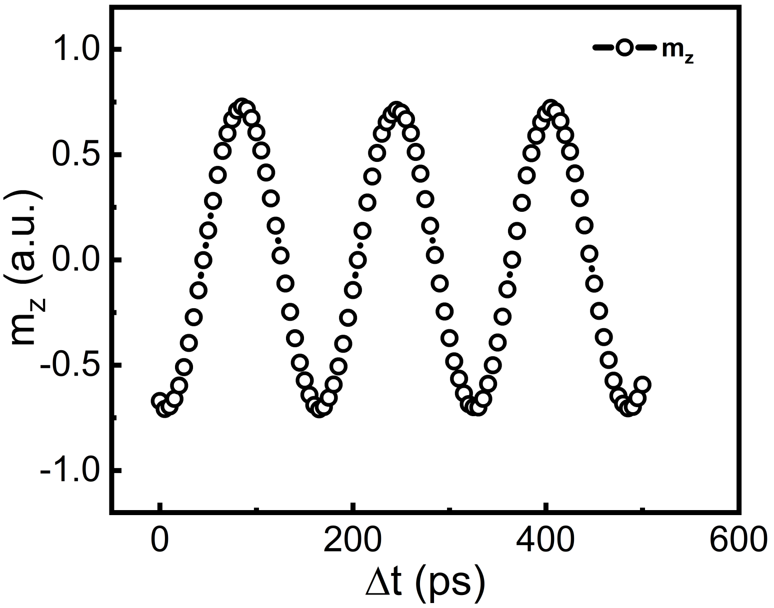

(b)

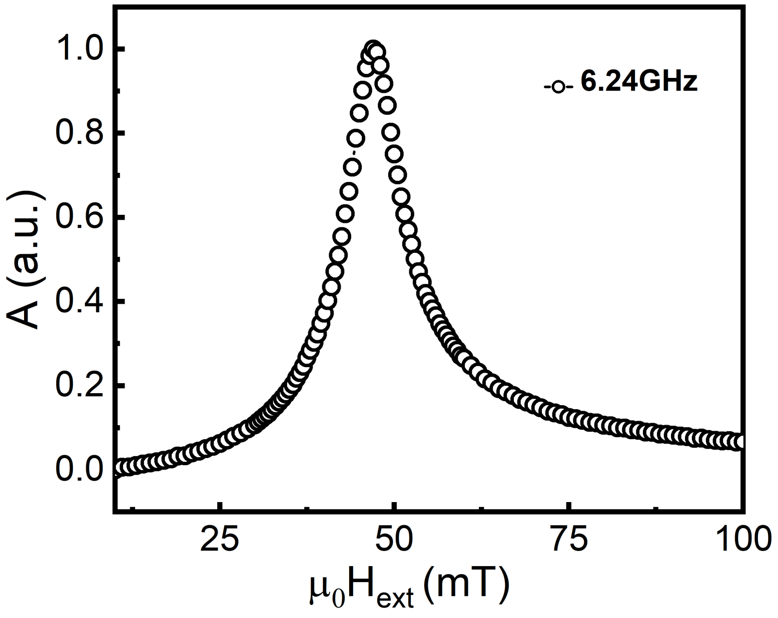

Figure 4.5: (a) The Oscillation of magnetic moment (m_z), oscillation period corresponds to the frequency of RF excitation. The above oscillation is recorded at 6.24 GHz for Py(5)/Pt(5)/Si0$_2$/Si sample. (b) Resonance curve (raw data) at 6.24 GHz for Py(5)/Pt(5)/Si0$_2$/Si sample in OFMR delay sweep measurement. The values of Amplitude (A) at different H_{ext} obtained from the equation (4.1)

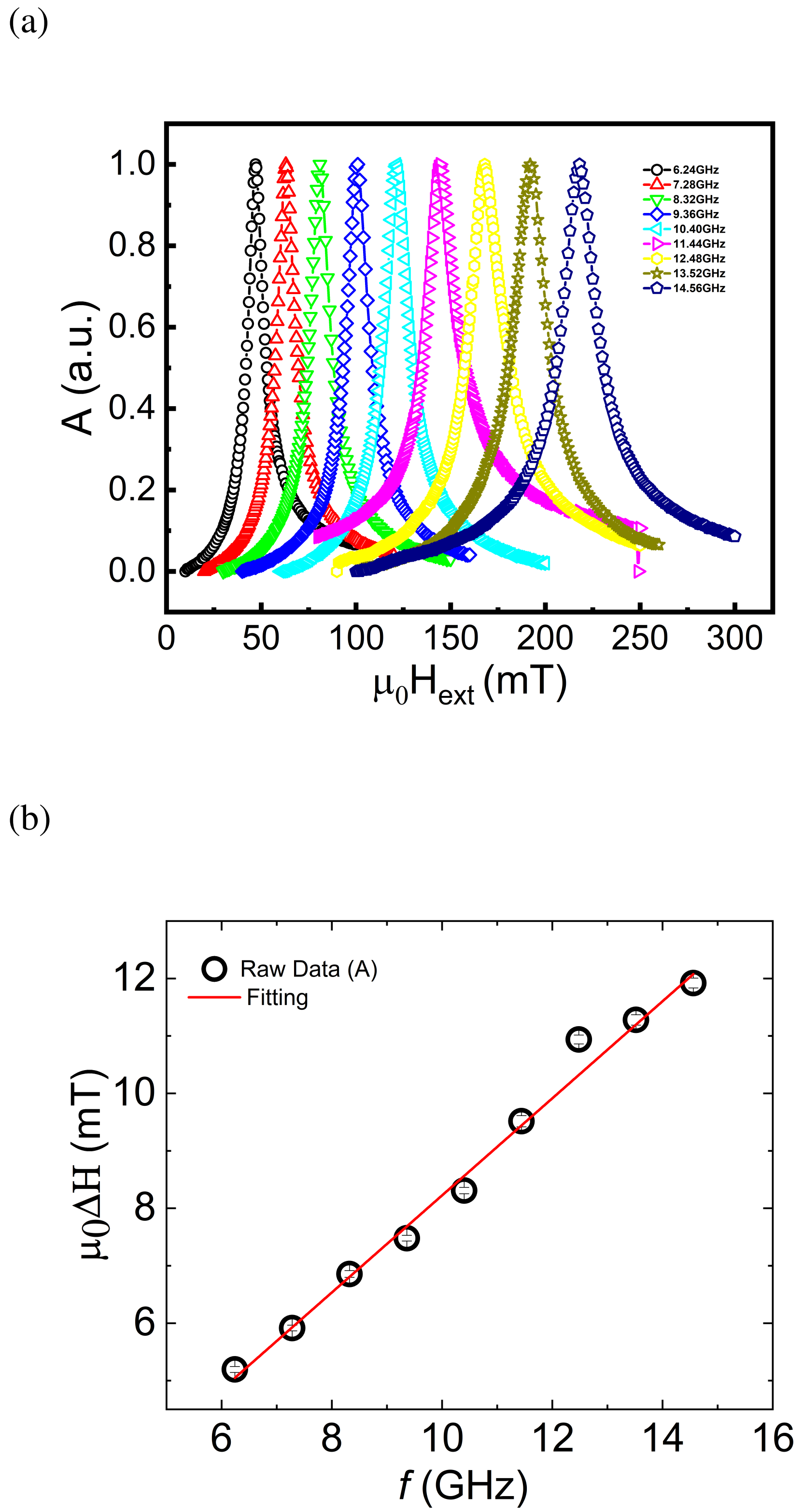

Figure 4.6: (a) Resonance spectra's at different frequencies from 6.24 to 13.52 GHz. (b) Dependence of Linewidth ΔH on frequency(f). The fitted red line is given by equation 4.2.

4.3.2 Field Sweep Measurement

In field sweep measurement, the field is swept at the arbitrary phase between microwave and laser pulses. The OFMR response in this case is a linear combination of symmetric and asymmetric parts of the Lorentzian function. The symmetric and asymmetric part is proportional to the real and imaginary part of the susceptibility of the magnetization and is given by equation 3.14.

$$\delta m_z = h_0 \left(\chi'_{xy} \cos\phi + \chi''_{xy} \sin\phi \right) \tag{4.3}$$

Where χ'_{xy} and χ''_{xy} are the real and imaginary part of the susceptibility tensor [70]. ϕ is the relative phase between microwave excitation and laser. The χ'_{xy} and χ''_{xy} are given by the equations 4.4.

$$\begin{aligned} \chi'_{xy} &= \frac{M_s \frac{\omega}{\gamma}}{2(2H+M_s)} \frac{\delta H}{(H-H_0)^2+\delta H^2} \\ \chi''_{xy} &= \frac{M_s \frac{\omega}{\gamma}}{2(2H+M_s)} \frac{(H-H_0)^2}{(H-H_0)^2+\delta H^2} \end{aligned} \tag{4.4}$$

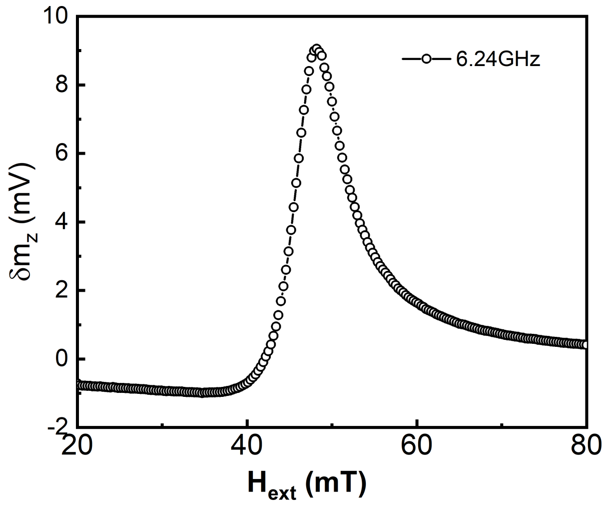

Figure 4.7: The resonance curve in field sweep measurement of OFMR. The shape of the curve depends on the relative phase (ϕ) of the laser pulse and microwave signal.

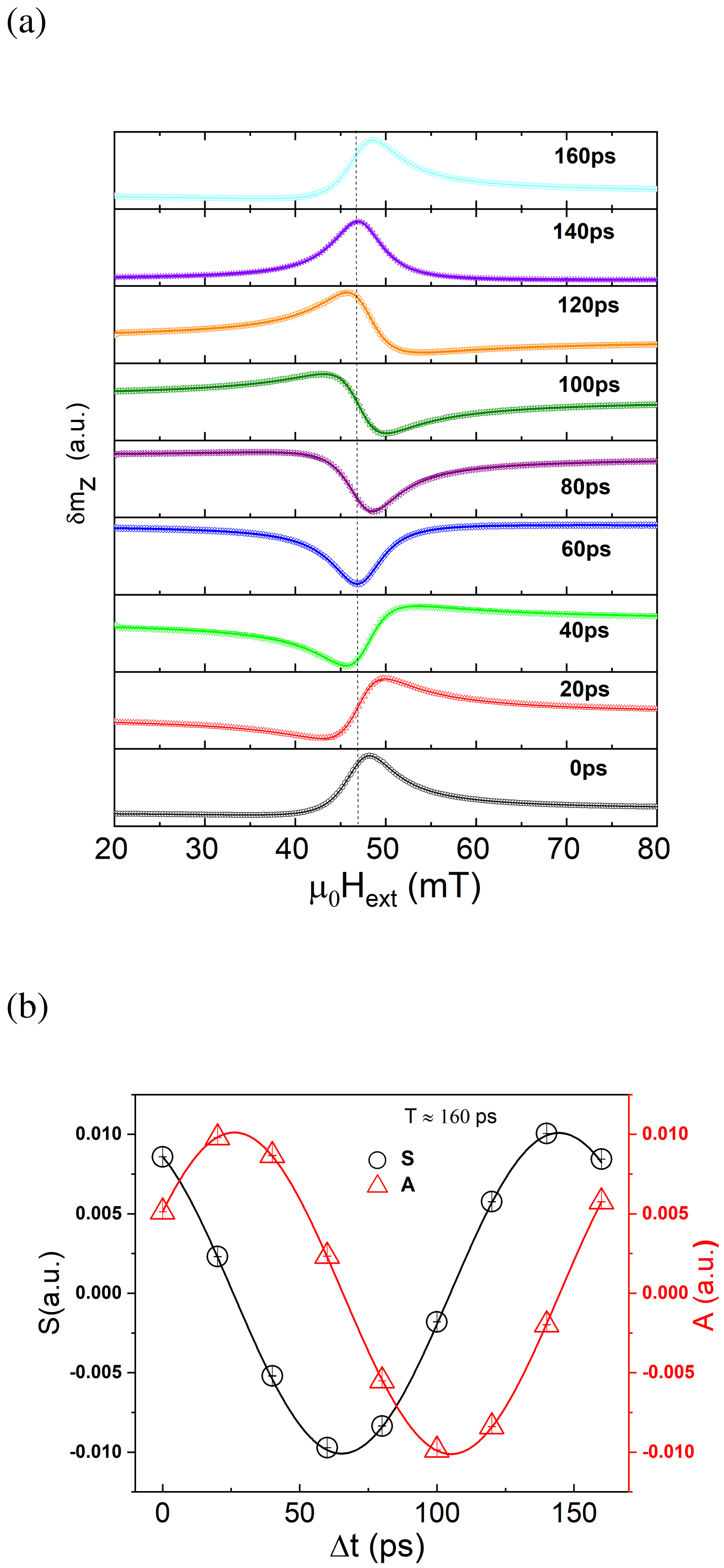

Figure 4.8: (a) OFMR traces at different delays(or phase ϕ) between laser pulses and microwave signal at 6.24GHz. It is important to note that the trace repeats itself after one cycle of RF signal ($\Delta t \sim$ 160ps corresponds to 6.24GHz in the frequency domain).(b) The values S and A represent the coefficients of the symmetric and asymmetric parts of the Lorentzian function. The ratio of S/A depends on the relative phase of the laser and microwave signal.

It is worth pointing out that the shape of the curve in field sweep measurement depends on the relative phase(ϕ) of the RF with respect to the laser pulse. By varying the phase or delays (Δt) by one cycle, the shape of the curve can be repeated, as evident from figure 4.8.

4.4 STFMR Measurement

Figure 4.9 shows the schematic of STFMR setup and the oscillations of the magnetic moment and various torques acting on it. This oscillation of the AMR and microwave current produces the rectified mix voltage (V_{mix}) across the FM/HM bilayer, which can be measured by DC Nano-voltmeter or lock-in amplifier. The OFMR and STFMR measurements were performed on the same devices. The samples were patterned by optical lithography followed by Ar ion-milling to define devices of area $25\times\mu m^2$. A detailed explanation of the STFMR setup is given in the later section.

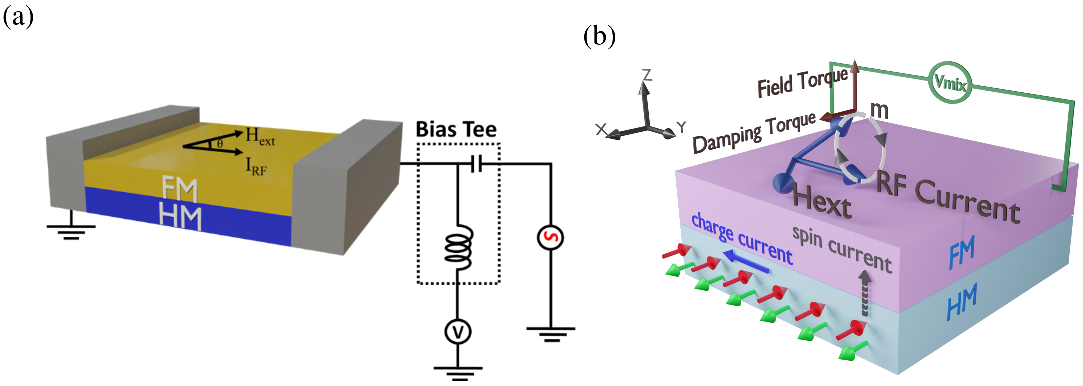

Figure 4.9: (a) Schematic of spin-torque ferromagnetic resonance (STFMR) setup. Bias tee is used to mix the microwave and DC current and at the same time to detect the DC voltage (V_{mix}) built across FM/HM bilayer. (b) Illustration of the precession of magnetic moment and torques: An RF current passes through FM/HM (Ferromagnet/Heavy Metal) bilayer and generates an RF spin torque which excites the magnetization. Due to the precession of the magnetization, anisotropic magnetoresistance(AMR) becomes also oscillatory. Oscillating AMR and RF current produces a rectified voltage, which can be measured by a lock-in amplifier or nano DC voltmeter. The arrow represents the directions of in-plane (Damping like torque τ_{DL}) and out-of-plane torques (Field like or Oersted torque τ_{FL})

4.5 Comparison of OFMR and STFMR Measurement

In this section, the detailed comparison of STFMR and OFMR measurement is presented. Figure 4.10 presents an example of the measured STFMR and OFMR spectra of Al_2O_3(0001)/Pt/Py the sample at 6-13 GHz and 6.24-13.52 GHz, respectively. Each STFMR spectrum is composed of symmetric and antisymmetric signals that stem, respectively, from the spin-orbit torque (SOT) and Oersted field contributions [89] [22]. In contrast, the OFMR traces were measured at an arbitrary delay between the optical pulses and the microwave excitation. Each OFMR response comprises a linear combination of real and imaginary parts of the susceptibility, χ' and, χ'' respectively. Namely, the measured traces can be either purely symmetric or antisymmetric or a combination of both. The linear combination is determined by the phase between the optical pulses and the microwave excitation, which is different at each frequency, as seen in the figure 4.10 (b). To extract the resonance field and the linewidth, each trace was decomposed into the symmetric and antisymmetric parts, similar to the procedure applied for STFMR measurements [89]. The resonance field, H_{res}, and the linewidth, ΔH, can be determined in the STFMR and OFMR responses by fitting the measured spectra to a sum of symmetric and antisymmetric Lorentzian functions according to the following equation :

$$V_{E/O} = V_{S_{E/O}} \frac{\Delta H^2}{(H - H_{res})^2 + \Delta H^2} + V_{A_{E/O}} \frac{(H - H_{res})\Delta H}{(H - H_{res})^2 + \Delta H^2} \tag{4.5}$$

Where V_S and V_A are the symmetric and anti-symmetric parts of the Lorentzian and the sub-index E or O indicates the electrical STFMR or optical OFMR method. From the above equation, parameters like linewidth (ΔH) and resonance field (H_{res}) are obtained. The extracted frequency dispersion curves are summarized in Fig. 4.11 (a), (b), (c) and (d) for the STFMR and OFMR measurements, respectively. The traces obtained by both methods are similar. Using the Kittel formula

$$f = \frac{\mu\gamma}{2\pi} \sqrt{(H_{res} + H_K)(H_{res} + M_{eff} + H_K)} \tag{4.6}$$

Value of effective magnetization, $\mu_0 M_{eff} \sim 1012 \pm 2$ mT(993 ± 4 mT), 700 ± 6mT

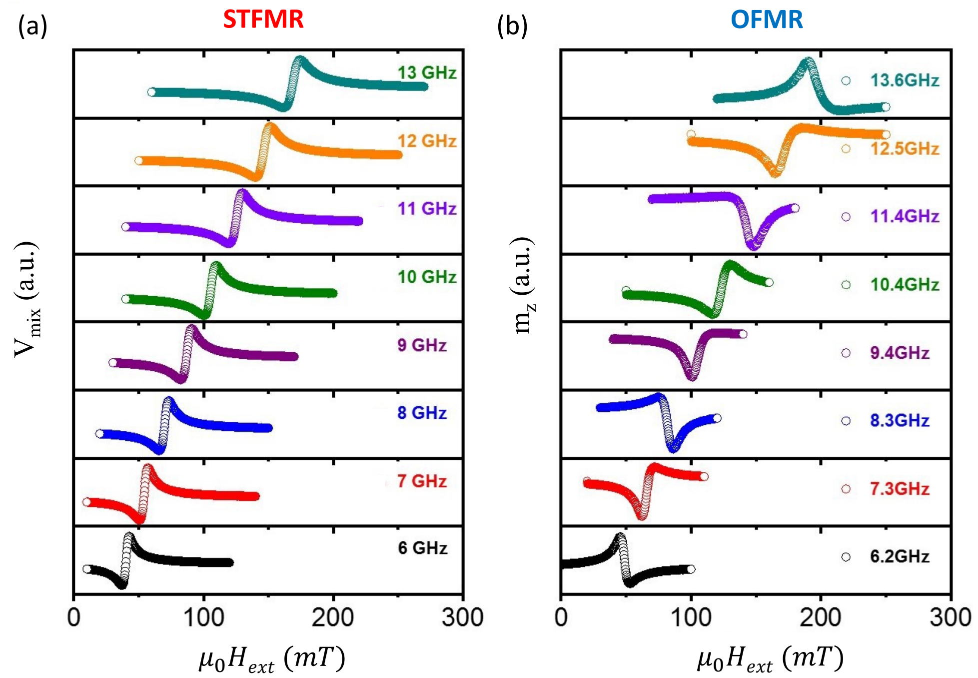

Figure 4.10: Examples of measured spectra taken for a device fabricated from Al_2O_3(0001)/Pt/Py at RF frequencies from 6 GHz to 13.5 GHz. (a) STFMR and (b) OFMR spectra's.

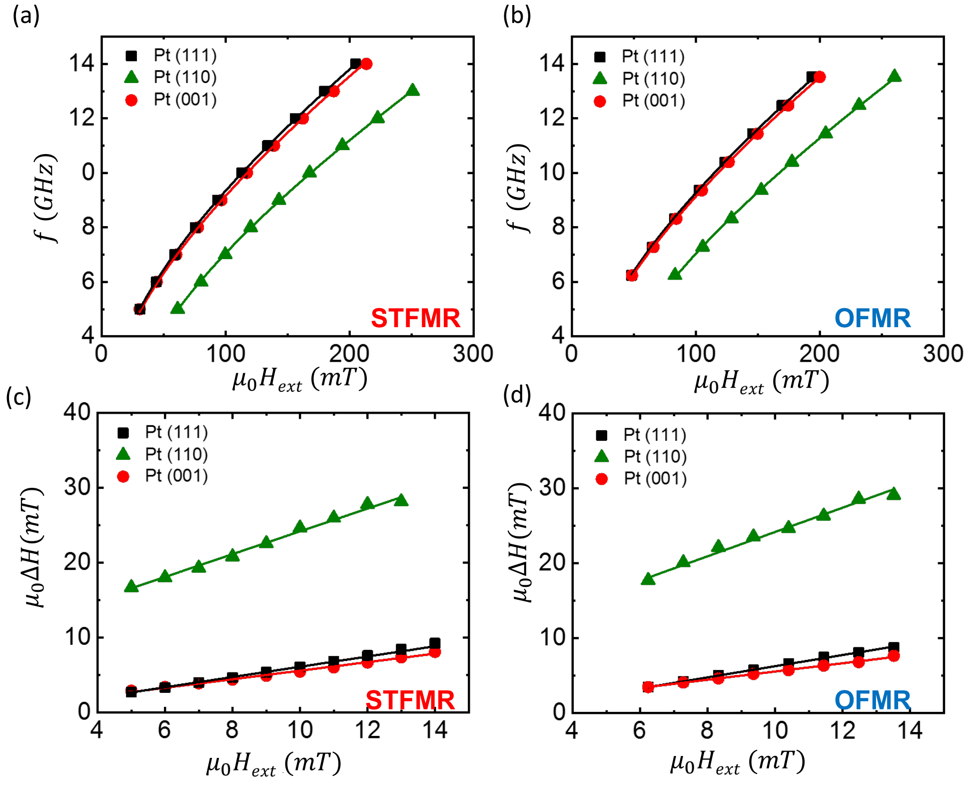

Figure 4.11: (a) Frequency dispersion curves measured by (a) STFMR and (b) OFMR Linewidth measurements obtained by (c) STFMR and (d) OFMR.

(730± 10 mT), and 968 ± 3 mT (970 ± 1 mT) for the Pt (111), Pt (110), and, Pt (001) films, respectively, was extracted for the STFMR (OFMR) measurements. γ = 178GHz/T for Py and $\mu_0 = 4\pi \times 10^{-7}$H/m are the gyromagnetic ratio and the magnetic permeability of free space. The in-plane anisotropy value H_K was negligible in Pt(111) and Pt(001), but significant in Pt (110) where it was 19 ± 0.2 mT (22 ± 0.1 mT) as extracted by the STFMR (OFMR). The value of $\mu_0 M_{eff}$ for the Pt (110) film appears to be lower by $\sim$ 30 % as compared to the values for Pt (111) and Pt (001). Additionally, the $\mu_0 M_{eff}$ values as measured by the optical and electrical methods for Pt (111) and Pt (001) agree within an error that is smaller than 1 % while the difference for the Pt (110) is significantly larger, reaching almost 5%. This behavior can be attributed to surface roughness. The same trend can also be seen in the figure 4.12 saturation magnetization, M_S, values measured by a vibrating sample magnetometer(VSM).

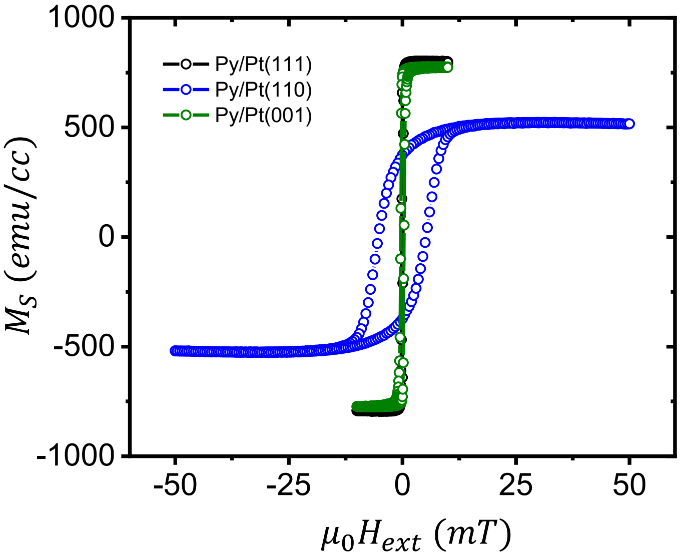

Figure 4.12: VSM data for Pt (111), Pt (110) and Pt (001) films.

The Gilbert damping parameter, α was extracted from ΔH measurements using the relation:

$$\mu_0 \Delta H = \mu_0 \Delta H_0 + \frac{2\pi\alpha f}{\gamma} \tag{4.7}$$

ΔH_0 arises from inhomogeneous broadening and disorder in the crystalline structure.

Figures 4.11 present the measurements of ΔH. The values of α obtained are $19.28 \pm 0.35 \times 10^{-3}$ ($20.9 \pm 0.2 \times 10^{-3}$), $42.86 \pm \times 10^{-3}$($45.7 \pm 2 \times 10^{-3}$), and $16.08 \pm 0.1 \times 10^{-3}$ ($15.4 \pm 0.2 \times 10^{-3}$) for the Pt (111), Pt (110), and Pt (001), for the STFMR (OFMR) respectively. These values are consistent with other reports [92]. Despite the larger values of α for the Pt (110) sample, both the optical and electrical methods give very similar values. The values of ΔH_0 extracted from equation 4.7 are 0.1 ± 0.15 mT(0.07 ± 0.06 mT), 9 ± 0.50mT(8 ± 0.6mT), and 0.7 ± 0.08mT(1.1 ± 0.07mT) for the Pt(111), Pt(110), and, Pt (001), as measured by the STFMR (OFMR), respectively. Here, as well, the STFMR and OFMR methods agree very well. The large ΔH_0 value of Pt (110) as compared to the other orientations illustrates quantitatively the conclusions drawn from the qualitative analysis of the static MOKE (as shown in figure 4.3) and the influence of the surface roughness on the measured magnetization dynamics. The side-by-side comparison of these values in bar plots are shown in Fig. 4.13

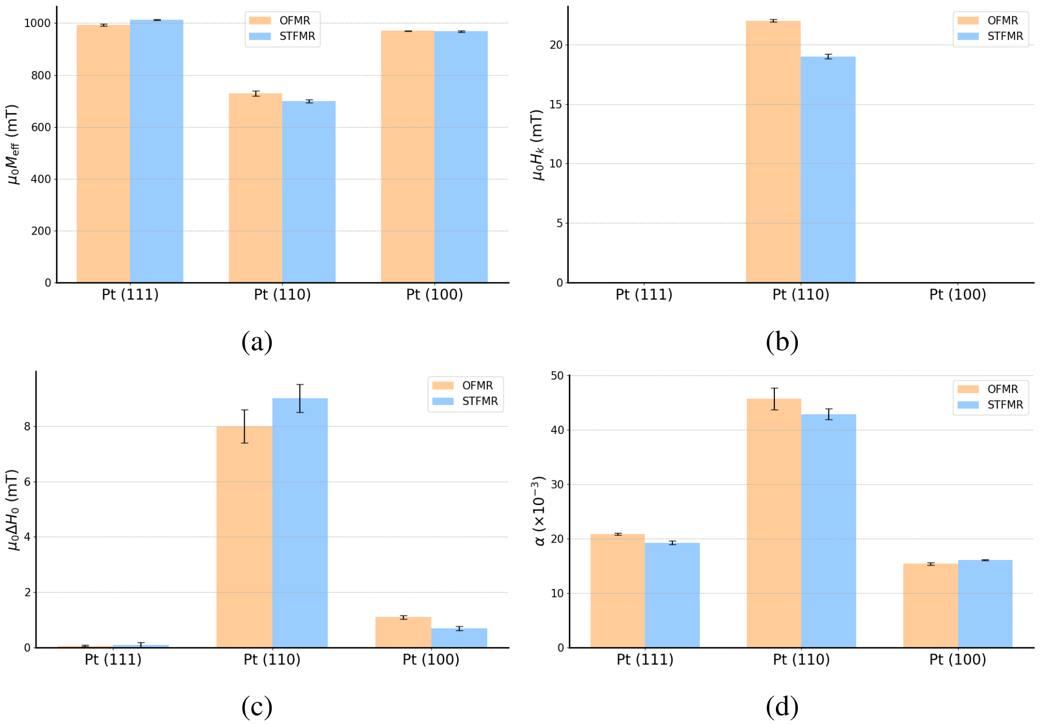

(a) (b)

(c) (d)

Figure 4.13: Comparison of parameters: (a) Effective magnetization ($\mu_0 M_{\mathrm{eff}}$), (b) In-plane anisotropy ($\mu_0 H_k$), (c) Inhomogeneous broadening ($\mu_0 \Delta H_0$), and (d) Gilbert damping parameter (α) from OFMR and STFMR, respectively.

4.6 Quantification of Spin Hall angle (θ_{SH}) using DC bias measurement

The spin Hall angle θ_{SH} was determined through measurements of DC bias linewidth modulation. The DC spin current density J_S flowing in the Pt layer induces DC spin currents that modulate the linewidth change ΔH of the Py layer through a damping/anti-damping spin-orbit torque (SOT) effect. The resulting effective damping α_{eff} is linearly proportional to J_S and can be described by the following relation [93]:

$$\alpha_{eff} = \alpha_0 + \frac{\sin\varphi}{(H_{res} + 0.5M_{eff})(\mu_0 M_S t)} \frac{\hbar J_S}{2e} \tag{4.8}$$

In the above equation, 4.8, φ is the angle between the charge current and the externally applied field, which is 45° in both techniques, and t is the thickness of the Py layer. The above equation can be written more conveniently from which θ_{SH} can be extracted as follows:

$$\theta_{SH} = \frac{\delta\Delta H/\delta\Delta I_{DC}}{\frac{2\pi f}{\gamma}\left[\frac{\sin\varphi}{(H_{res}+0.5M_{eff})(\mu_0 M_S t_{Py})}\right]} \left[\frac{\rho_{Py} t_{Pt} + \rho_{Pt} t_{Py}}{\rho_{Py}}\right] w \tag{4.9}$$

Here I_{DC} is the bias current and $\delta\Delta H$ is the variation in ΔH as a result of I_{DC}. ρ_{Pt} and ρ_{Py} are the resistivities of Pt, and Py, respectively, and w is the width of the device. From equations 4.8 and 4.9, it is seen that when the external field is reversed, $\sin\phi$ changes sign, i.e., the dependence of ΔH on I_{DC} is also reversed.

The linewidth data at 6.24 GHz and 6 GHz for OFMR and STFMR, respectively, with varying DC bias currents (I_{DC}), are shown in Figure 4.14. The linear dependence of the relative linewidth change ($\delta\Delta H$) on I_{DC} is clearly observed. It is also evident that the maximum applicable current in the optical measurements (OFMR) is nearly four times larger compared to the electrical measurements (STFMR). This limitation in STFMR arises from the fact that the detection of STFMR relies on the anisotropic magnetoresistance (AMR) of the ferromagnetic (FM) layer. As the DC current (I_{DC}) increases, the background DC voltage also increases, which is a function of AMR and the external magnetic field

(a)

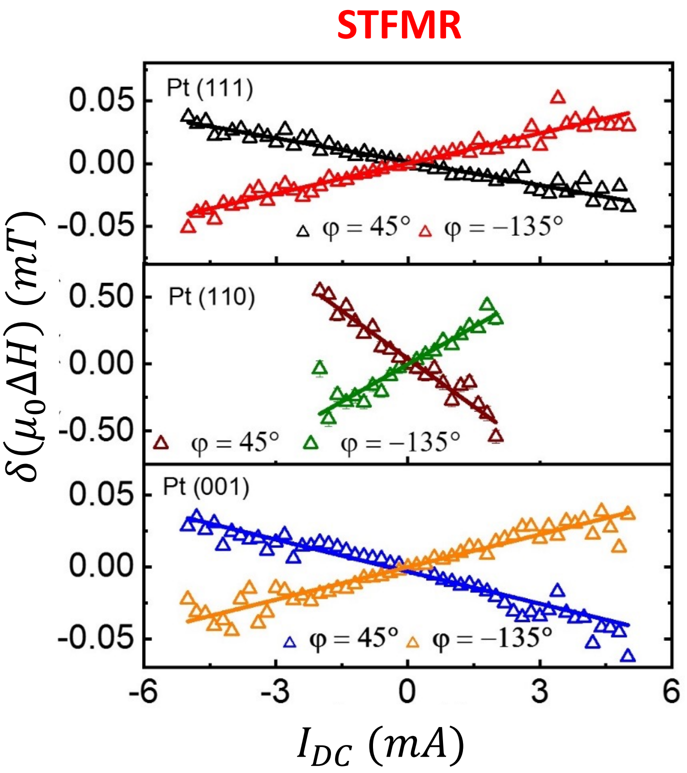

(b)

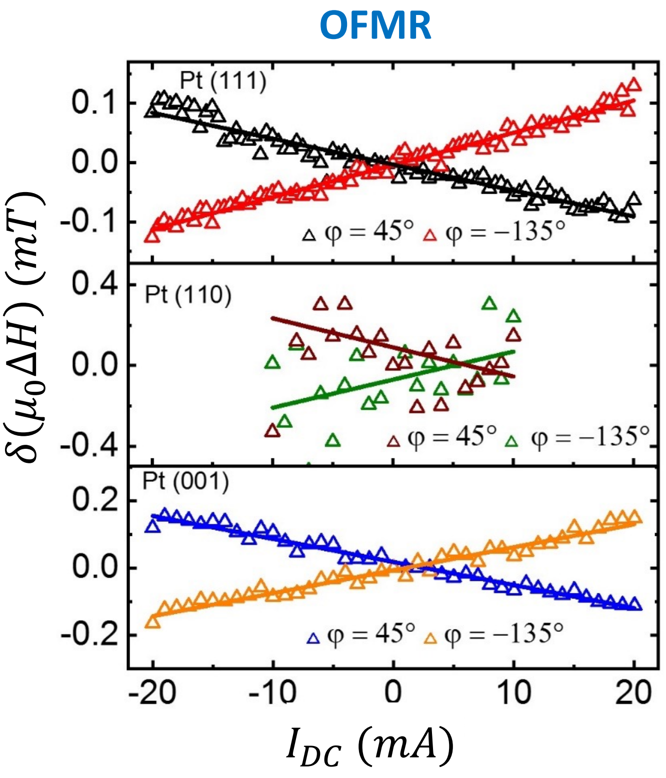

Figure 4.14: Current dependent linewidth broadening at 6 GHz and 6.24 GHz for Pt (111), Pt (110), and Pt (100) (a) in STFMR and (b) in OFMR, respectively.

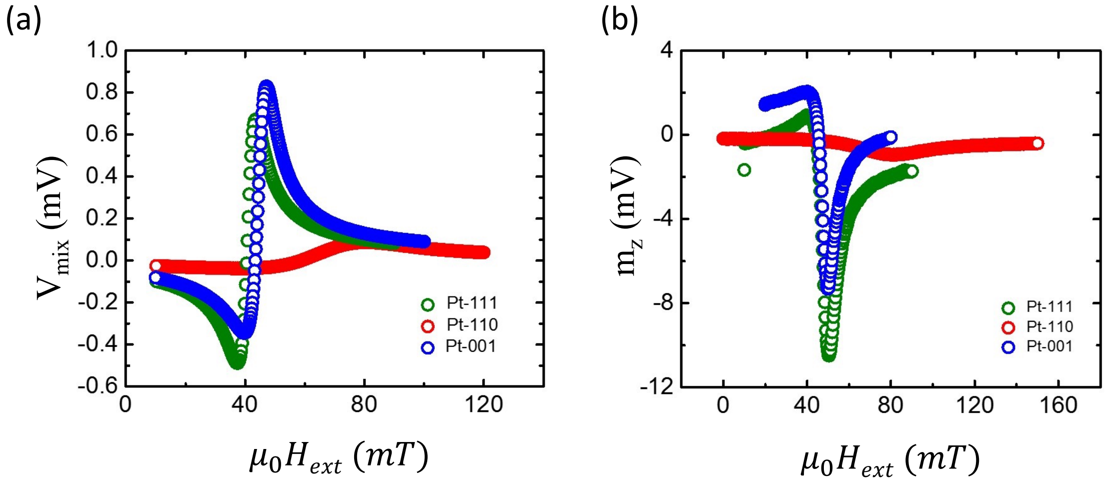

Figure 4.15: STFMR and OFMR zero bias spectra for Pt (111), Pt (110) and Pt (001).

(H_{ext}) [22]. Specifically, away from the resonance field H_{ext}, higher-order contributions of AMR become prominent, especially in the case of large damping (α) or inhomogeneous broadening (ΔH_0). Consequently, the shape of the STFMR spectra away from resonance at higher current densities introduces unwanted noise, leading to a lower signal-to-noise ratio (SNR) in the measurement.

In contrast, the OFMR signal relies solely on the Kerr rotation of the FM layer, which is a direct consequence of the magnetization of the FM layer, making it highly sensitive. These observations indicate that the sensitivity of STFMR is limited by the background detection voltage (V_{mix}) rather than the noise of the magnetic signal itself. Since the OFMR signal is based on the magnetization and is less prone to artifacts, changes in the linewidth ($\delta\Delta H$) with respect to the DC current (I_{DC}) can be studied over a wider range of current densities, allowing for a more accurate quantification of θ_{SH} (slope of the linewidth modulation).

This conclusion holds true for all samples except for Pt (110). Surprisingly, in Pt (110), the OFMR data is much noisier than the STFMR data, which clearly exhibits a linear dependence on I_{DC}. The θ_{SH} values explain this contradiction. For Pt (111) and Pt (001), the values of θ_{SH} obtained from STFMR (OFMR) are 0.053 ± 0.01 (0.043 ± 0.01) and 0.072 ± 0.01 (0.068 ± 0.01), respectively. These results indicate that both methods yield relatively close θ_{SH} values. However, for Pt (110), there is a significant discrepancy, with an unusually large θ_{SH} value of 0.45 ± 0.2 obtained using STFMR, while OFMR results in 0.09 ± 0.03. Additionally, for all measurements, the θ_{SH} values from STFMR are larger than those obtained using OFMR, except for Pt (110) where the difference is abnormal. This observation suggests that one of the measurements is more prone to artifacts and yields an inaccurate value of θ_{SH}. These contradictory values of θ_{SH} can be explained as follows:

As shown earlier, the VSM and MOKE data for Pt (110) films (Figure 4.3 and Figure 4.12) indicate small magnetic signals and a large coercivity (H_C). The OFMR and STFMR data also exhibit a large inhomogeneous linewidth broadening (ΔH_0) (shown in Figure 4.15) and weaker signals for Pt (110) compared to the other films (by almost an order of magnitude). As stated above, the application of I_{DC} shifts the DC baseline, and together with the weak V_{mix} signal of Pt (110), it results in measurement artifacts that eventually lead to an incorrect θ_{SH} value of 0.45. The OFMR results in a correct value of 0.09, from which we conclude that the STFMR data in this case is erroneous. The error-induced linewidth modulation in STFMR for Pt (110) at 8 GHz is shown in Figure 4.16. Additionally, the STFMR data in the other crystal orientations are affected by the same artifact, but in these cases, V_{mix} is larger, and the STFMR measurement is more reliable, except for a systematic offset in the STFMR θ_{SH} measurement. The values of θ_{SH} for Pt (111) and Pt (001) are larger by approximately 20% compared to OFMR.

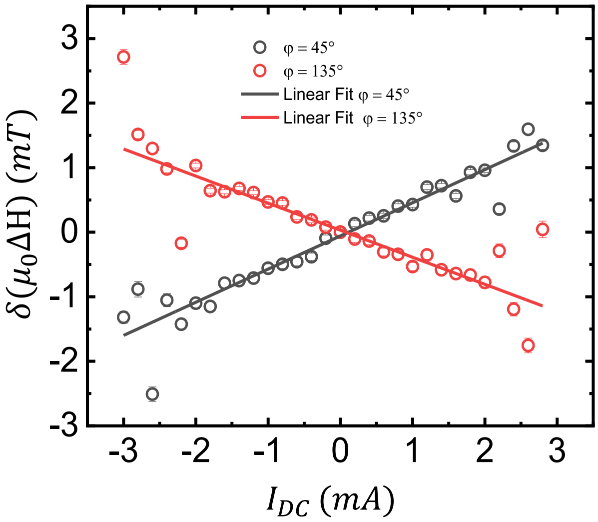

Figure 4.16: Error induced linewidth modulation for Pt(110) in STFMR at 8GHz. The value of θ_{SH} obtained from this data is ∼ 0.4 ± 0.2.

4.6.1 Interface Transparency (T)

Interface plays a important role when it comes to calculating the θ_{SH}. The spin current generated in HM layer $\hbar J_{int}$ is usually larger than the spin current $\hbar/2J_{SH}^{T}$ that diffuses into FM layer [92]. These two quantities is determined by interface transparency(T) [92].

$$T = \frac{G_{\uparrow\downarrow}\tanh(\frac{d}{2\lambda})}{G_{\uparrow\downarrow}\coth(\frac{d}{2\lambda}) + \frac{\sigma_{Pt}}{\lambda}\frac{h}{2e^2}} \tag{4.10}$$

Where d is the thickness of HM layer (Pt in our case), h is Planck's constant, λ and σ_{Pt} are the spin diffusion length and conductivity of Pt layer, respectively. When λ is relatively smaller than d, the parameter $G_{\uparrow\downarrow}$ is related to the spin mixing conductance G_{eff} [94].

$$G_{\uparrow\downarrow} = G_{eff}\frac{\frac{\sigma_{Pt}}{\lambda}\frac{h}{2e^2}}{\frac{\sigma_{Pt}}{\lambda}\frac{h}{2e^2} - G_{eff}} \tag{4.11}$$

Where spin mixing conductance G_{eff} is given by [95] [96].

$$G_{eff} = \frac{4\pi M_s t}{g\mu_B}(\alpha_{FM/HM} - \alpha_{FM}) \tag{4.12}$$

Where M_S, t, g, μ_B, $\alpha_{FM/HM}$ and α_{FM} are saturation magnetization, thickness of FM, Kittel's g-factor, Bohr magneton, effective damping of FM/HM bilayer and damping of single FM layer respectively.

The intrinsic spin Hall angle ($\theta_{SH\text{–}intrinsic}$) and effective spin Hall angle (θ_{SH}) are related by

$$\theta_{SH\text{–}intrinsic} = \frac{\theta_{SH}}{T} \tag{4.13}$$

The following table summarizes the transparency values of Pt (111) and Pt(001) samples

Table 4.1: Interface transparency values of Pt-111 and Pt-001 samples.

Sample	Pt-111	Pt-001
T (OFMR/STFMR)	0.4827	0.6338

In above calculation, we have used $\alpha_{Py} = 0.008$ for 5nm film. In Pt (110) the damping is too high and the assumptions of the model do not hold resulting in a transparency that is greater than 1. Overall, the $\theta_{SH-Intrinsic}$ of Pt (111) and Pt (001) are close in both OFMR and STFMR measurement. The values of θ_{SH} and $\theta_{SH-Intrinsic}$ are summarized in table below 4.2. For better illustration of the comparison, the bar graphs are plotted in figures 4.23 and 4.24 in the conclusion and discussion section below.

Table 4.2: Summary of θ_{SH} for Pt (111), Pt (110), Pt (001), and textured Pt (Pt/SiO$_2$) films measured by OFMR and STFMR.

Sample	θ_{SH} OFMR	θ_{SH} STFMR	Intrinsic θ_{SH} OFMR	Intrinsic θ_{SH} STFMR
Pt(111)	0.043 ± 0.01	0.053 ± 0.01	0.089 ± 0.01	0.109 ± 0.01
Pt(110)	0.09 ± 0.03	0.45 ± 0.2	N.A.	N.A.
Pt(100)	0.068 ± 0.01	0.072 ± 0.01	0.107 ± 0.01	0.113 ± 0.02
Pt/Si/SiO$_2$	0.08 ± 0.01	0.09 ± 0.01	0.12 ± 0.01	0.14 ± 0.01

4.6.2 Field like torque efficiency ξ_{FL} estimation

In this section, we calculate the field-like torque efficiency (ξ_{FL}) using the DC bias method in both OFMR and STFMR measurements. As mentioned earlier, in STFMR and OFMR, the magnetic moment ($\vec{m}$) in the FM layer is excited by three torques: the damping-antidamping torque (τ_{DL}), the Oersted torque (τ_{Oe}), and the field-like torque (τ_{FL}). Typically, in STFMR, there are multiple methods to estimate τ_{FL}, but they require complicated analyses such as precise estimation of the microwave current in the HM layer and different FM thicknesses [77]. Here, we utilize the DC bias method described earlier to calculate τ_{FL}.

In the presence of DC bias, the total effective field (H_{eff}) can be written as:

$$H_{eff} = H_{ext} + H_{Oe,dc} + H_{FL,dc} \tag{4.14}$$

Here, H_{ext}, $H_{Oe,dc}$, and $H_{FL,dc}$ represent the applied external field, the Oersted field, and the effective field of τ_{FL} due to the DC spin current flowing into the FM layer, respectively. Therefore, in the DC bias method, the changes in the resonance field at a given current (I) ($\Delta H_{res}(I) = H_{res}(I) - H_{res}(I = 0)$) are the vector projection of the effective fields $H_{Oe,dc}$ and

$H_{FL,dc}$, given by:

$$\Delta H_{res}(I) = -(\Delta H_{Oe,dc} + \Delta H_{FL,dc}) \sin\varphi \tag{4.15}$$

Here, φ represents the angle between the external magnetic field (H_{ext}) and the current (I). Since the thickness of the device is smaller than the width, H_{Oe} can be expressed as $\mu_0 J_{HM} d/2$ according to Ampere's law, where μ_0, J_{HM}, and d are the relative permeability of free space, the charge current density in the HM layer, and the thickness of the HM layer, respectively. Similarly, the effective field $H_{FL,dc}$ can be written as $\xi_{FL}\left[\frac{\hbar}{2e}\right]\left[\frac{1}{\mu_0 M_S t_{FM}^{eff} J_{HM}}\right]$, where ξ_{FL}, $\hbar$, e, $\mu_0 M_S$, and t_{FM}^{eff} represent the field-like torque efficiency, the reduced Planck constant, the electronic charge, the relative permeability of free space, the saturation magnetization, and the effective thickness of the FM layer, respectively. Therefore, Eq. 4.15 can be written as:

$$\Delta H_{res} = -\left[\frac{J_{HM} d}{2} + \xi_{FL}\frac{\hbar}{2e}\frac{1}{\mu_0 M_S t_{FM}^{eff} J_{HM}}\right]\sin\varphi \tag{4.16}$$

From the parallel model of current flow, $J_{HM} = \Delta I\left[\frac{R_{FM}}{R_{FM}+R_{HM}}\right]\left[\frac{1}{A_{c,HM}}\right]$. Therefore, we can express:

$$\frac{\Delta H_{res}}{\Delta I}\frac{R_{FM}+R_{HM}}{R_{FM}}\frac{A_{c,HM}}{\sin\varphi} = -\frac{d}{2} - \xi_{FL}\frac{\hbar}{2e}\frac{1}{\mu_0 M_S t_{FM}^{eff}} \tag{4.17}$$

Finally, we can calculate ξ_{FL} using the equation:

$$\xi_{FL} = \frac{2e}{\hbar}\left[\frac{\Delta H_{res}}{\Delta I}\frac{R_{FM}+R_{HM}}{R_{FM}}\frac{A_{c,HM}}{\sin\varphi}S - \frac{d}{2}\right]\mu_0 M_S t_{FM}^{eff} \tag{4.18}$$

The factor S can be ±1 depending on the geometry of the structure (FM/HM or HM/FM). The term $\frac{\Delta H_{res}}{\Delta I}$ represents the slope of the changes in H_{res} with respect to the current (I).

It is worth noting that changes in H_{res} can also be caused by the thermal effect of electrical current joule heating ($\Delta H_{res} \propto 4\pi M_{eff} \propto \Delta T \propto \Delta P_{diss} \propto \Delta I^2$). The thermal effect is an even function of the current and does not depend on the polarity of the charge current. Therefore, the odd part of the changes in H_{res} represents the contributions from both the

Oersted and field-like torques. By separating the odd and even components of H_{res} using $([H_{res}(I) - H_{res}(0)] \pm [H_{res}(-I) - H_{res}(0)])/2$, where (+) and (–) represent the even and odd components, respectively, we can accurately determine the field-like torque contribution. Figures 4.17 and 4.20, 4.18 and 4.21, and 4.19 and 4.22 represent the separation of the even and odd parts of H_{res} from the raw data (H_{res} vs I) for the Pt(111), Pt(110), and Pt(001) samples in OFMR and STFMR, respectively. Table 4.3 summarizes the values of ξ_{FL} obtained. In the case of Pt(110), OFMR and STFMR measurements disagree, which can be attributed to the broader STFMR signal and the lower signal-to-noise ratio (SNR) resulting from the additional DC bias. This leads to an inaccurate value of ξ_{FL} in STFMR.

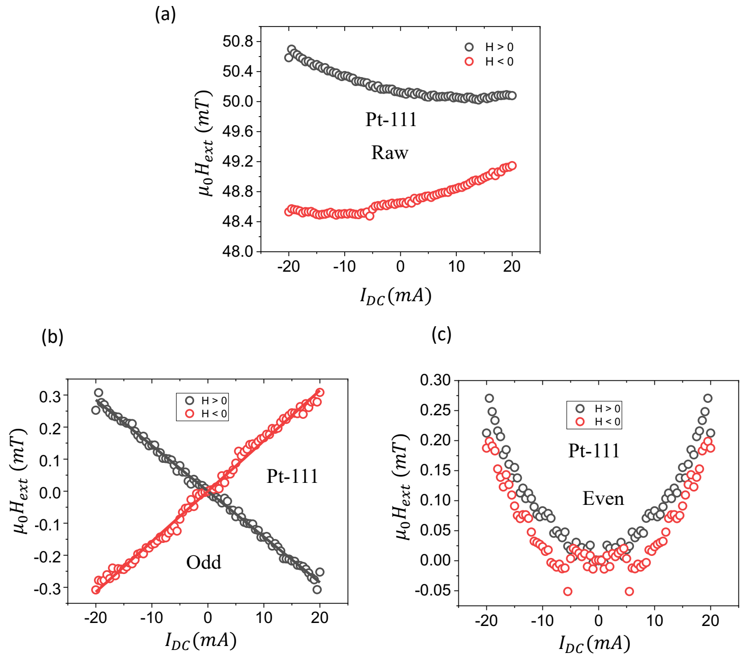

Figure 4.17: OFMR measurement of Pt (111).(a) Variations in H_{res} with respect to DC current for the positive and negative field.(b) and (c) are the odd and even components of H_{res} that represents the field like torque and Joule heating, respectively.

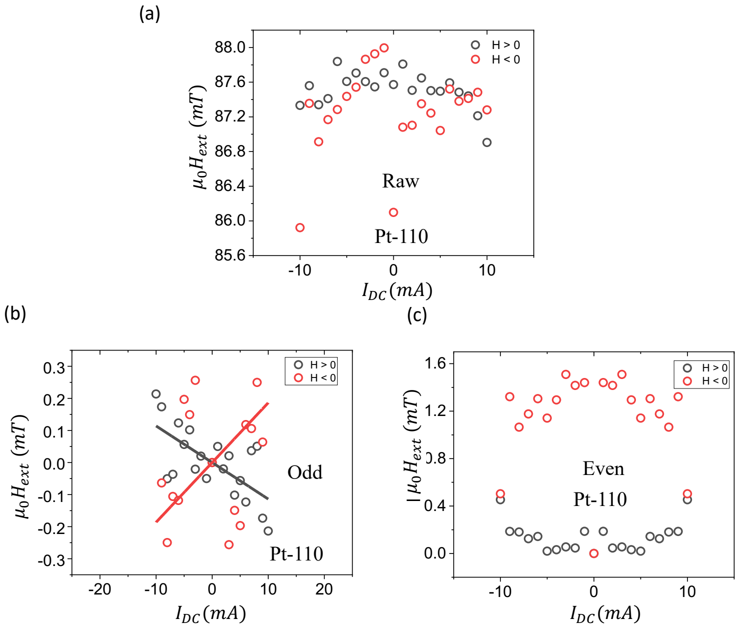

Figure 4.18: OFMR measurement of Pt (110).(a) Variations in H_{res} with respect to DC current for the positive and negative field.(b) and (c) are the odd and even components of H_{res} that represents the field like torque and Joule heating, respectively.

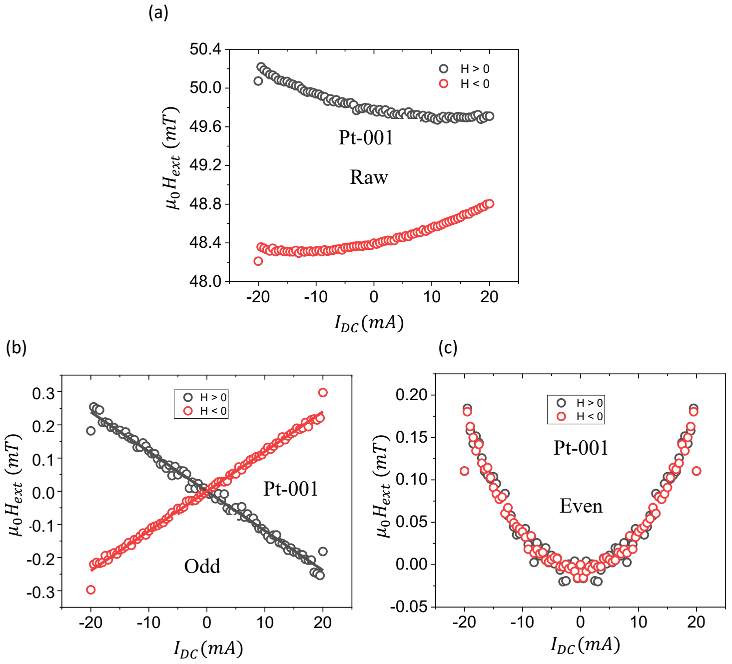

Figure 4.19: OFMR measurement of Pt (001).(a) Variations in H_{res} with respect to DC current for the positive and negative field. (b) and (c) are the odd and even components of H_{res} that represents the field like torque and Joule heating, respectively.

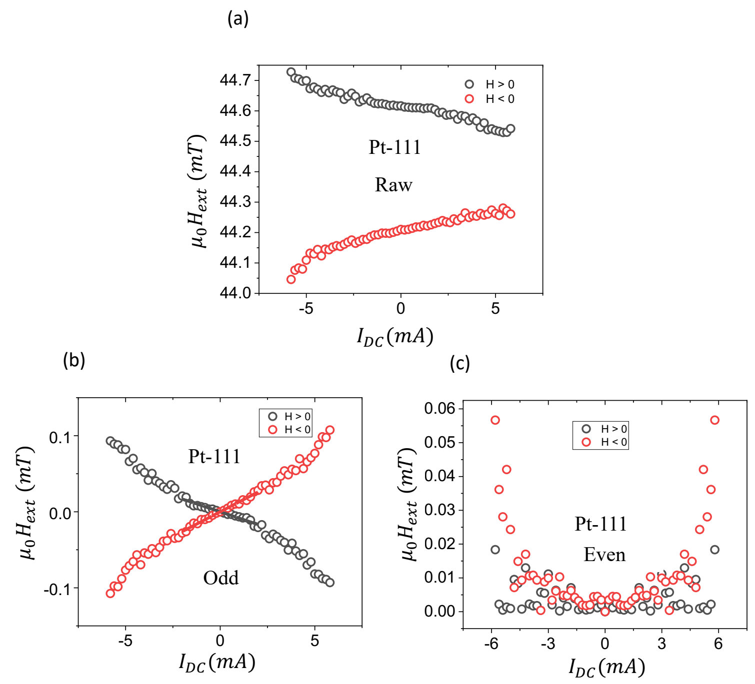

Figure 4.20: STFMR measurement of Pt (111).(a) Variations in H_{res} with respect to DC current for the positive and negative fields. (b) and (c) are the odd and even components of H_{res} that represents the field like torque and Joule heating, respectively. The linear fitting is limited to the linear regime of the data.

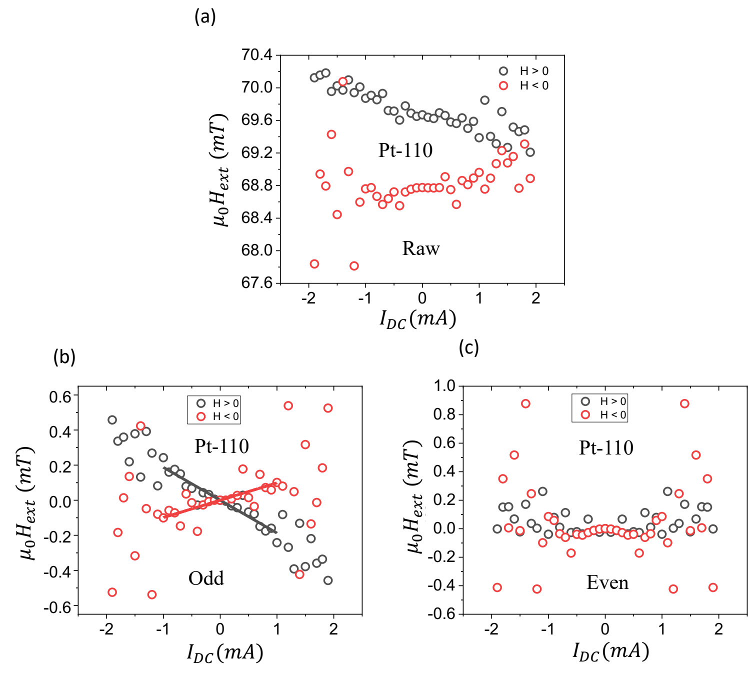

Figure 4.21: STFMR measurement of Pt (110). (a) Variations in H_{res} with respect to DC current for positive and negative field. (b) and (c) are the odd and even components of H_{res} that represent the field like torque and Joule heating, respectively. The linear fitting is limited to the linear regime of the data.

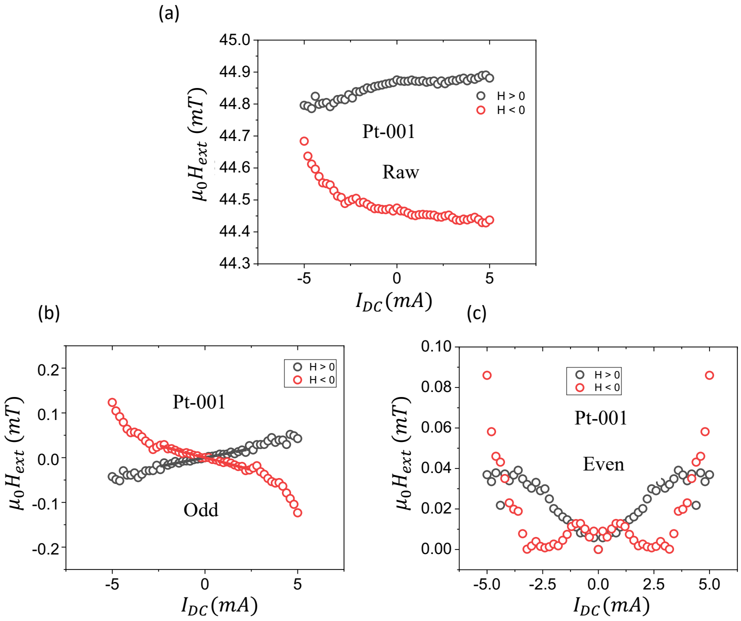

Figure 4.22: STFMR measurement of Pt (001). (a) Variations in H_{res} with respect to DC current for positive and negative field. (b) and (c) are the odd and even components of H_{res} that represent the field like torque and Joule heating, respectively. The linear fitting is limited to the linear regime of the data.

Table 4.3: Summary of the ξ_{FL} values of Pt (111), Pt (110), and Pt (001) films from OFMR and STFMR techniques

ξ_{FL}	Pt(111)	Pt(110)	Pt(001)
OFMR	0.08 ± 0.01	0.04 ± 0.02	0.04 ± 0.01
STFMR	0.05 ± 0.01	0.29 ± 0.2	0.03 ± 0.02

4.7 Conclusion and Discussion

In this chapter, we investigated the crystallographic dependence of the spin Hall angle (θ_{SH}) in epitaxial Pt thin films of Pt(111), Pt(110), and Pt(001) using both optical (OFMR) and electrical (STFMR) techniques. Our results demonstrate that the measurement of θ_{SH} using OFMR is more reliable than the conventional STFMR technique, particularly in cases where the FMR signal is weak and broad, such as in the Pt(110) film. We observed significant changes in θ_{SH} (20-30%) with respect to crystallographic orientation (Pt(111) to Pt(001)), as shown in Table 4.2. Due to the ambiguity in the results for Pt(110), particularly with

STFMR, we consider the value of θ_{SH} obtained from OFMR to be more accurate. The side by side comparison of θ_{SH} are shown in fig. 4.25.

For comparison, we also grew a textured Pt film along the (111) direction with the same structure: Si/SiO$_2$/Pt(5)/Py(5) (units in nm). This film exhibited a resistivity of $27 \pm 2\mu\Omega$-cm, damping constant α of $(14.0 \pm 1) \times 10^{-3}$, and inhomogeneous linewidth broadening ΔH_0 of 1.15 ± 0.3 mT, resulting in a θ_{SH} value of 0.09 ± 0.01 (STFMR) and 0.08 ± 0.01 (OFMR). We also estimated other parameters such as transparency (T), intrinsic spin Hall angle, and field-like torque efficiency (ξ_{FL}) for these films. Once again, we observed that OFMR provides a better estimation of these parameters due to its immunity to electrical noise and its local measurement nature compared to the non-local/global STFMR technique.

In summary, we developed a local optical technique called OFMR to measure θ_{SH} and compared it with the standard STFMR technique. Accurately determining θ_{SH} is crucial for characterizing the power efficiency of spintronics devices.

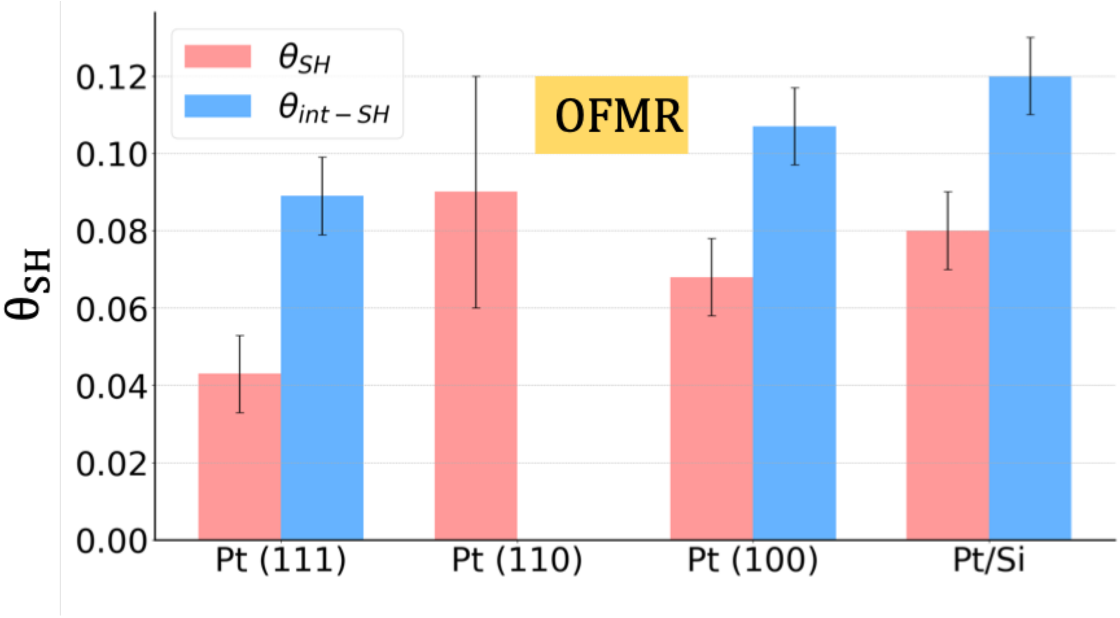

Figure 4.23: Values of θ_{SH} and $\theta_{int\text{–}SH}$ for Pt(111), Pt(110), Pt(100) and Pt/Si from OFMR measurement

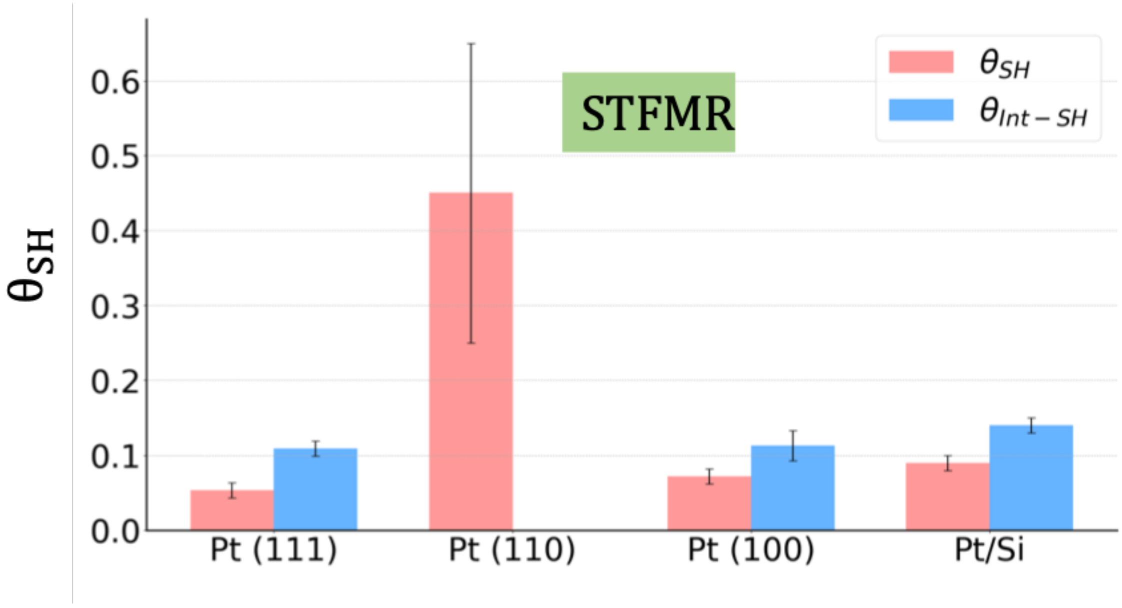

Figure 4.24: Values of θ_{SH} and θ_{int-SH} for Pt(111), Pt(110), Pt(100) and Pt/Si from STFMR measurement

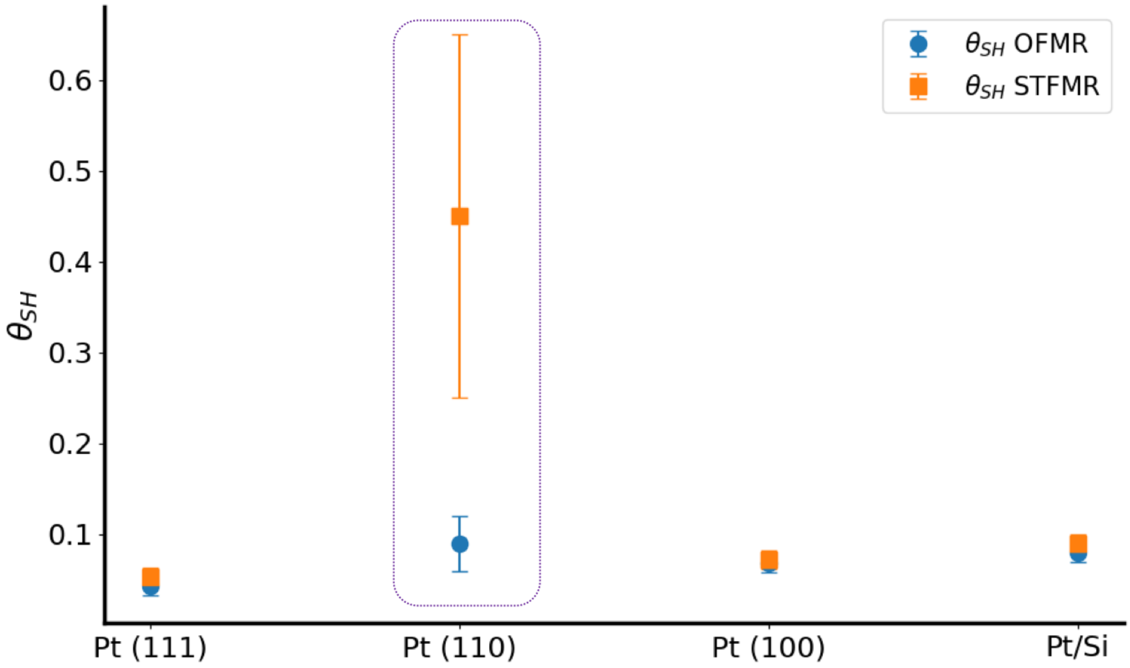

Figure 4.25: Side by side comparison of θ_{SH} values for different crystallographic directions in Pt from OFMR and STFMR measurements. The dotted rectangular box highlights the discrepancies in θ_{SH} for Pt(110).

5

Crystallographic Dependence of Spin Orbit Torques in Epitaxial Mn_3Pt thin films

5.1 Introduction

In recent years, there has been significant interest in current-induced spin-orbit torques (SOT) due to their potential applications in spintronics and their ability to manipulate the magnetization of adjacent ferromagnetic layers [97, 98, 99]. Heavy metals (HM) are commonly used as spin current source materials due to their large spin Hall angle (θ_{SH}) resulting from the conventional spin Hall effect (CSHE) caused by strong spin-orbit coupling (SOC) or the Rashba-Edelstein effect (REE) [100, 5]. The spin polarization in CSHE is even under time-reversal symmetry (TRS). In this case, the in-plane anti-damping torque

($\tau_{AD,y}$) is expressed as ($\mathbf{m} \times \mathbf{m} \times \sigma_y$), which is even under magnetization reversal, while the out-of-plane field-like torque ($\tau_{FL,y}$) is expressed as ($\mathbf{m} \times \sigma_y$), which is odd under magnetization reversal. Here, **m** represents the magnetization of a ferromagnet (FM), and σ_y represents the spin current polarization along the **y** direction.

In HM/FM bilayer systems with perpendicular magnetic anisotropy (PMA), magnetization switching is primarily achieved through the large $\tau_{AD,y}$ originating from spin current with polarization σ_y. However, one major technical challenge associated with current-induced switching using HM is the requirement of a finite in-plane biased field, as CSHE provides a pure in-plane damping-like torque. Consequently, there has been a significant burst in scientific activities to search for novel materials that can generate spin currents deviating from σ_y, with a special emphasis on collinear and non-collinear antiferromagnets, as well as 2D materials [101, 102, 103, 63, 104, 105].

Spin currents with out-of-plane spin polarization σ_z were first observed in low crystalline symmetric (orthorhombic) 2D materials in bilayer structures such as WTe_2/Py, where the broken crystal mirror symmetry contributes to the generation of σ_z [102]. A similar spin current with σ_z was also observed in relatively higher crystalline (hexagonal) $NbSe_2$/Py bilayer systems due to uniaxial strain [103]. Furthermore, σ_z was observed in low symmetric point group heavy metal CuPt/CoPt bilayer systems, where H_x-free magnetization switching was demonstrated [106]. In addition to broken crystal mirror symmetry, broken magnetic symmetry has been proposed as another effective way to generate σ_z in collinear antiferromagnets (AFMs) such as IrMn and Mn_2Au, as well as non-collinear AFMs such as Mn_3Sn, Mn_3Pt, and Mn_3SnN [63, 105, 107].

However, previous studies did not observe spin currents with σ_x polarization. Nevertheless, spin currents with all three polarizations (σ_x, σ_y, and σ_z) were observed in the non-collinear AFM Mn_3GaN, and spin current with only σ_y polarization was observed in $\gamma-Mn_3Ir$ [83, 101], which also belong to the non-collinear AFM family. Although non-collinear AFMs exhibit higher structural symmetry (either cubic or tetragonal), the unconventional torques in these systems differ, highlighting the need for further investigation. Moreover, it is worth noting that the interface between a heavy metal (HM) layer and a non-collinear antiferromagnetic (AFM) layer exhibits a substantial exchange bias (EB) field. Surprisingly, the influence of this EB field on the spin-orbit torque (SOT) phenomenon has not been adequately investigated in prior studies.

Mn_3Pt is a cubic non-collinear AFM that can exhibit two magnetic domain structures, denoted as T1 and T2 (shown in Fig. 5.1). Previous studies on SOT in Mn_3Pt focused on the T2 domain configuration, but the exchange bias effect between the FM and Mn_3Pt has not been extensively studied with both domain configurations [63].

In this chapter, we investigate the spin torque effects in Mn_3Pt/Py and Mn_3Pt/Cu/Py systems using spin torque ferromagnetic resonance (ST-FMR). We explore the behavior of Mn_3Pt with (111) and (001) orientations, both exhibiting a T1 domain configuration. Additionally, we examine the influence of exchange bias on different SOT phenomena by introducing a thin Cu layer between Mn_3Pt and Py.

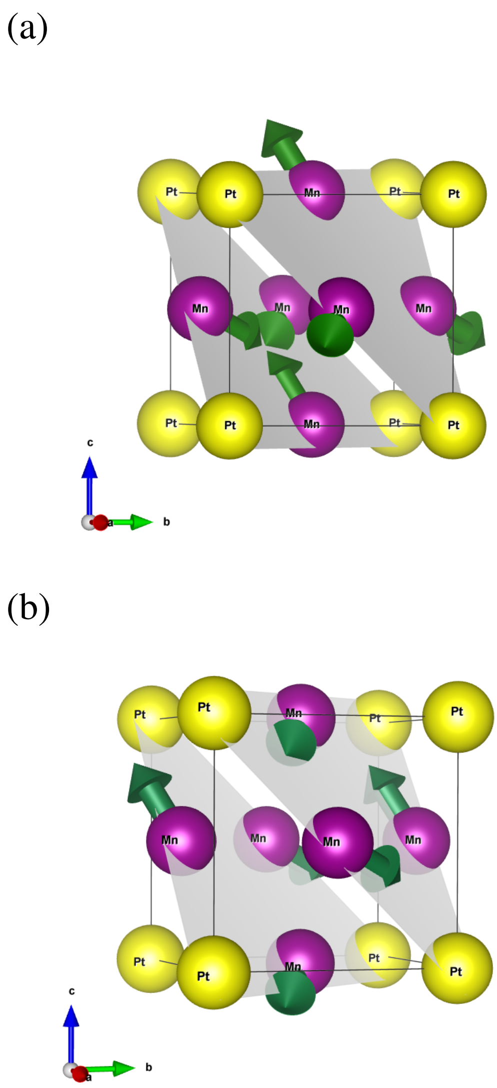

Figure 5.1: The (a) T1 and (b) T2 configurations of Mn_3Pt are represented in the images generated using VESTA software.

5.2 Sample Preparation and the Characterization

Mn_3Pt is a cubic non-collinear antiferromagnet in which magnetic moment of three Mn atoms form triangular spin arrangement in the (111) plane, (as shown in Fig. 5.1). It shows non-collinear AFM ground state at room temperature and goes through a collinear AFM phase at T $\sim$ 365K and finally paramagnetic phase at $T_N \sim$ 475K. High quality epitaxial thin films of 10 nm thick Mn_3Pt with (111) and (001) orientations were grown at 500°C on TaN buffered Al_2O_3(0001) and directly on STO(001) substrates respectively using ultra high vacuum DC magnetron sputtering. A 5 nm thick $Ni_{80}Fe_{20}$ (Py) layer was sputtered directly on top of the 10 nm thick Mn_3Pt layer at room temperature. Another two sets of samples with 10 nm thick Mn_3Pt were also prepared by inserting 2 nm Cu layer in between Mn_3Pt and Py. All the films were capped with 3 nm TaN layer to prevent oxidation. Figure 5.2 shows typical out-of-plane X-ray diffraction (XRD) patterns for both the samples. Furthermore, transverse ϕ scans confirm the single crystalline nature of $Mn_3Pt(111)$ and $Mn_3Pt(001)$ as shown in Fig. 5.4. Atomic force microscopy (AFM) micrograph displays a smooth surface with r.m.s. roughness close to 0.5 nm (Shown in Fig. 5.3). Single-layer Mn_3Pt films with a thickness of 10 nm were also deposited on substrates $Al_2O_3(0001)$ and STO(001), enabling the characterization of their properties.

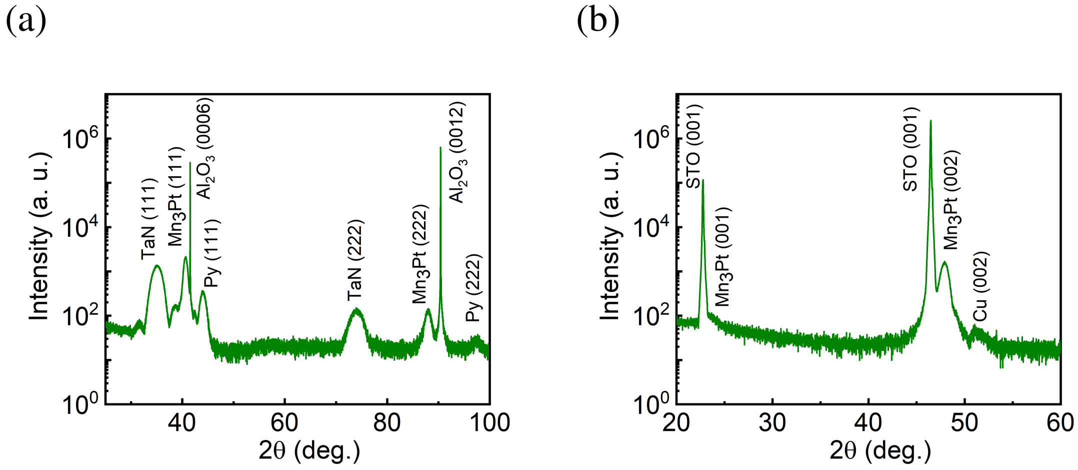

Figure 5.2: (a) Out of plane X-ray diffraction of $Mn_3Pt(111)/Cu/Py$, (b) $Mn_3Pt(001)/Cu/Py$ grown on TaN buffered $Al_2O_3(0001)$ and STO(001) substrates, respectively.

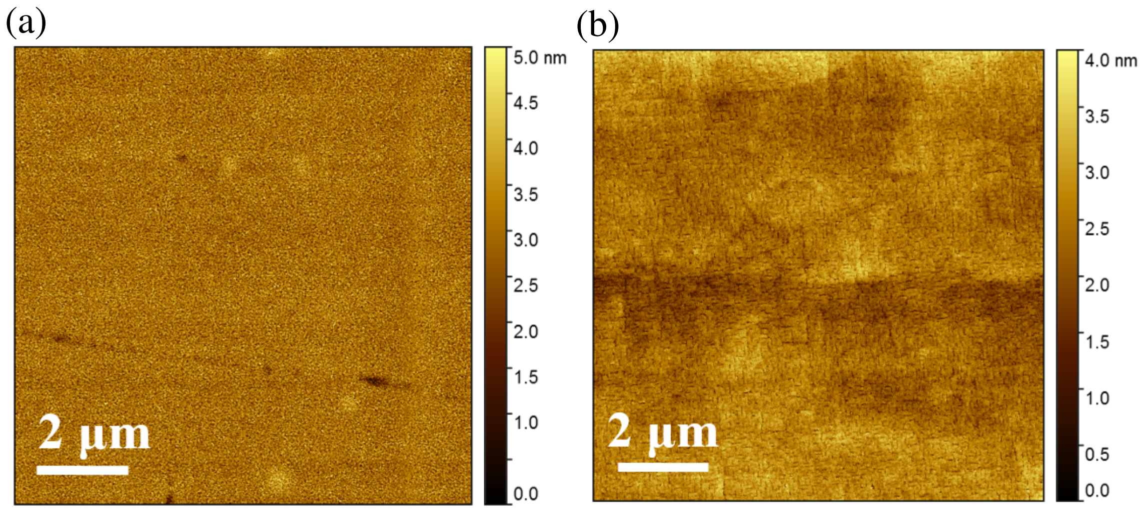

Figure 5.3: (a) AFM images of (a)$Mn_3Pt(111)/Cu/Py$ and (b)$Mn_3Pt(001)/Cu/Py$ thin films.

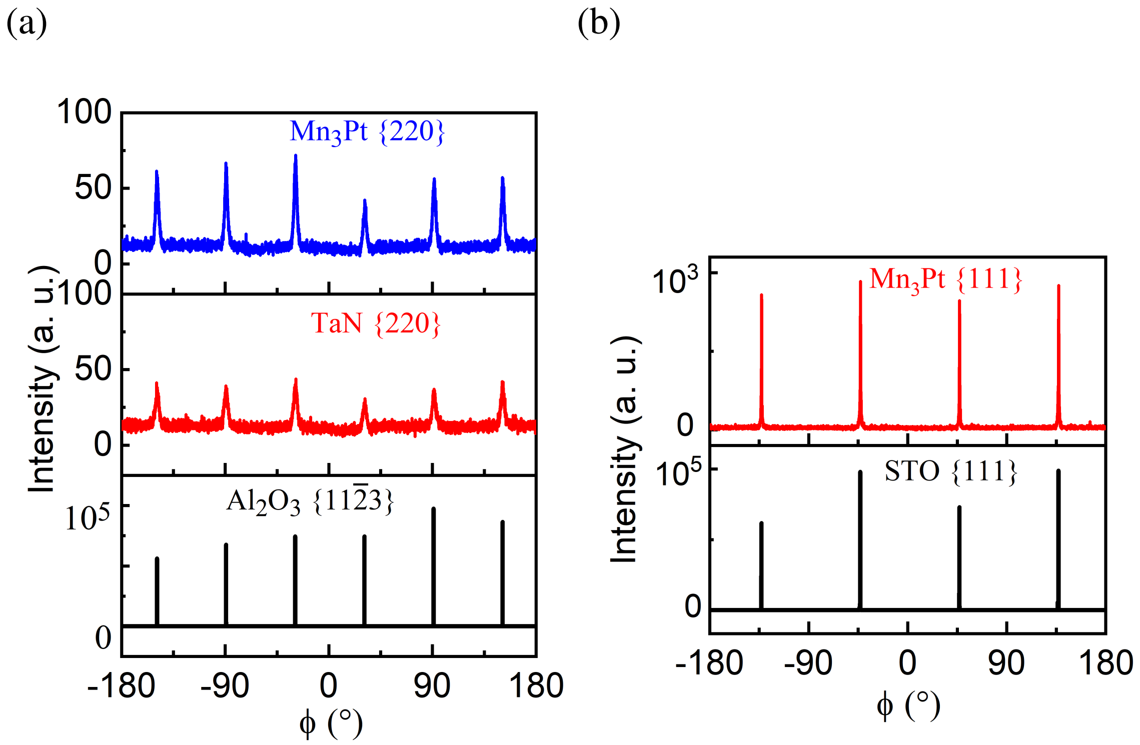

Figure 5.4: (a) Transverse ϕ scan of $Al_2O_3(11-23)$, TaN(220), $Mn_3Pt(220)$ reflections for $Mn_3Pt(001)$/Cu/Py and, (b) STO(111), $Mn_3Pt(111)$ reflections for $Mn_3Pt(111)$/Cu/Py structures, respectively.

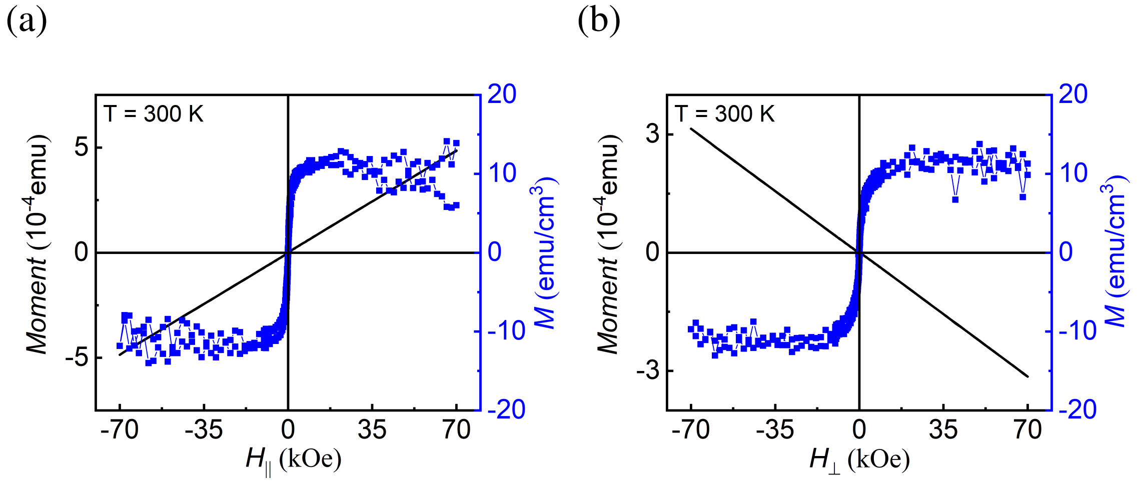

Figure 5.5: (a) Raw (black curve) and corrected (blue curve) M vs. $H_{||}$ for the 10 nm single layer $Mn_3Pt(111)$ film. (b) Raw (black curve) and corrected (blue curve) M vs. $H_{\perp}$ for the 10 nm single layer $Mn_3Pt(001)$ film

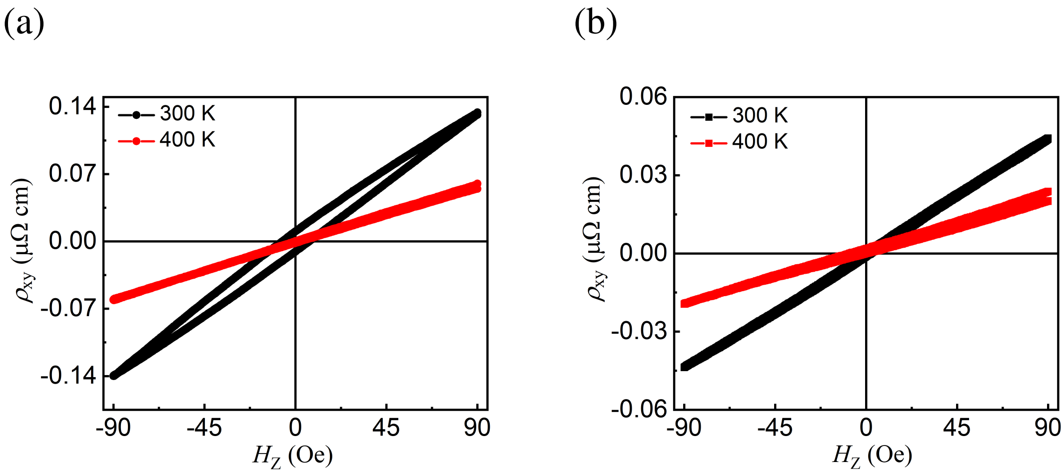

Figure 5.6: (a) Anomalous Hall resistivity of 10 nm $Mn_3Pt(001)$ film measured at 300 K and 400 K. (b) Anomalous Hall resistivity of 10 nm $Mn_3Pt(111)$ film measured at 300 K and 400 K.

The magnetization of 10 nm films for both the orientations is found to be less than 20emu/cm^3 (shown in Fig. 5.5). A small but finite AHE in 10 nm $Mn_3Pt(001)$ film confirms the non-collinear AFM state with T1 magnetic domain configuration and vanishing AHE at 400 K further verifies collinear AFM state which is usually observed beyond 365 K.

5.3 STFMR Measurement

Spin torque ferromagnetic resonance (ST-FMR) technique is used to determine the different spin orbit torques associated with this system. When an in-plane RF charge current (I_{RF}) is applied into the bilayer, spin accumulation occurs at the interface between the FM and the SOT materials and, produces an oscillatory anisotropic magneto resistance. This oscillatory anisotropic magneto resistance and I_{RF} produces a mixing ST-FMR DC voltage, V_{mix}, which is expressed as,

$$V_{mix} = V_0 \left[V_S \frac{\Delta H^2}{\Delta H^2 + (H_{ext} - H_{res})^2} + V_A \frac{\Delta H (H_{ext} - H_{res})}{\Delta H^2 + (H_{ext} - H_{res})^2} \right] \tag{5.1}$$

where $V_0, V_S, V_A, H_{res}, \Delta H$ and H_{ext} are constant prefactors, the amplitude of symmetric Lorentzian, the amplitude of antisymmetric Lorentzian, the resonance field, the linewidth and the external DC magnetic field, respectively. The schematic of STFMR is shown in

Chapter 4(Fig. 4.9).

To gain insights into the spin-orbit torque (SOT) phenomenon in these films, STFMR measurements were conducted on Mn_3Pt/Py and Mn_3Pt/Cu/Py films with both orientations of the Mn_3Pt layer. Figures 5.7, 5.8, 5.9, and 5.10 depict the STFMR spectra for $Mn_3Pt(111)(10)$/Py(5), $Mn_3Pt(001)(10)$/Py(5), $Mn_3Pt(111)(10)$/Cu(2)/Py(5), and $Mn_3Pt(001)(10)$/Cu(2)/Py(5), respectively. The value of Gilbert damping (α) and effective magnetization (M_{eff}) is calculated by using $\Delta H = \Delta H_0 + \frac{2\pi\alpha f}{\gamma}$ and Kittel relation $f = \frac{\mu\gamma}{2\pi}\sqrt{(H_{res}+H_K)(H_{res}+M_{eff}+H_K)}$, respectively. In these equations, the parameters have the following meanings as before: ΔH: Linewidth at given frequency, ΔH_0: Intrinsic Linewidth, α: Gilbert damping, f: Resonance frequency, γ: Gyromagnetic ratio, μ: material's magnetic permeability, H_{res}: Resonance field, H_K: In-plane anisotropy field and M_{eff}: Effective magnetization. The value of α and M_{eff} are summarized in the following text.

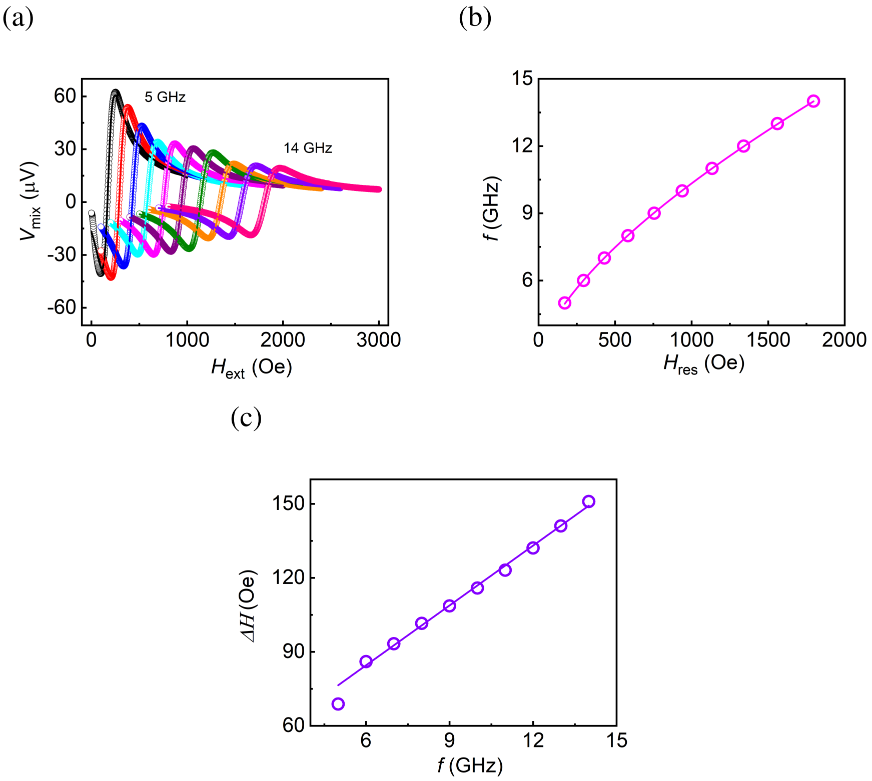
(a)

(b)

(c)

Figure 5.7: (a) STFMR spectra's for different frequencies (5 to 14 GHz), (b) f vs H_{res},(c) ΔH vs f of $Mn_3Pt(111)(10)$/Py(5) sample (All the thickness are in nm).

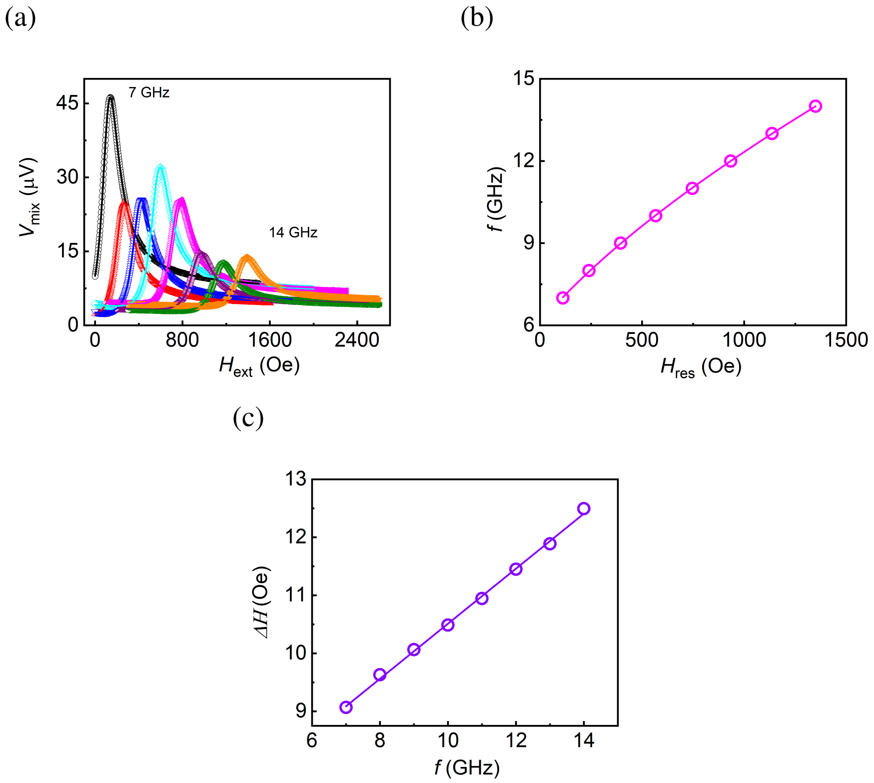

Figure 5.8: (a) STFMR spectra's for different frequencies (5 to 14 GHz), (b) f vs H_{res},(c) ΔH vs f of $Mn_3Pt(001)(10)/Py(5)$ sample (All the thickness are in nm).

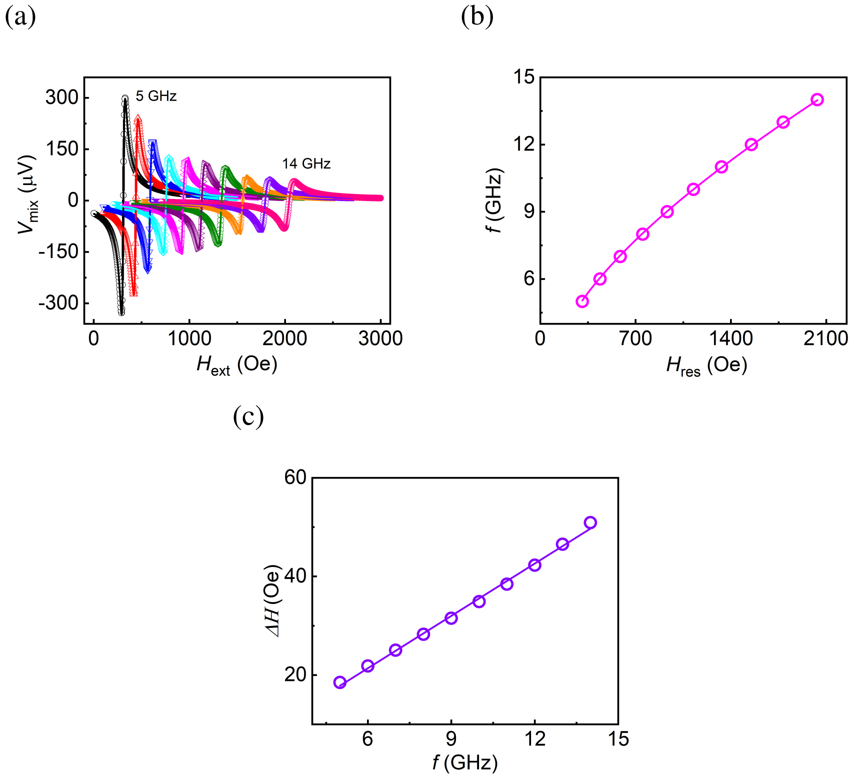

Figure 5.9: (a) STFMR spectra's for different frequencies (5 to 14 GHz), (b) f vs H_{res},(c) ΔH vs f of $Mn_3Pt(111)(10)/Cu(2)/Py(5)$ sample (All the thickness are in nm).

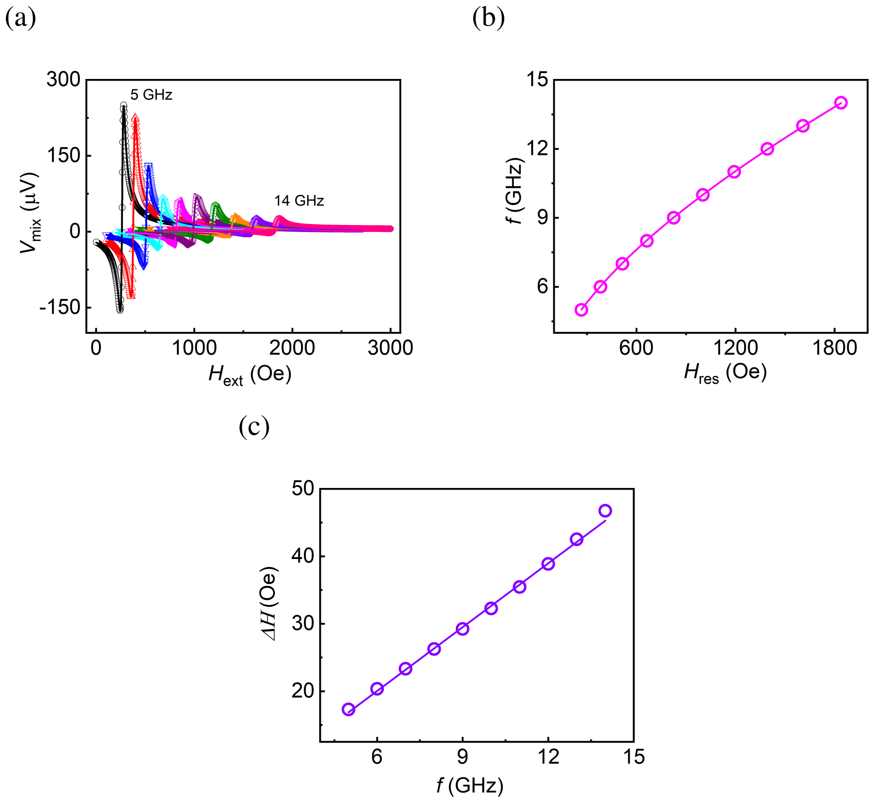

Figure 5.10: (a) STFMR spectra's for different frequencies (5 to 14 GHz), (b) f vs H_{res},(c) ΔH vs f of $Mn_3Pt(001)(10)/Cu(2)/Py(5)$ sample (All the thickness are in nm).

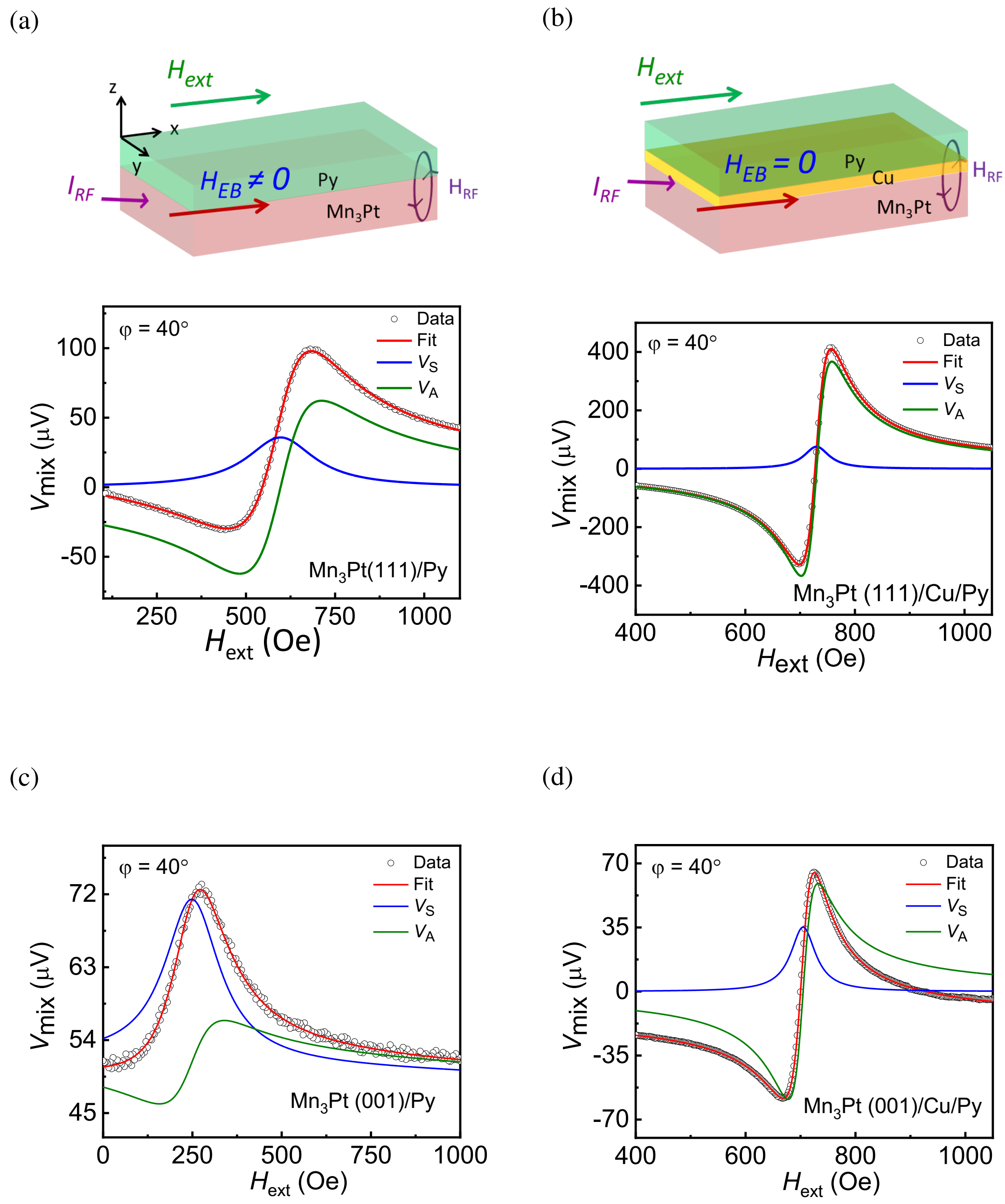

Figure 5.11: V_{mix} along with the fits and individual contributions of V_A and V_S are shown for (a) $Mn_3Pt(111)/Py$, (b) $Mn_3Pt(111)/Cu/Py$, (c) $Mn_3Pt(001)/Py$, and (d) $Mn_3Pt(001)/Cu/Py$ respectively. Pictorial representation of Mn_3Pt/Py and $Mn_3Pt/Cu/Py$, directions of H_{ext} and H_{EB} are shown on top of the panel.

V_{mix} were measured on the device of $Mn_3Pt(111)/Py$ and $Mn_3Pt(001)/Py$ bilayers for different frequencies at fixed, $\varphi = 40^\circ$, where φ is the angle between I_{RF} and external DC magnetic field. The V_{mix} is quite broad for both the bi-layers (Shown in Fig. 5.11a,c). The effective magnetization (M_{eff}) and Gilbert damping constant (α) are 895 (1027) emu/cm^3

and 0.023 (0.013) respectively for $Mn_3Pt(111)/Py$ ($Mn_3Pt(001)/Py$) bilayers. To investigate the origin of such broad V_{mix}, we insert 2 nm Cu layer in between Mn_3Pt and Py. The V_{mix} becomes sharper for both $Mn_3Pt(111)/Cu/Py$ and $Mn_3Pt(001)/Cu/Py$ tri-layers (Shown in Fig. 5.11b,d). M_{eff} and α are 812 (933) emu/cm^3 and 0.007 (0.006) respectively for $Mn_3Pt(111)/Cu/Py$ ($Mn_3Pt(001)/Cu/Py$) tri-layers. The H_{res} is found to be 0.06 (0.03T) for $Mn_3Pt(111)/Py$ ($Mn_3Pt(001)/Py$) whereas, $Mn_3Pt(111)/Cu/Py$($Mn_3Pt(001)/Cu/Py$) shows 0.08 (0.06T), respectively.

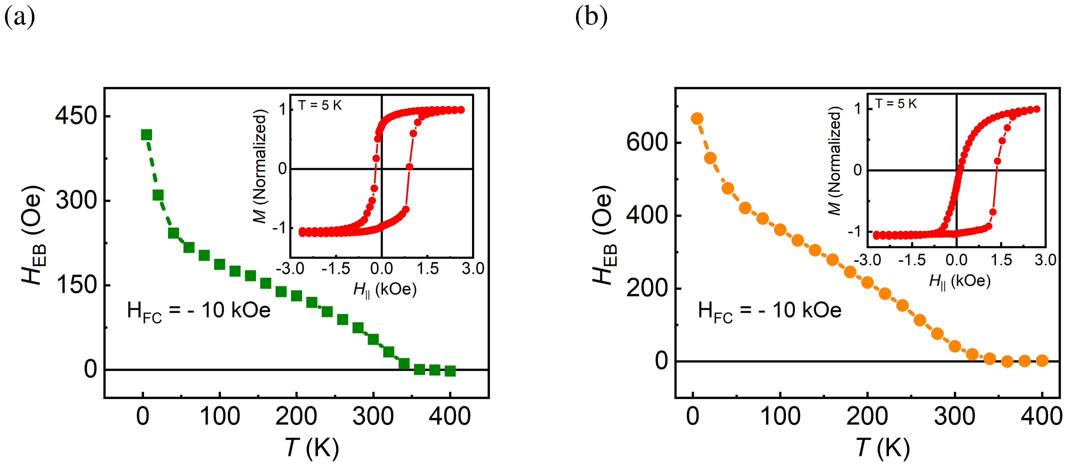

Figure 5.12: EB as a function of T for the (a) Mn3Pt(111)/Py and (b) Mn3Pt(001)/Py bilayers. Inset shows the magnetic hysteresis measured at 5 K and 300 K after field cooled at 10 kOe.

The comparatively smaller H_{res} indicate the presence of an additional field at the interface for $Mn_3Pt(111)/Py$ and $Mn_3Pt(001)/Py$. This additional field is the exchange bias (H_{EB}) field, which is finite at room temperature for both $Mn_3Pt(111)/Py$ and $Mn_3Pt(001)/Py$ (Shown in Fig. 5.12). To confirm this, detailed measurements of the exchange bias (EB) were performed between 5K to 400 K. The highest magnitude of the EB field was observed at 4 K, and as the temperature increased, the EB field gradually diminished until reaching the blocking temperature. For the Mn3Pt (111)/Py sample, the blocking temperature was determined to be 350 K, while for Mn3Pt (001)/Py, it was found to be 330 K. At these respective temperatures, the EB field effectively diminishes to zero (shown in Fig. 5.12). EB is not observed at 300 K when Cu is inserted between Mn_3Pt and Py as Cu breaks the exchange coupling between Mn_3Pt and Py. The absence of EB causes a shift of H_{res} to high magnetic field for $Mn_3Pt(111)$/Cu/Py and $Mn_3Pt(001)$/Cu/Py. The large damping and broad V_{mix} in $Mn_3Pt(111)$/Py and $Mn_3Pt(001)$/Py bilayers mainly originate due to the exchange coupling between Mn_3Pt and Py [108] [109].

5.4 Angular Dependence STFMR Measurement

To quantify the different torques (σ_x,σ_y and σ_z), a detailed angular dependence of V_{mix} has been performed on both the bi-layers and tri-layers. The amplitudes V_S and V_A in V_{mix} are proportional to the in-plane torque and out-of-plane torque arising from adjacent Mn_3Pt.

$$V_S(\varphi) = -A(\tau_{x,AD}\sin\varphi\sin2\varphi + \tau_{y,AD}\cos\varphi\sin2\varphi + \tau_{z,FL}\sin2\varphi) \tag{5.2}$$

$$V_A(\varphi) = A\sqrt{1+\frac{M_{eff}}{H_{ext}}}(\tau_{x,FL}\sin\varphi\sin2\varphi + \tau_{y,FL}\cos\varphi\sin2\varphi + \tau_{z,AD}\sin2\varphi) \tag{5.3}$$

Where $A = -\frac{I_{RF}}{2}\cdot\frac{1}{\alpha(2\mu_0 H_{res}+\mu_0 M_{eff})}$ is a constant. $\tau_{i,AD}$ and $\tau_{i,FL}$ represents the strength of the different torques(damping/anti-damping and field like) related to different polarization directions $\sigma_i(i = x, y, z)$, the spin polarization of the spin current along x,y,z, where x and y are the directions along and transverse to the current, respectively and z is the normal to the plane of the device.

$V_A(\varphi)$ can be described with out-of-plane field like torque ($\tau_{y,FL}$ and $\tau_{x,FL}$) due to σ_y and σ_x respectively (second and first term in equation 5.3) and small out of plane damping/antidamping torque $\tau_{z,AD}$ due to σ_z. Whereas, $V_S(\varphi)$ reveals in-plane anti-damping like torque ($\tau_{y,AD}$ and $\tau_{x,AD}$) originating from σ_y and σ_x respectively (second and first term in equation 5.2) and small in-plane field like torque $\tau_{z,FL}$ due to σ_z. V_S and V_A contributions at different φ are extracted from V_{mix} using the equation 5.1.

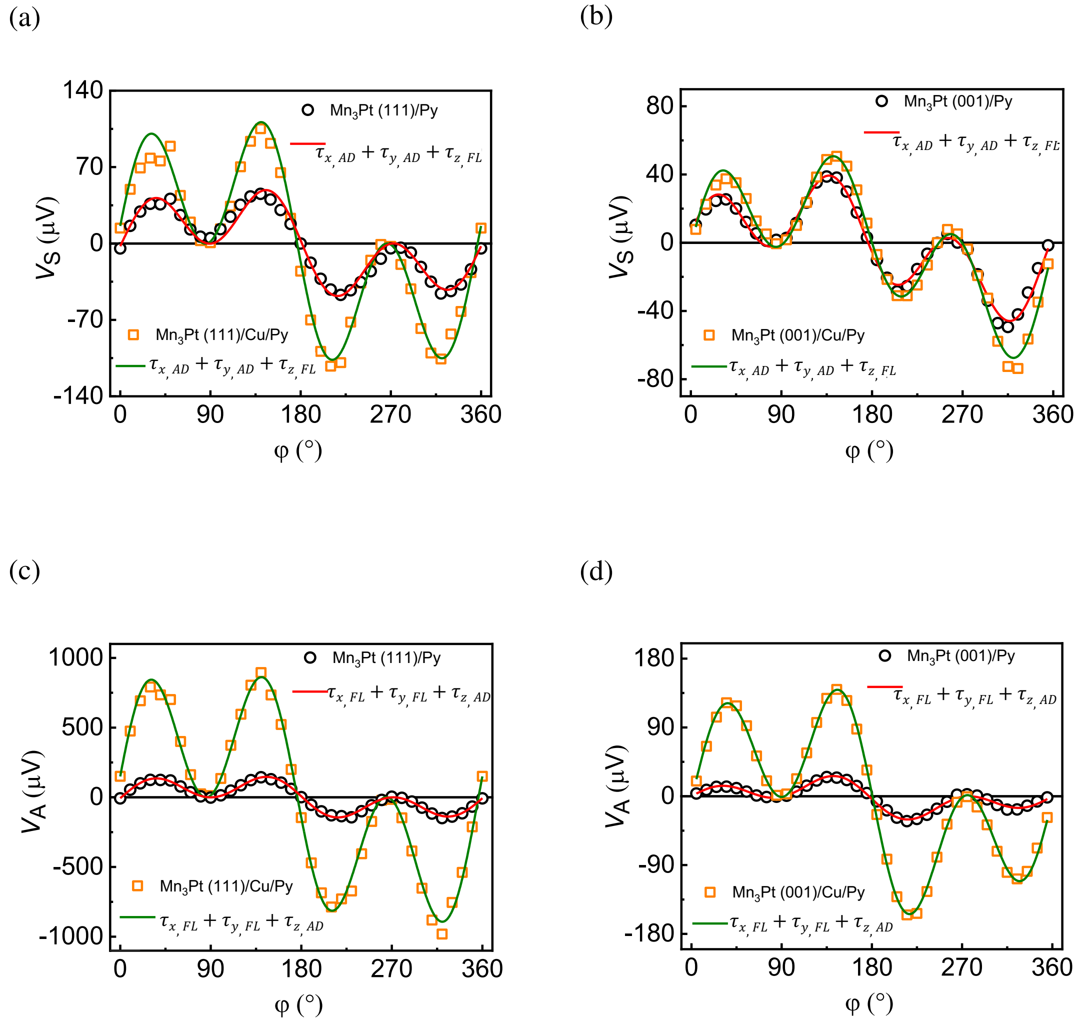

Figure 5.13: V_S and V_A as a function of φ (Angle between I_{RF} and H_{ext}) for (a) $Mn_3Pt(111)/Py$, (b) $Mn_3Pt(111)/Cu/Py$, (c) $Mn_3Pt(001)/Py$ and (d) $Mn_3Pt(001)/Cu/Py$ structures, respectively.

Fig. 5.13a,b,c,d shows the angular dependence of $V_S(\varphi)$ and $V_A(\varphi)$ for $Mn_3Pt(111)/Py$ and $Mn_3Pt(001)/Py$ samples with and without Cu, respectively. The variations of $V_A(\varphi)$ and $V_S(\varphi)$ with respect to the angle φ in both (001) and (111) orientations of Mn_3Pt (with and without Cu) demonstrate the presence of all damping/anti damping and field like torques resulting from spin polarization σ_x, σ_y, and σ_z, respectively. However, the magnitudes of these torques vary among different samples, as indicated by the differences in the magnitudes of $V_A(\varphi)$ and $V_S(\varphi)$, as shown in Figure 5.13. Notably, the samples without an exchange bias (with Cu layer) exhibit larger values of $V_A(\varphi)$ and $V_S(\varphi)$, while the samples with an exchange bias (without Cu) display smaller values. It is important to point out that $Mn_3Pt(001)/Py$ shows highly asymmetrical angular dependence of V_A and V_S compare to $Mn_3Pt(111)/Py$.

(a)

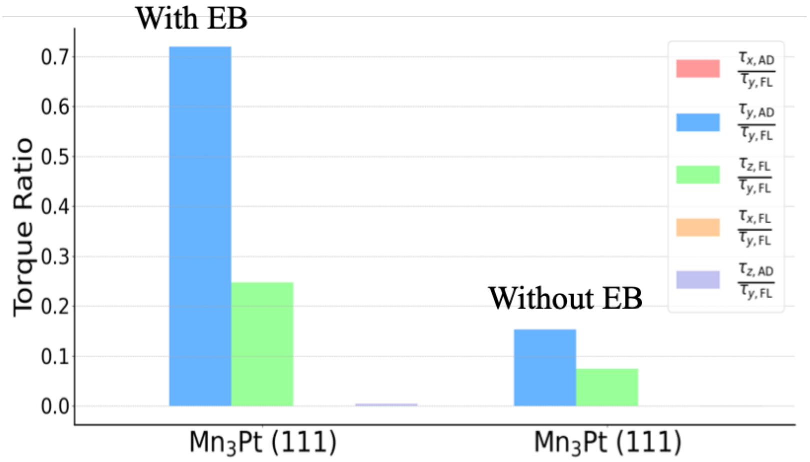

(b)

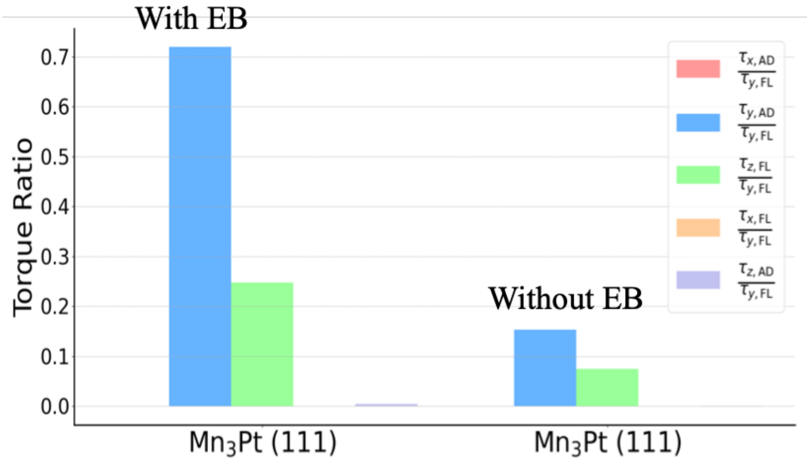

Figure 5.14: Histogram of normalized torques for (a) $Mn_3Pt(111)/Py$ (with EB) and $Mn_3Pt(111)/Cu/Py$ (without EB), (b) for $Mn_3Pt(001)/Py$ (with EB) and Mn3Pt(001)/Cu/Py (without EB), respectively.

Figure 5.14 presents histograms depicting the normalized differences in torques with respect to $\tau_{y,FL}$. In the case of the $Mn_3Pt(111)/Py$ configuration, both the ratios $\tau_{y,AD}/\tau_{y,FL}$ and $\tau_{z,FL}/\tau_{y,FL}$ exhibit large values. Conversely, these ratios are small for the $Mn_3Pt(111)/Cu/Py$ configuration. For the $Mn_3Pt(001)/Py$ and $Mn_3Pt(001)/Cu/Py$ configurations, similar torques are observed. However, the presence of exchange bias (EB) significantly impacts not only the magnitude of the torques but also leads to erroneous estimations of various torques. For instance, the ratio $\tau_{y,AD}/\tau_{y,FL}$ reaches approximately 3, which is physically implausible. The magnitudes of all the torques decrease substantially and become physically acceptable when a layer of Cu is inserted between Mn_3Pt and Py. It is noteworthy that the ratio $\tau_{y,AD}/\tau_{y,FL}$ is considerably higher for $Mn_3Pt(001)$ compared to $Mn_3Pt(111)$.The angular dependence of the spin-torque ferromagnetic resonance (STFMR) measurement reveals that both orientations of $Mn_3Pt(111)$/Py and $Mn_3Pt(001)$/Py exhibit all three torques (σ_x,σ_y and σ_z). Furthermore, the magnitudes of these torques are influenced by the presence of exchange bias at the interface between Mn_3Pt and Py.

5.5 Current Induced Magnetization Switching

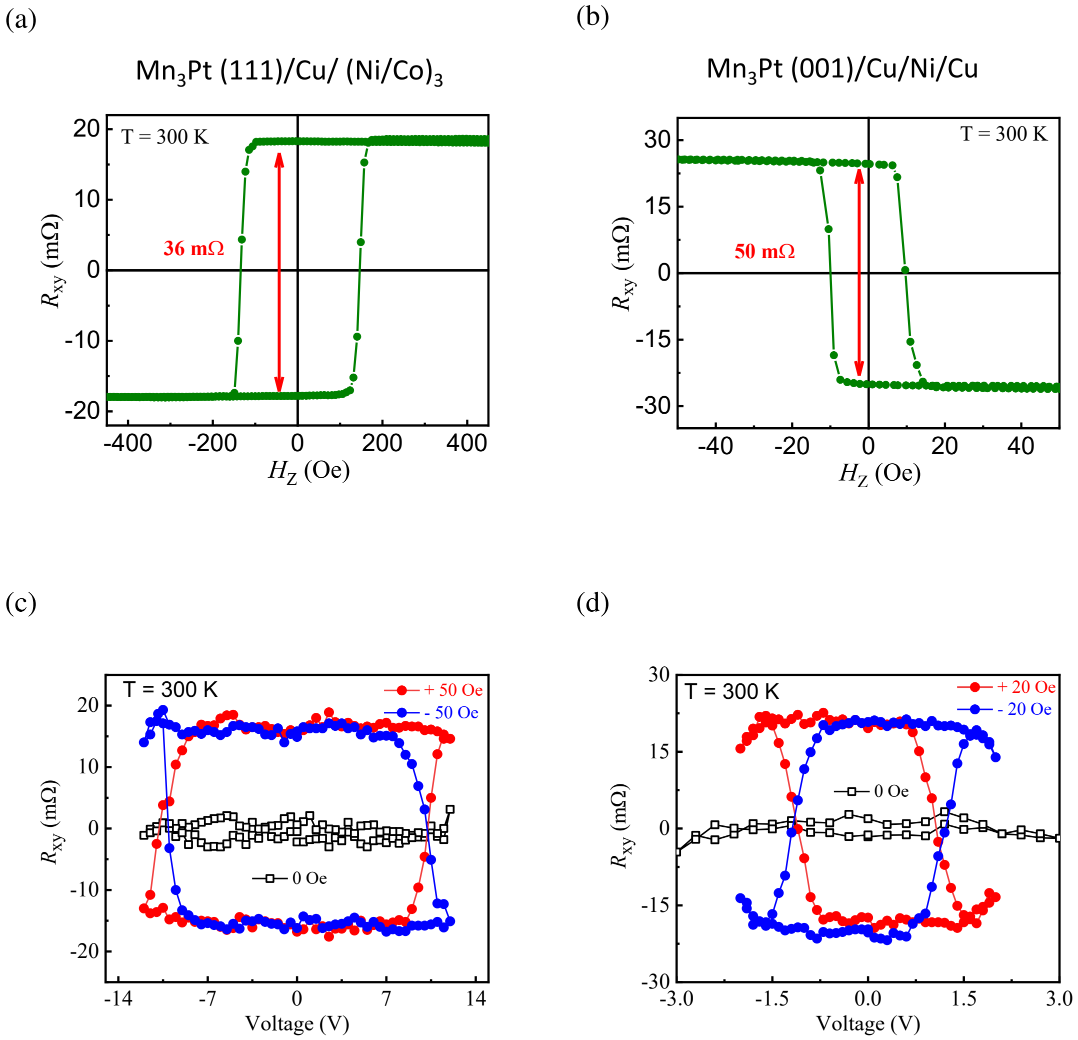

Figure 5.15: Anomalous Hall Resistance (AHR) of (a) Mn_3Pt(111)/Cu/(Ni/Co)$_3$ and (c) Mn_3Pt (001)/Cu/Ni/Cu structures. Current induced magnetization switching in presence of small H_x and in the absence of H_x are shown for (b) Mn_3Pt(111)/Cu/(Ni/Co)$_3$ and (d) Mn_3Pt(001)/Cu/Ni/Cu structures.

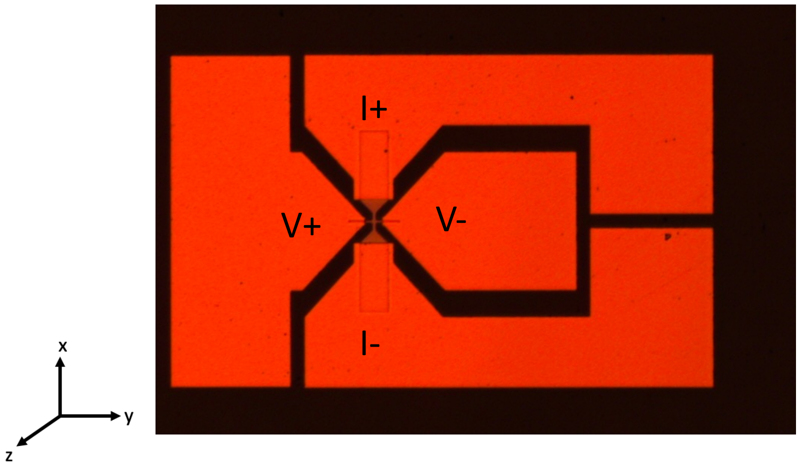

Figure 5.16: Optical micrograph of Hall bar device. V+(V-), I+(I-) represents the polarity of the measured voltage and applied current.

To investigate the capability of the observed Spin-Orbit Torques (SOTs) to reliably switch a perpendicularly magnetized layer, two distinct sample configurations were prepared: Mn$_3$Pt(111)/Cu/(Ni/Co)$_3$ and Mn$_3$Pt(001)/Cu/Ni/Cu. The choice of (Ni/Co)$_3$ was motivated by its growth orientation along (111) and its well-established perpendicular magnetic anisotropy (PMA). Conversely, in the second configuration, no significant PMA was observed in these layers, leading to the growth of a Cu/Ni/Cu structure with an orientation along (001) that exhibited PMA.

Hysteresis loops of the Anomalous Hall Resistance (AHR) as a function of out-of-plane magnetic field (H$_Z$) are depicted in Figure 5.15a and b, clearly demonstrating the presence of PMA in both cases. Notably, the AHR originating from the Mn$_3$Pt layer is quite small, as determined from measurements conducted on individual Mn$_3$Pt(001) and Mn$_3$Pt(111) layers (see Fig. 5.6).To assess the effectiveness of current-induced electrical switching, we have performed experiments on both samples using a 100 ms writing pulse and a 1 mA DC read current (I), without the application of any in plane bias field (H$_X$) (device structure shown in Fig. 5.16). In the absence of H$_X$, no magnetization switching was observed in either structure. However, Mn$_3$Pt(111)/Cu/(Ni/Co)$_3$ exhibited nearly complete (90%) magnetization switching when a bias field of H$_X$ = ±50 Oe was applied (Fig. 5.15c). The degree of switching decreased for smaller or larger values of H$_X$. On the other hand, Mn$_3$Pt(111)/Cu/(Ni/Co)$_3$ demonstrated a lower degree of switching (82%) at H$_X$ = ±20

Oe (shown in Fig. 5.15d). It is worth noting that although previous STFMR results on related structures indicated finite values of $\tau_{z,AD}/\tau_{y,FL}$ that should result in switching in the absence of any bias field, no such switching was observed in our experiments. This suggests that these torques are relatively small in magnitude.

5.6 Conclusion and Summary

In conclusion, we demonstrate that the presence of exchange bias in non-collinear AFM/FM bilayers significantly enhances the magnitude of spin orbit torques. The substantial value of Gilbert damping α in AFM/FM bilayers primarily stems from the finite exchange coupling between Mn_3Pt and Py, resulting in a broad V_{mix} signal. We observe spin currents with all three polarizations, σ_x, σ_y, and σ_z, in both $Mn_3Pt(111)$/Py and $Mn_3Pt(001)$/Py configurations, as well as in similar structures with Cu interface layers. Notably, the Spin Hall Effect (SHE) attributed to σ_y ($\tau_{y,AD}/\tau_{y,FL}$) is considerably larger for $Mn_3Pt(001)$ compared to $Mn_3Pt(111)$, regardless of the presence of Cu layers. Despite the presence of a $\tau_{z,AD}$ torque indicated by our STFMR measurements, its magnitude is insufficient to enable field-free magnetization switching in related structures with perpendicularly magnetized ferromagnetic layers. This study underscores the significance of exchange bias in assessing spin-orbit torques in non-collinear AFM/FM systems. The summarized parameters related to spin-orbit torques (SOT) for these films are presented in table 5.1. Additionally, the effect of exchange bias on ferromagnetic resonance (FMR) parameters is illustrated through bar plots shown in Figure 5.17.

Sample	M_{eff} (emu/cc)	H_{res}(T)	α	$\tau_{x,AD}/\tau_{y,FL}$	$\tau_{y,AD}/\tau_{y,FL}$	$\tau_{z,FL}/\tau_{y,FL}$	$\tau_{x,FL}/\tau_{y,FL}$	$\tau_{z,AD}/\tau_{y,FL}$
$Mn_3Pt(111)(10)$/Py	895	0.059	0.023	0	0.720	0.248	0	0.005
$Mn_3Pt(111)(10)$/Cu(2)/Py	812	0.073	0.007	0	0.153	0.075	0	-0.001
$Mn_3Pt(001)(10)$/Py	1027	0.023	0.013	-1.064	3.136	0.195	0.049	-0.332
$Mn_3Pt(001)(10)$/Cu(2)/Py	933	0.063	0.006	-0.182	0.539	0.066	0.068	-0.095

Table 5.1: Summary of the SOT extracted parameters of $Mn_3Pt(001)$, $Mn_3Pt(111)$ films from STFMR Measurement (All the thickness in nm).

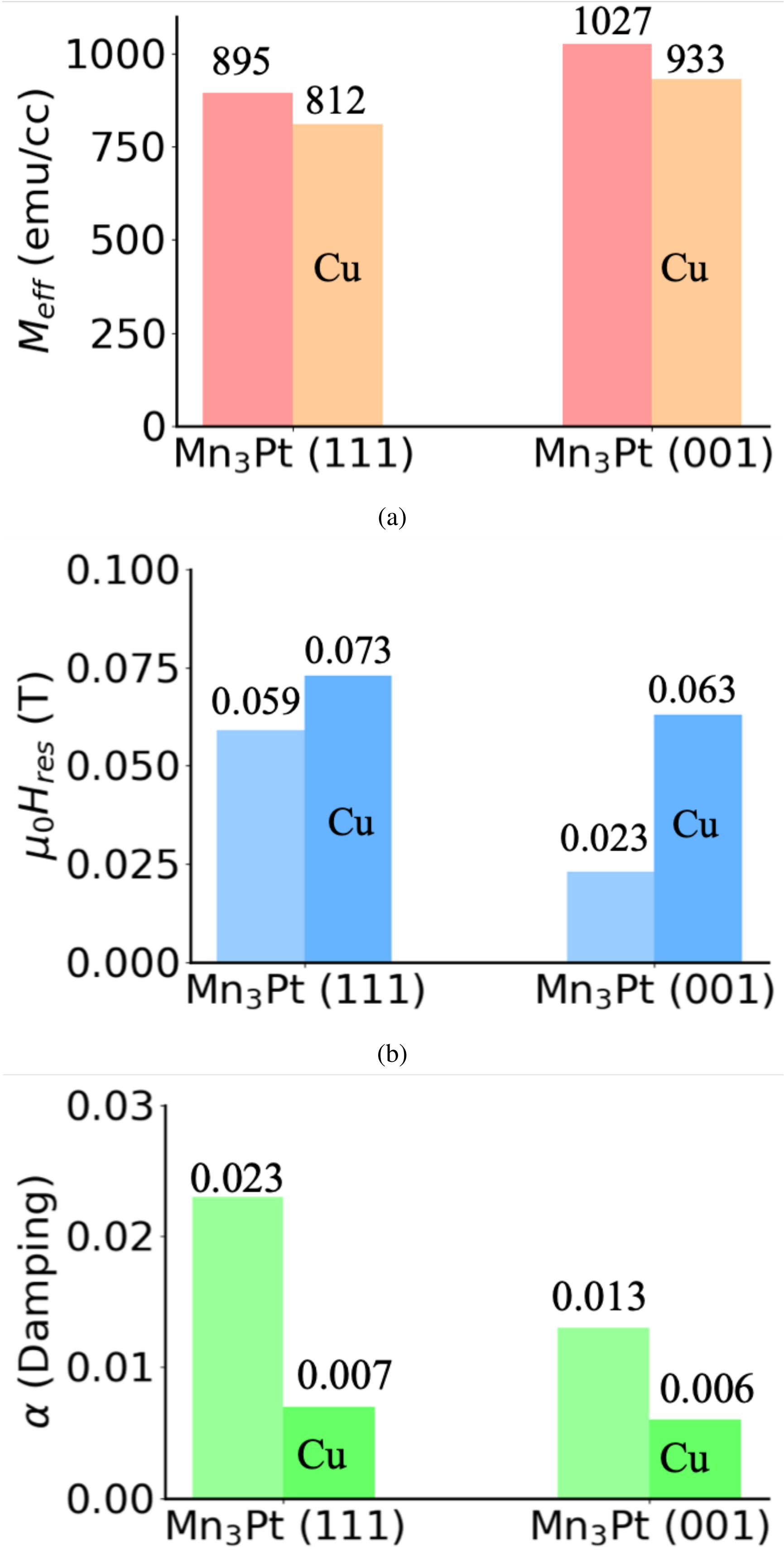

(a)

(b)

(c)

Figure 5.17: Effect of exchange bias (with Cu indicating no exchange bias) on parameters : (a) effective magnetization M_{eff}, (b) resonance field $\mu_0 H_{res}$, and (c) damping α in $Mn_3Pt(111)$ and $Mn_3Pt(001)$, respectively.

6

Conclusion and Outlook

In summary, this thesis presents the study of the crystallographic dependence of SHE in two different class of materials, namely heavy metal Pt and non collinear AFM Mn_3Pt.

SHE is very well known in Pt and various technique has been employed to study the effect. However, a direct comparison of optical and electrical methods has not been yet explored. In this study, we have utilized magneto optical Kerr effect (MOKE) to build an optical technique called OFMR that resemble STFMR however with a key difference of detection. We have used this OFMR technique to measure the SHE in Pt in three crystallographic directions Pt(111), Pt(110) and Pt(001) respectively. From the comparison of SHE measurement, we have concluded that when the FMR width is large and the signal is low, it's difficult to estimate the value of θ_{SH} using DC bias method, especially in the case of STFMR. This can be clearly seen in Pt(110) sample, where STFMR measurement results in erroneous value of θ_{SH} due to electrical artifacts. However, due to high sensitivity (pron to fewer artifacts) of OFMR measurement, it results close to realistic value of θ_{SH} for Pt (110). For other two samples, Pt(111) and Pt(001) respectively, we got agreeable values of θ_{SH} from both OFMR and STFMR measurement. Overall, both the measurement showed, 20-30% changes in θ_{SH} values with respect to crystallographic directions (from Pt(111) to Pt(001)). The other spin Hall parameter such as intrinsic spin Hall angle ($\theta_{SH-intrinsic}$), field like torque efficiency (τ_{FL}) were also found consistent for Pt(111) and Pt(001) from both the measurement.

Second important part of the thesis focus on the characterization of SOT in cubic Mn_3Pt with respect to the crystallographic directions (001) and (111). It has been theoretically predicted that non-collinear AFM posses large SHE due to its large Berry curvature. Due to high crystal and magnetic symmetry of Mn_3Pt, we have studied the effect of crystallographic orientation on spin polarization (σ_x,σ_y and σ_z). To measure these spin polarization or torques, angular dependence of STFMR measurement is carried out. We have concluded that exchange bias plays a crucial role to characterize the SOT and in order to rule out the effect of exchange bias, a thin (2 nm) Cu layer is inserted between Mn_3Pt/Py. To further support the evidence of facet dependent unconventional torques coming from Mn_3Pt, field dependent current induced magnetization switching is carried out.

The SHE has been investigated for Pt and Mn_3Pt films in this thesis. Following could be a potential outlook for future scientific work.

- One of the next steps would be to study the SHE with respect to film thickness and temperature. For temperature dependent OFMR measurement, a suitable optical cryostat would indeed be needed. Additionally, a rotating magnetic field dependence measurement would also be beneficial to study the effect of anisotropy on SHE (as shown in fig. 6.1).

- Studying the SHE in other non-collinear AFMs: The thesis has investigated the SHE in Mn_3Pt as an example of a non-collinear AFM with strong SHE, but there are other non-collinear AFMs that could exhibit interesting SHE properties as well. For example, Mn_3Sn and Mn_3Ge have recently been shown to have large SHE signals.

Investigating the SHE in these materials could provide further understanding of the effect and could also lead to the discovery of new materials with promising SHE properties.

- Exploring the relationship between crystal structure and SHE: The thesis has investigated the crystallographic dependence of the SHE, but there may be other structural factors that influence the effect as well. For example, defects, strain, and interface effects could all play a role in the SHE. Investigating these factors could provide a more complete understanding of the effect and could also lead to the development of new materials and devices with enhanced SHE properties.
- Developing new techniques for measuring the SHE: The thesis likely used a variety of techniques to measure the SHE, but there may be new techniques that could provide additional insights into the effect. For example, time-resolved measurements or pump-probe measurements could help to reveal the underlying physics of the SHE. Developing new techniques could also help to improve the accuracy and reproducibility of measurements, which is important for developing new materials and devices.

Overall, the thesis has provided a good foundation for understanding the crystallographic dependence of the SHE in Pt and Mn_3Pt, but there are many directions for future research.

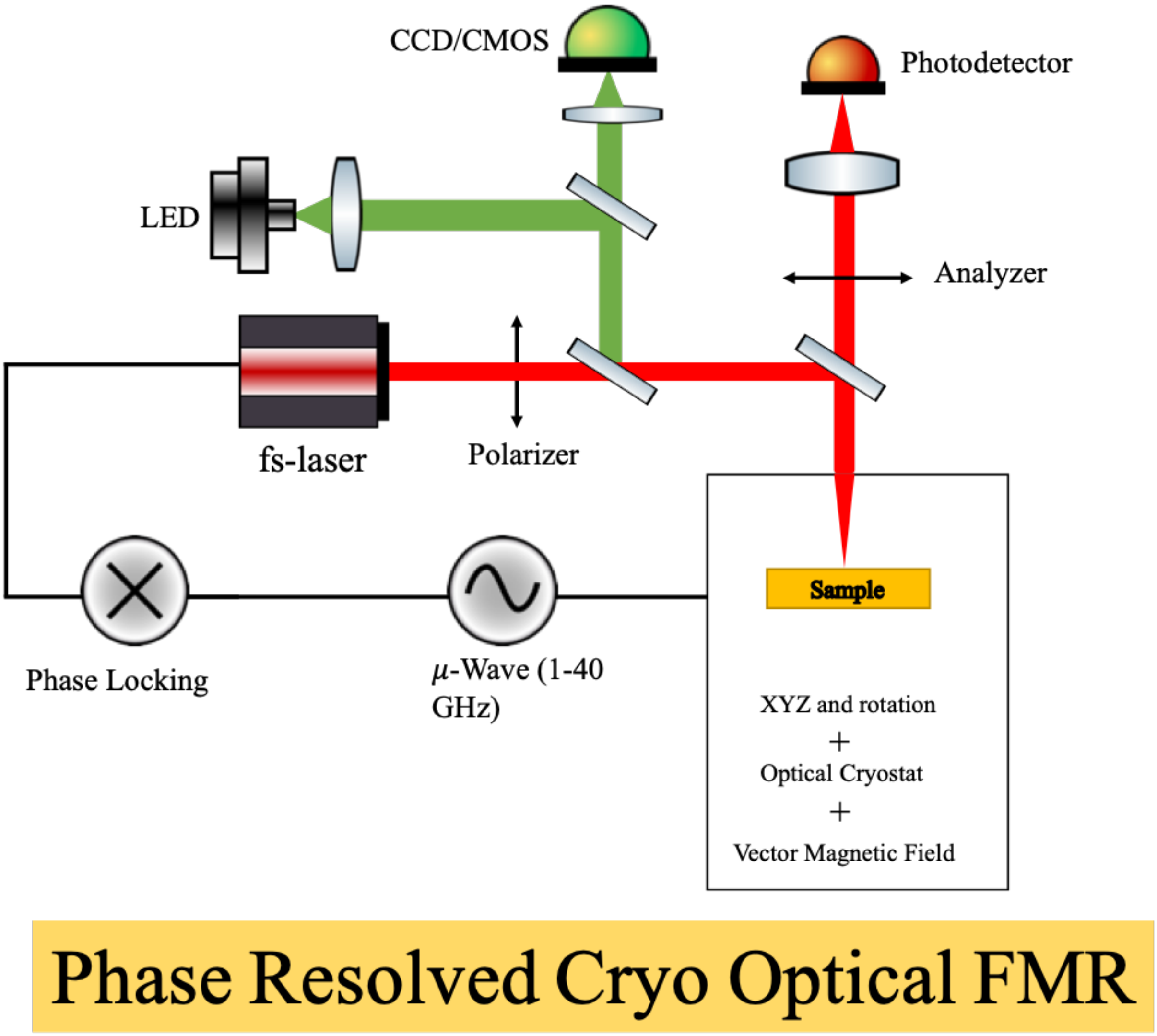

Figure 6.1: Proposed schematic of the Cryo-OFMR setup, where a vector magnetic field can be applied in any given 2D plane (complete circle) or 3D space (complete sphere) at a cryogenic temperature of 4K.

A

Appendix

List of Abbreviations

SHE	Spin Hall Effect
ISHE	Inverse Spin Hall Effect
AHE	Anomalous Hall Effect
MTJ	Magnetic Tunnel Junction
RM	Race Track Memory
GMR	Giant Magneto Resistance
TMR	Tunnel Magneto Resistance
MRAM	Magnetic Random Access Memory
CMOS	Complementary Metal-Oxide Semiconductor
SOC	Spin Orbit Coupling
STT	Spin Transfer Torque
SOT	Spin Orbit Torque
DW	Domain Wall
FM	Ferromagnetic Material
HM	Heavy Metal
DMI	Dzyaloshinskii–Moriya Interaction
ST-FMR	Spin Torque Ferromagnetic Resonance
OFMR	Optically Detected Ferromagnetic Resonance
AFM	Antiferromagnetic
XRD	X-Ray Diffraction
AFM	Atomic Force Microscopy
PPMS	Physical Properties Measurement System
SQUID	Superconducting Quantum Interference Device
VSM	Vibrating Sample Magnetometer
MOKE	Magneto Optical Kerr Effect
LASER	Light Amplification by Stimulated Emission of Radiation
SHA	Spin Hall Angle

BHARAT GROVER

EDUCATION

Doctor of Philosophy in Physics, Ph.D. | Spintronics and Optics Jan. 2017 - April 2022
Max Planck Institute of Microstructure Physics, Halle Halle, Germany

Masters in Material Science Technology | M.Tech. (8.025/10) June. 2013 – May 2015
Indian Institute of Technology, Delhi Delhi, India

Master of Science | M.Sc. (8.3/10) Aug. 2011 – May 2013
University of Rajasthan, Jaipur Rajasthan, India

Bachelor of Science | B.Sc. (9.0/10) Aug. 2008 – May 2011
University of Rajasthan, Jaipur Rajasthan, India

SKILLS

Languages : English (Professional efficiency), Hindi (Native), and German (B1 level).

Computer Programming and Skills : LabVIEW, Python, (Ray Optics module)COMSOL, Opticstudio(ZEMAX),Origin and Autodesk Inventor.

Document Creation : Microsoft Office and LaTex.

Laboratory Skills : Instrumentation, Electronics, Optics and Microwave etc.

RESEARCH ACHIEVEMENTS

Doping-induced spin Hall ratio enhancement in A15-phase, Ta-doped -W thin films. April 2020
J. Phys. Mater. 2020, 3, 044001

Spin Hall effect in non-collinear antiferromagnets. August 2019
Joint European Magnetic Symposia, Upsala, Sweden

Measurement of spin currents: Comparison of optical and electrical methods. March 2021
APS March Meeting 2021

Crystallographic dependence of the spin Hall angle in epitaxial Pt films. April 2022
Appl. Phys. Lett. 2022, 172406 (**Featured Article**)

Generation of out-of-plane polarized spin current by spin swapping July 2023
Nature Communications, 2023, 14, 1120

HONORS AND AWARDS

CSIR NET Fellowship - 2013
NET (National Eligibility Test) is the award to get one of the prestigious research fellowships in Indian research institutes.

GATE MHRD Fellowship - 2013, 2014
GATE is the entrance exam for post-graduation admission to the Indian Institute of Technology (IITs).

References

[1] Stuart S. P. Parkin, Masamitsu Hayashi, and Luc Thomas. Magnetic Domain-Wall Racetrack Memory. *Science*, 320(5873):190–194, 4 2008.

[2] Jun Ichiro Inoue. GMR, TMR, BMR, and Related Phenomena. *Nanomagnetism and Spintronics: Second Edition*, pages 15–106, 1 2014.

[3] Bernard Dieny and I Lucian Prejbeanu. Magnetic Random-Access Memory. In *Introduction to Magnetic Random-Access Memory*, chapter 5, pages 101–164. John Wiley & Sons, Ltd, 2017.

[4] Jairo Sinova, Sergio O. Valenzuela, J. Wunderlich, C.H. Back, and T. Jungwirth. Spin Hall effects. *Reviews of Modern Physics*, 87(4):1213, 10 2015.

[5] Jairo Sinova, Dimitrie Culcer, Q Niu, N A Sinitsyn, T Jungwirth, and A H Macdonald. Universal Intrinsic Spin Hall Effect. *Phys. Rev. Lett*, 92(12):126603, 2004.

[6] Jakub Železný, Yang Zhang, Claudia Felser, and Binghai Yan. Spin-Polarized Current in Noncollinear Antiferromagnets. *Physical Review Letters*, 119(18):187204, 11 2017.

[7] Yang Zhang, Jakub Železný, Yan Sun, Jeroen Van Den Brink, and Binghai Yan. Spin Hall effect emerging from a noncollinear magnetic lattice without spin–orbit coupling. *New Journal of Physics*, 20(7):073028, 7 2018.

[8] Y. Taguchi, Y. Oohara, H. Yoshizawa, N. Nagaosa, and Y. Tokura. Spin chirality, berry phase, and anomalous hall effect in a frustrated ferromagnet. *Science*, 291(5513):2573–2576, 3 2001.

[9] Yang Zhang, Yan Sun, Hao Yang, Jakub Železný, Stuart P.P. Parkin, Claudia Felser, and Binghai Yan. Strong anisotropic anomalous Hall effect and spin Hall effect in the chiral antiferromagnetic compounds Mn3X (X=Ge, Sn, Ga, Ir, Rh, and Pt). *Physical Review B*, 95(7):075128, 2 2017.

[10] Donald M. Mattox. Physical Sputtering and Sputter Deposition (Sputtering). *Handbook of Physical Vapor Deposition (PVD) Processing*, pages 237–286, 1 2010.

[11] G. A Jeffery. Elements of x-ray diffraction (Cullity, B. D.). *Journal of Chemical Education*, 34(4):A178, 4 1957.

[12] Nader Jalili and Karthik Laxminarayana. A review of atomic force microscopy imaging systems: application to molecular metrology and biological sciences. *Mechatronics*, 14(8):907–945, 10 2004.

[13] Daniel Bothner, Ines Corveira Rodrigues, Jasper Franse, and Gary Steele. TN2513-P SQUID Practicum Manual.

[14] R. L. Fagaly. Superconducting quantum interference device instruments and applications. *Review of Scientific Instruments*, 77(10):101101, 10 2006.

[15] Physical Property Measurement System ® DynaCool TM User's Manual.

[16] Masato Yamashita, Toshifumi Nishii, and Hiroya Mizutani. Resistivity measurement by dual-configuration four-probe method. *Japanese Journal of Applied Physics, Part 1: Regular Papers and Short Notes and Review Papers*, 42(2 A):695–699, 2 2003.

[17] Jitendra P. Singh, Richa Bhardwaj, Aditya Sharma, Baljeet Kaur, Sung O. Won, Sanjeev Gautam, and Keun Hwa Chae. Fabrication of Magnetic Tunnel Junctions. *Advanced Applications in Manufacturing Engineering*, pages 53–77, 1 2019.

[18] Atsufumi Hirohata, Keisuke Yamada, Yoshinobu Nakatani, Lucian Prejbeanu, Bernard Diény, Philipp Pirro, and Burkard Hillebrands. Review on spintronics: Principles and device applications. *Journal of Magnetism and Magnetic Materials*, 509:166711, 9 2020.

[19] Robin Blasing, Asif Ali Khan, Panagiotis Ch Filippou, Chirag Garg, Fazal Hameed, Jeronimo Castrillon, and Stuart S.P. Parkin. Magnetic Racetrack Memory: From Physics to the Cusp of Applications within a Decade. *Proceedings of the IEEE*, 108(8):1303–1321, 8 2020.

[20] Weifeng Zhang, Wei Han, See Hun Yang, Yan Sun, Yang Zhang, Binghai Yan, and Stuart S.P. Parkin. Giant facet-dependent spin-orbit torque and spin Hall conductivity in the triangular antiferromagnet IrMn3. *Science Advances*, 2(9), 2016.

[21] Luqiao Liu, R. A. Buhrman, and D. C. Ralph. Review and Analysis of Measurements of the Spin Hall Effect in Platinum. *arXiv preprint arXiv:1111.3702*, 11 2011.

[22] Luqiao Liu, Takahiro Moriyama, D. C. Ralph, and R. A. Buhrman. Spin-torque ferromagnetic resonance induced by the spin Hall effect. *Physical Review Letters*, 106(3):1–4, 2011.

[23] IAN M. ROSS. The Invention of the Transistor. *Proceedings of the IEEE*, 86(1):7–28, 1998.

[24] https://www.intel.com/content/www/us/en/history/virtual-vault/articles/moores-law.html, 2023.

[25] Atsufumi Hirohata, Keisuke Yamada, Yoshinobu Nakatani, Lucian Prejbeanu, Bernard Diény, Philipp Pirro, and Burkard Hillebrands. Review on spintronics: Principles and device applications. *Journal of Magnetism and Magnetic Materials*, 509:166711, 9 2020.

[26] M. N. Baibich, J. M. Broto, A. Fert, F. Nguyen Van Dau, F. Petroff, P. Eitenne, G. Creuzet, A. Friederich, and J. Chazelas. Giant magnetoresistance of (001)Fe/(001)Cr magnetic superlattices. *Physical Review Letters*, 61(21):2472–2475, 11 1988.

[27] G. Binasch, P. Grünberg, F. Saurenbach, and W. Zinn. Enhanced magnetoresistance in layered magnetic structures with antiferromagnetic interlayer exchange. *Physical Review B*, 39(7):4828, 3 1989.

[28] S. S.P. Parkin, N. More, and K. P. Roche. Oscillations in exchange coupling and magnetoresistance in metallic superlattice structures: Co/Ru, Co/Cr, and Fe/Cr. *Physical Review Letters*, 64(19):2304, 5 1990.

[29] J S Moodera, Lisa R Kinder, Terrilyn M Wong, and R Meservey. Large Magnetoresistance at Room Temperature in Ferromagnetic Thin Film Tunnel Junctions. 74:16, 1995.

[30] Shun-Qing Shen. Spintronics and Spin Current. In *AAPPS Bulletin October*, volume 18, 2008.

[31] A. Manchon, H. C. Koo, J. Nitta, S. M. Frolov, and R. A. Duine. New perspectives for Rashba spin–orbit coupling. *Nature Materials 2015 14:9*, 14(9):871–882, 8 2015.

[32] N. A. Sinitsyn, E. M. Hankiewicz, Winfried Teizer, and Jairo Sinova. Spin Hall and spin-diagonal conductivity in the presence of Rashba and Dresselhaus spin-orbit coupling. *Physical Review B - Condensed Matter and Materials Physics*, 70(8):081312, 8 2004.

[33] M. I. Dyakonov and V. I. Perel. Current-induced spin orientation of electrons in semiconductors. *Physics Letters A*, 35(6):459–460, 7 1971.

[34] Naoto Nagaosa, Jairo Sinova, Shigeki Onoda, A. H. MacDonald, and N. P. Ong. Anomalous Hall effect. *Reviews of Modern Physics*, 82(2):1539, 5 2010.

[35] J. Wunderlich, B. Kaestner, J. Sinova, and T. Jungwirth. Experimental Observation of the Spin-Hall Effect in a Two-Dimensional Spin-Orbit Coupled Semiconductor System. *Physical Review Letters*, 94(4):047204, 2 2005.

[36] Y. K. Kato, R. C. Myers, A. C. Gossard, and D. D. Awschalom. Observation of the Spin Hall Effect in Semiconductors. *Science*, 306(5703):1910–1913, 12 2004.

[37] Ganesh Sundaram and Qian Niu. Wave-packet dynamics in slowly perturbed crystals: Gradient corrections and Berry-phase effects. *Physical Review B*, 59(23):14915, 6 1999.

[38] Dimitrie Culcer, Yugui Yao, and Qian Niu. Coherent wave-packet evolution in coupled bands. *Physical Review B - Condensed Matter and Materials Physics*, 72(8):085110, 8 2005.

[39] M V Berry. Quantal Phase Factors Accompanying Adiabatic Changes. *Proceedings of the Royal Society of London. Series A, Mathematical and Physical Sciences*, 392:45–57, 1984.

[40] Yu A. Bychkov and E. I. Rashba. Oscillatory effects and the magnetic susceptibility of carriers in inversion layers. *Journal of Physics C: Solid State Physics*, 17(33):6039, 11 1984.

[41] J. Smit. The spontaneous hall effect in ferromagnetics I. *Physica*, 21(6-10):877–887, 1 1955.

[42] L. Berger. Influence of spin-orbit interaction on the transport processes in ferromagnetic nickel alloys, in the presence of a degeneracy of the 3d band. *Physica*, 30(6):1141–1159, 6 1964.

[43] P. Němec, M. Fiebig, T. Kampfrath, and A. V. Kimel. Antiferromagnetic opto-spintronics. *Nature Physics 2018 14:3*, 14(3):229–241, 3 2018.

[44] T. Jungwirth, X. Marti, P. Wadley, and J. Wunderlich. Antiferromagnetic spintronics. *Nature Nanotechnology 2016 11:3*, 11(3):231–241, 3 2016.

[45] Yang Zhang, Yan Sun, Hao Yang, Jakub Železný, Stuart P.P. Parkin, Claudia Felser, and Binghai Yan. Strong anisotropic anomalous Hall effect and spin Hall effect in the chiral antiferromagnetic compounds Mn3X (X=Ge, Sn, Ga, Ir, Rh, and Pt). *Physical Review B*, 95(7):075128, 2 2017.

[46] Pei Xin Qin, Han Yan, Xiao Ning Wang, Ze Xin Feng, Hui Xin Guo, Xiao Rong Zhou, Hao Jiang Wu, Xin Zhang, Zhao Guo Gang Leng, Hong Yu Chen, and Zhi Qi Liu. Noncollinear spintronics and electric-field control: a review. *Rare Metals*, 39(2):95–112, 2 2020.

[47] A. Kohn, A. Kovács, R. Fan, G. J. McIntyre, R. C.C. Ward, and J. P. Goff. The antiferromagnetic structures of IrMn3 and their influence on exchange-bias. *Scientific Reports 2013 3:1*, 3(1):1–7, 8 2013.

[48] James M. Taylor, Edouard Lesne, Anastasios Markou, Fasil Kidane Dejene, Benedikt Ernst, Adel Kalache, Kumari Gaurav Rana, Neeraj Kumar, Peter Werner, Claudia Felser, and Stuart S.P. Parkin. Epitaxial growth, structural characterization, and exchange bias of noncollinear antiferromagnetic M n3Ir thin films. *Physical Review Materials*, 3(7):074409, 7 2019.

[49] James Mark Taylor. *Epitaxial thin films of the noncollinear antiferromagnets Mn3Ir and Mn3Sn for topological spintronic applications*. PhD thesis, Martin-Luther-Universitt Halle-Wittenberg, 2020.

[50] Christoph Sürgers, Wolfram Kittler, Thomas Wolf, and Hilbert V. Löhneysen. Anomalous Hall effect in the noncollinear antiferromagnet Mn5Si3. *AIP Advances*, 6(5):055604, 3 2016.

[51] Naoto Nagaosa, Jairo Sinova, Shigeki Onoda, A. H. MacDonald, and N. P. Ong. Anomalous Hall effect. *Reviews of Modern Physics*, 82(2):1539–1592, 5 2010.

[52] Zijian Xiong, Trinanjan Datta, and Dao-Xin Yao. ARTICLE Resonant inelastic x-ray scattering study of vector chiral ordered kagome antiferromagnet.

[53] David Vanderbilt. Berry Phases and Curvatures in Electronic-Structure Theory. 2006.

[54] K. Kuroda, T. Tomita, M. T. Suzuki, C. Bareille, A. A. Nugroho, P. Goswami, M. Ochi, M. Ikhlas, M. Nakayama, S. Akebi, R. Noguchi, R. Ishii, N. Inami, K. Ono, H. Kumigashira, A. Varykhalov, T. Muro, T. Koretsune, R. Arita, S. Shin, Takeshi Kondo, and S. Nakatsuji. Evidence for magnetic Weyl fermions in a correlated metal. *Nature Materials 2017 16:11*, 16(11):1090–1095, 9 2017.

[55] C. Helman, A. Camjayi, E. Islam, M. Akabori, L. Thevenard, C. Gourdon, and M. Tortarolo. Anomalous Hall effect in MnAs: Intrinsic contribution due to Berry curvature. *Physical Review B*, 103(13):134408, 4 2021.

[56] Weifeng Zhang, Wei Han, See Hun Yang, Yan Sun, Yang Zhang, Binghai Yan, and Stuart S.P. Parkin. Giant facet-dependent spin-orbit torque and spin Hall conductivity in the triangular antiferromagnet IrMn3. *Science Advances*, 2(9), 9 2016.

[57] Z. Q. Liu, H. Chen, J. M. Wang, J. H. Liu, K. Wang, Z. X. Feng, H. Yan, X. R. Wang, C. B. Jiang, J. M.D. Coey, and A. H. Macdonald. Electrical switching of the topological anomalous Hall effect in a non-collinear antiferromagnet above room temperature. *Nature Electronics 2018 1:3*, 1(3):172–177, 3 2018.

[58] Hua Chen, Qian Niu, and A. H. Macdonald. Anomalous hall effect arising from noncollinear antiferromagnetism. *Physical Review Letters*, 112(1):017205, 1 2014.

[59] Tomoya Higo, Huiyuan Man, Daniel B. Gopman, Liang Wu, Takashi Koretsune, Olaf M.J. Van 'T Erve, Yury P. Kabanov, Dylan Rees, Yufan Li, Michi To Suzuki, Shreyas Patankar, Muhammad Ikhlas, C. L. Chien, Ryotaro Arita, Robert D. Shull, Joseph Orenstein, and Satoru Nakatsuji. Large magneto-optical Kerr effect and imaging of magnetic octupole domains in an antiferromagnetic metal. *Nature Photonics 2018 12:2*, 12(2):73–78, 1 2018.

[60] Satoru Nakatsuji, Naoki Kiyohara, and Tomoya Higo. Large anomalous Hall effect in a non-collinear antiferromagnet at room temperature. *Nature 2015 527:7577*, 527(7577):212–215, 10 2015.

[61] Jing Zhou, Xinyu Shu, Yaohua Liu, Xiao Wang, Weinan Lin, Shaohai Chen, Liang Liu, Qidong Xie, Tao Hong, Ping Yang, Binghai Yan, Xiufeng Han, and Jingsheng Chen. Magnetic asymmetry induced anomalous spin-orbit torque in IrMn. *Physical Review B*, 101(18):184403, 5 2020.

[62] Longjie Yu, Shutaro Karube, Min Liu, Masakiyo Tsunoda, Mikihiko Oogane, and Yasuo Ando. Observation of unconventional spin polarization induced spin orbit torque in L1 2-ordered antiferromagnetic Mn3Pt thin films. *Applied Physics Express*, 15(033002), 2022.

[63] H. Bai, X. F. Zhou, H. W. Zhang, W. W. Kong, L. Y. Liao, X. Y. Feng, X. Z. Chen, Y. F. You, Y. J. Zhou, L. Han, W. X. Zhu, F. Pan, X. L. Fan, and C. Song. Control of spin-orbit torques through magnetic symmetry in differently oriented noncollinear antiferromagnetic Mn3Pt. *Physical Review B*, 104(10):104401, 9 2021.

[64] E. Krén, G. Kádár, L. Pál, and P. Szabó. Investigation of the First-Order Magnetic Transformation in Mn3Pt. *Journal of Applied Physics*, 38(3):1265, 6 2004.

[65] B. D. Josephson. Possible new effects in superconductive tunnelling. *Physics Letters*, 1(7):251–253, 7 1962.

[66] E. Wimmer and A. J. Freeman. Fundamentals of the Electronic Structure of Surfaces. *Handbook of Surface Science*, 2:1–91, 1 2000.

[67] Tomoya Higo, Huiyuan Man, Daniel B. Gopman, Liang Wu, Takashi Koretsune, Olaf M.J. Van 'T Erve, Yury P. Kabanov, Dylan Rees, Yufan Li, Michi To Suzuki, Shreyas Patankar, Muhammad Ikhlas, C. L. Chien, Ryotaro Arita, Robert D. Shull, Joseph Orenstein, and Satoru Nakatsuji. Large magneto-optical Kerr effect and imaging of magnetic octupole domains in an antiferromagnetic metal. *Nature Photonics 2018 12:2*, 12(2):73–78, 1 2018.

[68] Z. Q. Qiu and S. D. Bader. Surface magneto-optic Kerr effect. *Review of Scientific Instruments*, 71(3):1243, 3 2000.

[69] Rudi Rottenfusser. https://zeiss-campus.magnet.fsu.edu/articles/basics/resolution.html.

[70] Seungha Yoon, Jason Liu, and Robert D. McMichael. Phase-resolved ferromagnetic resonance using a heterodyne detection method. *Physical Review B*, 93(14):144423, 4 2016.

[71] Jack C Sankey, Yong-Tao Cui, Jonathan Z Sun, John C Slonczewski, Robert A Buhrman, and Daniel C Ralph. Measurement of the spin-transfer-torque vector in magnetic tunnel junctions. *Nature Physics*, 4(1):67–71, 2008.

[72] Hitoshi Kubota, Akio Fukushima, Kay Yakushiji, Taro Nagahama, Shinji Yuasa, Koji Ando, Hiroki Maehara, Yoshinori Nagamine, Koji Tsunekawa, David D. Djayaprawira, Naoki Watanabe, and Yoshishige Suzuki. Quantitative measurement of voltage dependence of spin-transfer torque in MgO-based magnetic tunnel junctions. *Nature Physics*, 4(1):37–41, 2008.

[73] Yi Wang, Rajagopalan Ramaswamy, and Hyunsoo Yang. FMR-related phenomena in spintronic devices. *Journal of Physics D: Applied Physics*, 51(27):273002, 6 2018.

[74] Yi Wang, Dapeng Zhu, Yang Wu, Yumeng Yang, Jiawei Yu, Rajagopalan Ramaswamy, Rahul Mishra, Shuyuan Shi, Mehrdad Elyasi, Kie Leong Teo, Yihong Wu, and Hyunsoo Yang. Room temperature magnetization switching in topological insulator-ferromagnet heterostructures by spin-orbit torques. *Nature Communications 2017 8:1*, 8(1):1–6, 11 2017.

[75] A. R. Mellnik, J. S. Lee, A. Richardella, J. L. Grab, P. J. Mintun, M. H. Fischer, A. Vaezi, A. Manchon, E. A. Kim, N. Samarth, and D. C. Ralph. Spin-transfer torque generated by a topological insulator. *Nature 2014 511:7510*, 511(7510):449–451, 7 2014.

[76] Yi Wang, Praveen Deorani, Karan Banerjee, Nikesh Koirala, Matthew Brahlek, Seongshik Oh, and Hyunsoo Yang. Topological surface states originated spin-orbit torques in Bi2Se3. *Physical Review Letters*, 114(25):257202, 6 2015.

[77] Changsoo Kim, Dongseuk Kim, Byong Sun Chun, Kyoung Woong Moon, and Chanyong Hwang. Evaluation Method for Fieldlike-Torque Efficiency by Modulation of the Resonance Field. *Physical Review Applied*, 9(5):054035, 5 2018.

[78] K. Ando, S. Takahashi, K. Harii, K. Sasage, J. Ieda, S. Maekawa, and E. Saitoh. Electric manipulation of spin relaxation using the spin hall effect. *Physical Review Letters*, 101(3):036601, 7 2008.

[79] Junyeon Kim, Jaivardhan Sinha, Masamitsu Hayashi, Michihiko Yamanouchi, Shunsuke Fukami, Tetsuhiro Suzuki, Seiji Mitani, and Hideo Ohno. Layer thickness dependence of the current-induced effective field vector in Ta|CoFeB|MgO. *Nature materials*, 12(3):240–245, 3 2013.

[80] Hanshen Tsai, Tomoya Higo, Kouta Kondou, Takuya Nomoto, Akito Sakai, Ayuko Kobayashi, Takafumi Nakano, Kay Yakushiji, Ryotaro Arita, Shinji Miwa, Yoshichika Otani, and Satoru Nakatsuji. Electrical manipulation of a topological antiferromagnetic state. *Nature*, 580(7805):608–613, 4 2020.

[81] H. Dery, P. Dalal, Cywiński, and L. J. Sham. Spin-based logic in semiconductors for reconfigurable large-scale circuits. *Nature*, 447(7144):573–576, 5 2007.

[82] Lijun Zhu, Daniel C. Ralph, and Robert A. Buhrman. Maximizing spin-orbit torque generated by the spin Hall effect of Pt. *Applied Physics Reviews*, 8(3):031308, 8 2021.

[83] Lijun Zhu, Lujun Zhu, Manling Sui, Daniel C. Ralph, and Robert A. Buhrman. Variation of the giant intrinsic spin Hall conductivity of Pt with carrier lifetime. *Science Advances*, 5(7), 7 2019.

[84] G. Y. Guo, S. Murakami, T. W. Chen, and N. Nagaosa. Intrinsic spin hall effect in platinum: First-principles calculations. *Physical Review Letters*, 100(9):096401, 3 2008.

[85] Ryan Freeman, Andrei Zholud, Zhiling Dun, Haidong Zhou, and Sergei Urazhdin. Evidence for dyakonov-perel-like spin relaxation in Pt. *Physical Review Letters*, 120(6):067204, 2 2018.

[86] Yi Wang, Praveen Deorani, Xuepeng Qiu, Jae Hyun Kwon, and Hyunsoo Yang. Determination of intrinsic spin Hall angle in Pt. *Applied Physics Letters*, 105(15):152412, 10 2014.

[87] Chirag Garg, See Hun Yang, Leslie Thompson, Teya Topuria, Amir Capua, Brian Hughes, Timothy Phung, Panagiotis Ch Filippou, and Stuart S.P. Parkin. Efficient chiral-domain-wall motion driven by spin-orbit torque in metastable platinum films. *Physical Review Applied*, 14(3):034052, 9 2020.

[88] Yin Zhang, Q. Liu, B. F. Miao, H. F. Ding, and X. R. Wang. Anatomy of electrical signals and dc-voltage line shape in spin-torque ferromagnetic resonance. *Physical Review B*, 2019.

[89] Ranen Ben-Shalom, Nirel Bernstein, Stuart S.P. Parkin, See Hun Yang, and Amir Capua. Determination of the spin Hall angle by the inverse spin Hall effect, device level

ferromagnetic resonance, and spin torque ferromagnetic resonance: A comparison of methods. *Applied Physics Letters*, 119(4):042401, 7 2021.

[90] E. Saitoh, M. Ueda, H. Miyajima, and G. Tatara. Conversion of spin current into charge current at room temperature: Inverse spin-Hall effect. *Applied Physics Letters*, 88(18):182509, 5 2006.

[91] Kyeong Dong Lee, Dong Jun Kim, Hae Yeon Lee, Seung Hyun Kim, Jong Hyun Lee, Kyung Min Lee, Jong Ryul Jeong, Ki Suk Lee, Hyon Seok Song, Jeong Woo Sohn, Sung Chul Shin, and Byong Guk Park. Thermoelectric Signal Enhancement by Reconciling the Spin Seebeck and Anomalous Nernst Effects in Ferromagnet/Non-magnet Multilayers. *Scientific Reports 2015 5:1*, 5(1):1–10, 5 2015.

[92] Weifeng Zhang, Wei Han, Xin Jiang, See Hun Yang, and Stuart S.P. Parkin. Role of transparency of platinum-ferromagnet interfaces in determining the intrinsic magnitude of the spin Hall effect. *Nature Physics*, 2015.

[93] S. Petit, C. Baraduc, C. Thirion, U. Ebels, Y. Liu, M. Li, P. Wang, and B. Dieny. Spin-torque influence on the high-frequency magnetization fluctuations in magnetic tunnel junctions. *Physical Review Letters*, 98(7):077203, 2 2007.

[94] Hujun Jiao and Gerrit E.W. Bauer. Spin Backflow and ac Voltage Generation by Spin Pumping and the Inverse Spin Hall Effect. *Physical Review Letters*, 110(21):217602, 5 2013.

[95] O. Mosendz, J. E. Pearson, F. Y. Fradin, G. E.W. Bauer, S. D. Bader, and A. Hoffmann. Quantifying spin hall angles from spin pumping: Experiments and theory. *Physical Review Letters*, 104(4):046601, 1 2010.

[96] K. Ando, S. Takahashi, J. Ieda, Y. Kajiwara, H. Nakayama, T. Yoshino, K. Harii, Y. Fujikawa, M. Matsuo, S. Maekawa, and E. Saitoh. Inverse spin-Hall effect induced by spin pumping in metallic system. *Journal of Applied Physics*, 109(10):103913, 5 2011.

[97] Ioan Mihai Miron, Gilles Gaudin, Stéphane Auffret, Bernard Rodmacq, Alain Schuhl, Stefania Pizzini, Jan Vogel, and Pietro Gambardella. Current-driven spin torque induced by the Rashba effect in a ferromagnetic metal layer. *Nature materials*, 9(3):230–234, 2010.

[98] Ioan Mihai Miron, Kevin Garello, Gilles Gaudin, Pierre Jean Zermatten, Marius V. Costache, Stéphane Auffret, Sébastien Bandiera, Bernard Rodmacq, Alain Schuhl, and Pietro Gambardella. Perpendicular switching of a single ferromagnetic layer induced by in-plane current injection. *Nature 2011 476:7359*, 476(7359):189–193, 8 2011.

[99] Luqiao Liu, Chi Feng Pai, Y. Li, H. W. Tseng, D. C. Ralph, and R. A. Buhrman. Spin-torque switching with the giant spin hall effect of tantalum. *Science*, 336(6081):555–558, 5 2012.

[100] J. E. Hirsch. Spin Hall Effect. *Physical Review Letters*, 83(9):1834, 8 1999.

[101] T. Nan, C. X. Quintela, J. Irwin, G. Gurung, D. F. Shao, J. Gibbons, N. Campbell, K. Song, S. Y. Choi, L. Guo, R. D. Johnson, P. Manuel, R. V. Chopdekar, I. Hallsteinsen, T. Tybell, P. J. Ryan, J. W. Kim, Y. Choi, P. G. Radaelli, D. C. Ralph, E. Y. Tsymbal, M. S. Rzchowski, and C. B. Eom. Controlling spin current polarization through non-collinear antiferromagnetism. *Nature Communications 2020 11:1*, 11(1):1–7, 9 2020.

[102] D. MacNeill, G. M. Stiehl, M. H.D. Guimaraes, R. A. Buhrman, J. Park, and D. C. Ralph. Control of spin–orbit torques through crystal symmetry in WTe2/ferromagnet bilayers. *Nature Physics 2016 13:3*, 13(3):300–305, 11 2016.

[103] Marcos H.D. Guimarães, Gregory M. Stiehl, David MacNeill, Neal D. Reynolds, and Daniel C. Ralph. Spin-Orbit Torques in NbSe2/Permalloy Bilayers. *Nano Letters*, 18(2):1311–1316, 2018.

[104] Xianzhe Chen, Shuyuan Shi, Guoyi Shi, Xiaolong Fan, Cheng Song, Xiaofeng Zhou, Hua Bai, Liyang Liao, Yongjian Zhou, Hanwen Zhang, Ang Li, Yanhui Chen, Xiaodong Han, Shan Jiang, Zengwei Zhu, Huaqiang Wu, Xiangrong Wang, Desheng Xue, Hyunsoo Yang, and Feng Pan. Observation of the antiferromagnetic spin Hall effect. *Nature Materials*.

[105] Yunfeng You, Hua Bai, Xiaoyu Feng, Xiaolong Fan, Lei Han, Xiaofeng Zhou, Yongjian Zhou, Ruiqi Zhang, Tongjin Chen, Feng Pan, and Cheng Song. Cluster magnetic octupole induced out-of-plane spin polarization in antiperovskite antiferromagnet. *Nature Communications 2021 12:1*, 12(1):1–8, 11 2021.

[106] Liang Liu, Chenghang Zhou, Xinyu Shu, Changjian Li, Tieyang Zhao, Weinan Lin, Jinyu Deng, Qidong Xie, Shaohai Chen, Jing Zhou, Rui Guo, Han Wang, Jihang Yu, Shu Shi, Ping Yang, Stephen Pennycook, Aurelien Manchon, and Jingsheng Chen. Symmetry-dependent field-free switching of perpendicular magnetization. *Nature Nanotechnology 2021 16:3*, 16(3):277–282, 1 2021.

[107] Motoi Kimata, Hua Chen, Kouta Kondou, Satoshi Sugimoto, Prasanta K. Muduli, Muhammad Ikhlas, Yasutomo Omori, Takahiro Tomita, Allan H. MacDonald, Satoru Nakatsuji, and Yoshichika Otani. Magnetic and magnetic inverse spin Hall effects in a non-collinear antiferromagnet. *Nature 2019 565:7741*, 565(7741):627–630, 1 2019.

[108] M. C. Weber, H. Nembach, B. Hillebrands, and J. Fassbender. Modified Gilbert damping due to exchange bias in NiFeFeMn bilayers. *Journal of Applied Physics*, 97(10):10A701, 4 2005.

[109] Shujuan Yuan, Baojuan Kang, Liming Yu, Shixun Cao, and Xinluo Zhao. Increased ferromagnetic resonance linewidth and exchange anisotropy in NiFe/FeMn bilayers. *Journal of Applied Physics*, 105(6):063902, 3 2009.

List of Publications and Presentations

Refereed Journals/Manuscripts Under Preparation

1. **Bharat Grover**, Binoy Krishna Hazra, Tianping Ma, Banabir Pal, Nirel Bernstein, Amit Rothschild, Abhay Kant Srivastava, Samiran Choudhury, Georg Woltersdorf, Amir Capua, and Stuart S. P. Parkin. “Crystallographic dependence of the spin Hall angle in epitaxial Pt films: Comparison of optical and electrical detection of spin-torque ferromagnetic resonance techniques”, *Applied Physics Letters*, 120, 172406 (2022) (**Featured Article**).

2. Binoy Krishna Hazra, **Bharat Grover**, Banabir Pal, Jae-Chun Jeon, Holger Meyerheim, Stuart S. P. Parkin. “Dependence of spin-orbit-torque on exchange bias in non-collinear antiferromagnet/ferromagnet heterostructures” (Manuscript in Preparation).

3. Mohsin Z Minhas, Avanindra K Pandeya, **Bharat Grover**, Alessandro Fumarola, Ilya Kostanovskiy, Binoy K Hazra, Wolfgang Hoppe, Georg Woltersdorf, Amilcar Bedoya-Pinto, Stuart S P Parkin. “Doping-induced spin Hall ratio enhancement in A15-phase, Ta-doped β-W thin films", *J. Phys. Mater.*, 3, 044001, 2020.

4. Binoy Krishna Hazra, Banabir Pal, Jae-Chun Jeon, Robin R. Neumann, Börge Göbel, **Bharat Grover**, Hakan Deniz, Andriy Styervoyedov, Holger Meyerheim, Ingrid Mertig, See-Hun Yang, Stuart S. P. Parkin. “Interface generated out of plane polarized spin current” (Manuscript accepted in Nature Communication)

Conference Abstracts/Posters/Presentations

1. Bharat Grover, “Spin Hall effect in non-collinear antiferromagnets”,*Joint European Magnetic Symposia, Upsala, Sweden*, August 2019.

2. Bharat Grover, “Measurement of the spin currents: Comparison of optical and electrical methods”, *APS March Meeting*, March 2021.

Contribution of the Author

The author made the following key technical and scientific contributions during his doctoral research :

1. **Development of an Optical Setup**: Designed and constructed a custom optical setup from scratch to perform Optically Detected Ferromagnetic Resonance (OFMR) measurements. This included aligning laser sources, integrating free-space polarization optics, and ensuring synchronization between the laser and RF signals. The setup was made to precisely measure spin-orbit coupling effects, providing a powerful alternative to conventional electrical measurement techniques.
2. **Creation of LabVIEW Virtual Instruments (VIs)**: To automate the entire optical experiment setup, the author developed LabVIEW VIs to control the experimental process and used them to automatically analyze the data after each measurement sequence.
3. **SOT and SHE Characterization**: Characterized the crystallographic dependence of Spin-Orbit Torque (SOT) and Spin Hall Effect (SHE) in heavy metal and antiferromagnetic thin films across different crystallographic orientations.
4. **Sample Fabrication and Optimization**: Fabricating devices of high-quality epitaxial Pt and Mn_3Pt thin films in clean room to study the SHE and SOTs in different crystallographic directions.
5. **Data Analysis and Interpretation**: Conducted rigorous data analysis to investigate the angular and current-dependent characteristics of SOTs using both OFMR and STFMR measurement setup.

Eidesstattliche Erklärung

Ich, Bharat Grover, erkläre hiermit an Eides statt, dass ich die Arbeit selbstständig und ohne fremde Hilfe verfasst habe. Ich habe keine anderen als die von mir angegebenen Quellen und Hilfsmittel benutzt und die den benutzten Werken wörtlich oder inhaltlich entnommenen Stellen als solche kenntlich gemacht.

Name: Bharat Grover
Ort: Halle (Saale)
Datum: 25.10.2024